GEOCHEMISTRY AND GEOCHRONOLOGY OF THE PERMIAN ARC MAGMATISM OF THE CENTRAL CORDILLERA OF COLOMBIA

Geoquímica y geocronología del magmatismo de arco pérmico de la Cordillera Central de Colombia

MARCELA RESTREPO VELÁSQUEZ

Tesis

Asesor

Camilo Bustamante Londoño

UNIVERSIDAD EAFIT

ESCUELA DE CIENCIAS APLICADAS E INGENIERÍA

MAESTRÍA EN CIENCIAS DE LA TIERRA

MEDELLÍN

2022

Abstract

In Colombia, the occurrence of Permian magmatic rocks is restricted to a few localities at the Sierra Nevada de Santa Marta, the Serranía de San Lucas, and the Central Cordillera. Previous works have focused mainly on explaining its tectonic setting whereas petrogenesis has received less attention. This study reports whole-rock geochemistry, zircon U-Pb geochronology, trace elements, and Hf isotopes from mylonitic and massive granitoids located along the Tolima region (eastern flank of the Central Cordillera) to constraint their age, source, and petrogenesis. Our results show that the granitoids have a calc-alkaline character, are rich in light-rare elements (LREEs), and large-ion lithophile elements (LILEs), present negative Nb and Ti anomalies; crystallized between 273-265 Ma; and show variable εHf(i) values ranging from -1.5 to +1.7. Combining our results with published geochemical, geochronological, and isotopic data from this region, we suggest that the Middle Permian granitoids from the Tolima region were formed in a continental magmatic arc installed at the western margin of Gondwana, where crustal assimilation and partial melting of an old radiogenic and heterogeneous crust were essential processes for the modification of the source of the magmas that generated the granitoids. The peak magmatic conditions may have been reached by the middle Permian (~280-270 Ma), according to the recurrence of ages in this time interval. This period of magmatic activity may have been interrupted by the Triassic extensional period related to the beginning of the Pangea breakup.

Resumen

En Colombia, la ocurrencia de rocas magmáticas pérmicas está limitada a pocas regiones como la Sierra Nevada de Santa Marta, la Serranía de San Lucas y la Cordillera Central. Trabajos anteriores se han enfocado principalmente en explicar el ambiente de formación de estas rocas, mientras que los procesos que las generaron han recibido menos atención. En esta investigación, aplicamos geoquímica de roca total, geocronología U-Pb y elementos traza de circón e isótopos de Hf en granitoides miloníticos y masivos ubicados a lo largo del departamento de Tolima (flanco oriental de la Cordillera Central) para definir su edad, ambiente, fuente y los procesos involucrados para su formación. Nuestros resultados indican que los granitoides presentan una firma calco-alcalina, son ricos en elementos raros ligeros (LREEs) y elementos litófilos de ión grande (LILEs), presentan anomalías negativas de Nb y Ti; cristalizaron durante el Pérmico Medio (273-265 Ma); y muestran valores variables de εHf(i) que oscilan entre -1,5 y +1,7. La combinación de nuestros resultados con datos geoquímicos, geocronológicos e isotópicos publicados indican que los granitoides del Pérmico Medio ubicados en el departamento de Tolima se formaron en un arco magmático continental generado a lo largo del margen occidental de Gondwana y que procesos como asimilación y fusión parcial de una antigua corteza heterogénea fueron esenciales para la modificación de la fuente de los magmas. El pico del magmatismo pudo haber sido alcanzado durante el Pérmico Medio (~280-270 Ma), según la recurrencia de edades en este intervalo de tiempo. Se considera que este período de actividad magmática se vio reducido durante el Triásico, debido a un período de extensión relacionado con el comienzo de la separación del supercontinente Pangea.

1. Introduction

As a result of the closure of the Rheic Ocean between ca. 358-280 Ma, Laurussia, and Gondwana were sutured and formed the supercontinent Pangea. This suture produced the Ouachita-Alleghanian-Variscan collisional orogen, which extended over 10,000 km from Middle America to Eastern Europe (Nance and Linnemann, 2008). Meanwhile, the Terra Australis accretionary orogen was active along the Pacific margin of Gondwana (Cawood, 2005), which was the manifestation of a subduction zone that extended throughout the continental margins of Australia, Antarctica, New Zealand, South Africa, and South America (Cawood and Buchan, 2007).

The formation of the Gondwanide Orogen marked the end of the Terra Australis Orogen during the Permian and the Triassic (ca. 300-230 Ma) along the Pan-Pacific Gondwana margin. The latter involved stepping out in the plate boundary position in areas like eastern Australia and Antarctica. In contrast, in South America, the plate boundary remained relatively fixed with younger units superimposed directly on pre-existing tectonic elements (Cawood, 2005), and changes like a drastic reduction in plate velocities and an almost complete pause in continental drift (Vilas and Valencio, 1978; Riel et al., 2018), producing heat accumulation and large volumes of magmas (e.g., Kay et al., 1989), as well as geographically extensive extension along with western South America (e.g., Charrier et al., 2007; Spikings et al., 2015, 2016).

The Late Paleozoic geological record of the Northern Andes includes rocks correlated to the final stages of Pangea assembly (Viscarret et al., 2009; van der Lelij et al., 2016, 2019; Paul et al., 2018; Cochrane et al., 2014; Spikings and Paul, 2019; Rodríguez-García et al., 2019). In Colombia, Permian rocks have been reported in the Sierra Nevada de Santa Marta,

the Serranía de San Lucas, and the Central Cordillera, including granitoids, mylonites, migmatites, and gneisses. The magmatic activity was mostly acid in composition and lasted for about 40 Ma (293-253 Ma) (Spikings and Paul, 2019; Rodríguez-García et al., 2019 and references therein).

Two interpretations have been proposed to explain the formation of these rocks: i) a collisional event related to the agglutination of the Pangea supercontinent and the Ouachita-Alleghanian-Variscan Orogen, which produced collisional plutonism that caused partial melting of the continental crust, and a regional metamorphic event that affected Permian intrusive bodies (Vinasco et al., 2006; Vinasco, 2019). ii) a continental arc related to the subduction of the Panthalassa oceanic crust at the western Gondwana margin outside the nucleus of the Laurentia–Gondwana Ouachita-Alleghanian-Variscan orogens, which is part of a broader magmatic province that extends from the Southern Eastern Cordillera of Perú to allochthonous Mexican terranes (Cardona et al., 2010; Spikings and Paul, 2019; Piraquive et al., 2021). The growing geochronological and geochemical data of these recent works have served mainly to position the magmatic rocks into regional geotectonic models, but less attention has been paid to their petrogenesis and their implications in the evolution of the arc magmatism recorded in the northern Andes.

In this study, we report new whole-rock geochemistry, U-Pb, Hf isotopes, and trace elements in zircons from Permian lithologies of the Central Cordillera of Colombia, which combined with recently reported geochemical and U-Pb data, will allow us to constrain the age, source, and petrogenesis of the Permian magmatism of the western margin of Gondwana. Furthermore, our results will provide further insights into the tectonic

configuration of the final stages of the Pangea assembly and shed light on the evolution of the Permian arc-related magmatism during its peak.

2. Geological setting

The Colombian Andes consist of three major mountain ranges, the Western, Central, and Eastern Cordilleras, separated by the Cauca and Magdalena valleys. The Western Cordillera comprises Cretaceous, allochthonous ultramafic, mafic rocks, and marine sediments formed in an intra-oceanic plateau and arc-related setting (Kerr et al., 1997; Villagómez et al., 2011; Hincapié-Gómez et al., 2018). The Central Cordillera includes a Paleozoic to Early Mesozoic metamorphic basement intruded by Jurassic to Paleogene arc-related plutonic bodies, and Cretaceous volcano-sedimentary and high P/T metamorphic rocks that records events like the agglutination and dispersal of Pangea, mainly related to preserve subduction/accretion complex and back-arc opening and closure tectonics (Bustamante et al., 2010; Cochrane et al., 2014; Bustamante et al., 2016; 2017; Duque-Trujillo et al., 2019; Bustamante et al., 2011; 2012; Zapata et al., 2019; Jaramillo et al., 2017; Bustamante et al., 2021; Avellaneda-Jiménez et al., 2020). The Eastern Cordillera contains a Precambrian-Paleozoic metamorphic basement covered by Paleozoic to Cenozoic marine and siliciclastic sedimentary sequences and intruded by Cretaceous gabbroic dikes and sills (Cortés et al., 2006; Mora et al., 2009; Vásquez et al., 2010; Sarmiento-Rojas, 2019).

2.1. Permian magmatic and metamorphic record in Colombia

Permian magmatic and metamorphic rocks in Colombia are limited to a few localities like at the Sierra Nevada de Santa Marta, the Serranía de San Lucas, and the Central

Cordillera (Fig. 1). In the Sierra Nevada de Santa Marta, El Encanto Orthogneiss and the northeastern segment of the Inner Santa Marta Metamorphic Belt include a series of non-deformed granitoids, mylonitized granitoids, mylonites, protomylonites, and orthogneisses that yields crystallization ages from ca. 288 to 264 Ma (Cardona et al., 2010; Piraquive et al., 2021). In the Serranía de San Lucas, the Nechí Gneiss is composed of gneisses, migmatites, and quartz–feldspar granofels (Rodríguez et al., 2014). According to Restrepo et al. (2011), the unit has a Permian crystallization age of 277.3 ± 3 Ma and a Triassic metamorphic age of 236.4 ± 6.6 Ma.

To the north of the Central Cordillera, the Abejorral and Rio Verde granitic gneisses units comprise gneisses composed of plagioclase, K-feldspar, quartz, biotite, muscovite, cordierite, and sillimanite; they are classified as S-type granitoids and have U-Pb zircon ages spanning between ca. 290 and 275 Ma (Vinasco et al., 2006). At the central segment of the Central Cordillera, Permian rocks have been reported in the Tierradentro gneisses and amphibolites unit, and in the Cajamarca Complex (Cochrane et al., 2014; Bustamante et al., 2017; Paul et al., 2018). The Tierradentro gneisses and amphibolites unit is a discontinuous sequence of ortho- and paragneisses, amphibolites, granulites, quartzites, and marbles in the northern segment of the Tolima region (Acosta et al., 2002; Bustamante et al., 2017). Vesga and Barrero (1978) reported a K-Ar hornblende age of 1360 ± 270 Ma, suggesting a Proterozoic age for this unit; however, Bustamante et al. (2017), according to U-Pb geochronological analyses performed in two orthogneisses and one amphibolite sample, suggest that the protoliths of these samples crystallized between 271 and 234 Ma, and are in turn, intruded by the Ibagué Batholith (Acosta et al., 2002; Bustamante et al., 2017). The Cajamarca Complex includes low- to medium-grade metamorphic rocks like pelitic schists, quartzites, marbles, amphibolites (Maya and González, 1995), and S-type granites with U/Pb

zircon crystallization ages ranging from ca. 278 to 255 Ma (Cochrane et al., 2014). The age of metamorphism of this complex varies from Mid- to Late Triassic (ca. 240–230 Ma; Vinasco et al. 2006; Restrepo et al. 2011; Cochrane et al. 2014) and Jurassic (ca. 157-146 Ma; Blanco-Quintero et al., 2014).

Along the eastern flank of the Central Cordillera, the Ortega Granite is an intrusive massif that consists of quartz monzodiorites, monzonites, tonalites, granodiorites, monzogranites, and syenogranites with U/Pb zircon crystallization ages from ca. 294 to 263 Ma (Rodríguez-Garcia et al., 2019). Finally, located in the Upper Magdalena Valley, La Plata Granite is composed of non-deformed granitoids, migmatites, and granitic rocks with folded, stromatic, and nebulitic structures. It is intruded by Jurassic magmatic rocks and covered by Cenozoic pyroclastic rocks (Rodríguez et al., 2017); according to U-Pb zircon analyses reported by Rodríguez et al. (2017) and Leal-Mejía et al. (2019), this plutonic body yields crystallization ages that range from ca. 280 to 268 Ma.

According to regional geological maps, samples collected in the studied zone (Tolima region, Central Cordillera) are part of the units Tierradentro gneisses and amphibolites and the Ibagué Batholith (Fig 2). However, based on our petrographic and geochronological analyses, we consider that the samples located in the south of the Tolima region, near the municipality of Planadas, could be an extension of the La Plata Granite (see results section).

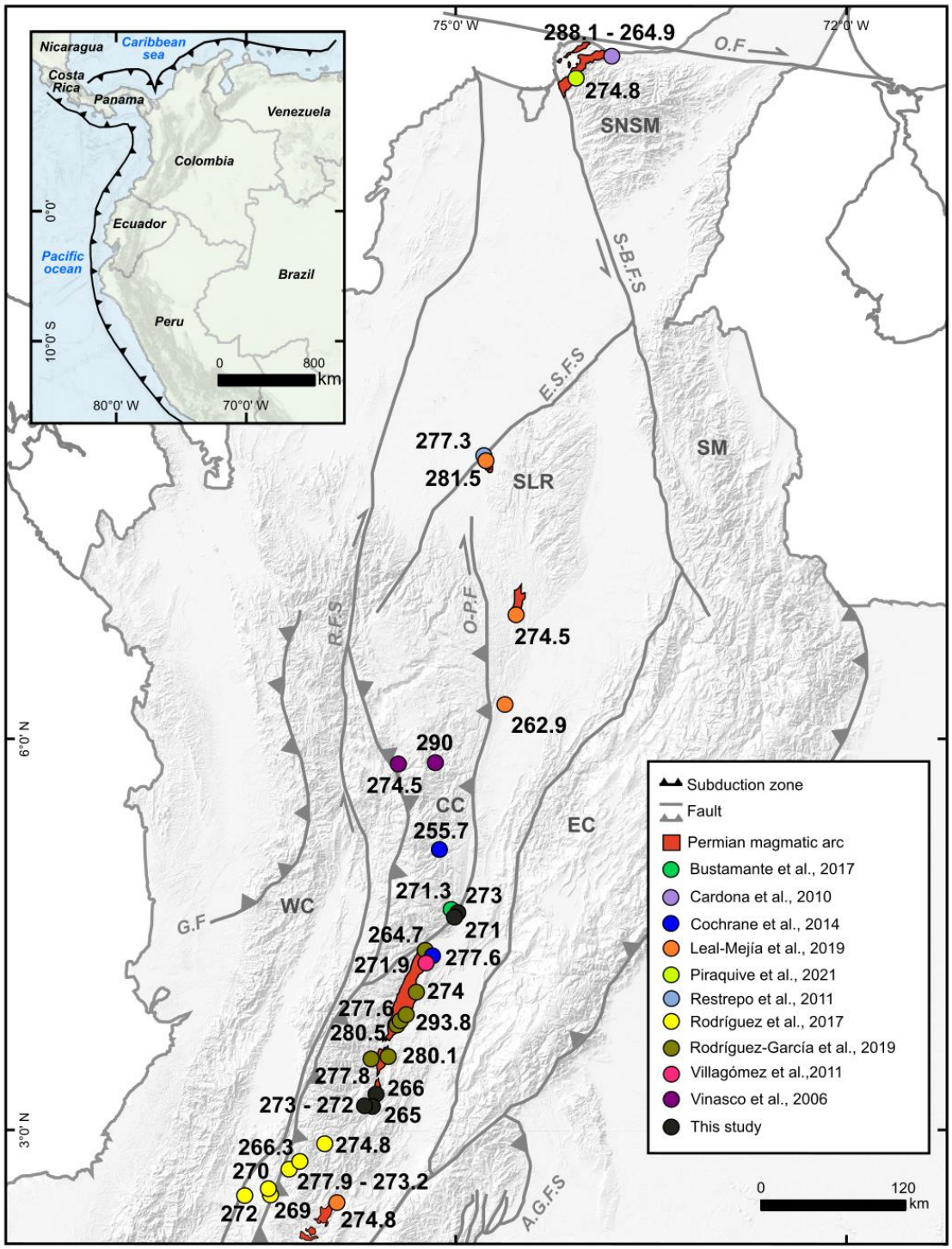

Figure 1. Permian magmatic and metamorphic rocks of Colombia. Zircon U-Pb ages from previous works and this study are included to show spatial and temporal distribution of Permian rocks. SNSM: Sierra Nevada de Santa Marta; SLR: San Lucas Range; SM: Santander Massif; WC: Western Cordillera; CC: Central Cordillera; EC: Eastern Cordillera. O.F: Oca Fault; S.B.F.S: Santa Marta-Bucaramaga Fault system. G.F: Garrapata Fault; R.F.S: Romeral Fault System; O.P.F: Otú-Pericos Fault; E.S.F.S.: Espíritu Santo Fault System; A.G.F.S: Algeciras Fault System.

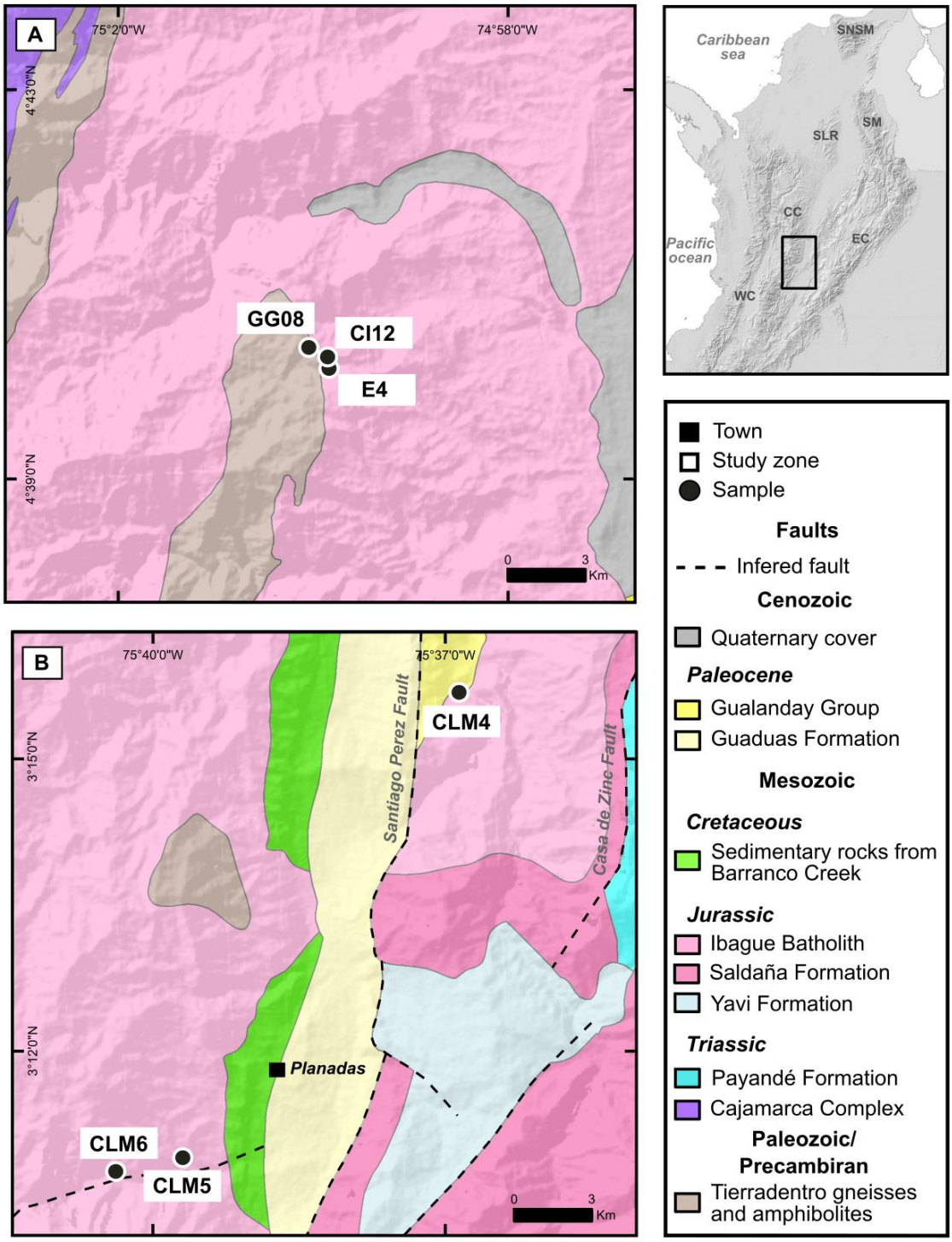

Figure 2. Geological map of the studied area showing sample location. A: North of the Tolima region, near to the municipality of Anzoátegui. B: South of the Tolima region, near to the municipality of Planadas.

3. Methods

3.1. Fieldwork and sampling

Fieldwork was carried out along the Tolima region, near the municipalities of Anzoátegui, Rovira, and Planadas (Fig. 2). A total of twelve samples were collected, where eight samples were massive granitoids, three were mylonitic granitoids, and one sample corresponded to volcanic rock. One of the mylonitic granitoids was previously dated by Bustamante et al. (2017) (sample CI12). Petrographic analysis was carried out mainly in thin sections observed under a polarized light microscope to describe textural and mineral features and select samples for geochemical, geochronological, and isotopic analyses.

3.2. Zircon U-Pb geochronology and trace elements

Zircon separation followed standard procedures (e.g., Mange and Maurer, 1992) and was performed at EAFIT University facilities. Seven samples (CLM4A, CLM5, CLM6A, CLM6B, R1, E4, and GG-8) were crushed with a conventional jawbreaker, and the heavy mineral fraction was separated from the 400-63 microns fraction using a pan. Hand-picking of zircon grains from the heavy mineral concentrates was randomly performed in each sample. After mounting the epoxy pill, zircon grains were polished and carbon-coated at ETH Zurich facilities. Zircon cathodoluminescence (CL) imagery was carried out to evaluate the magmatic zonation, metamorphic origin, rims, and inherited cores. For this purpose, we used a JEOL JSM-6390LA scanning electron microscope (SEM) at the Institute for Geochemistry and Petrology at ETH Zurich. Zircon U–Pb geochronology was performed through laser ablation inductively coupled mass spectrometry (LA-ICP-MS) at ETH Zurich, and laser ablation spots (19 microns) were selected in both cores and rims when it was possible.

In situ U-Pb geochronology was conducted by laser ablation inductively coupled plasma mass spectrometry (LA-ICP-MS) at the Institute of Geochemistry and Petrology, ETH Zurich, using a 193 nm Resolution (S155) ArF excimer laser coupled to an Element SF ICPMS (Guillong et al., 2014; von Quadt et al., 2016).

Statistical analyses of zircon data were performed using IsoplotR (Vermeesch, 2018). Only zircons with concordance higher than 90% were accepted and plotted. Errors reported for all ages are 2 sigma.

3.3. Hf Isotopes

In situ analysis of zircon, Hf isotope signatures were performed in four samples (CLM4A, CLM5, CLM6A, CLM6B) using a Thermo Finnigan Neptune multicollector ICP-MS at the Geoanalytical Lab at Washington State University. The ablation spot size was 40 μm and situated on top of, or adjacent to, the U-Pb age analysis ablation pit. Details of analytical procedures and data treatment follow Vervoort et al. (2004) and DuFrane et al. (2007). For the Hf depleted mantle model ages (HfTDM), we used $^{176}Hf/^{177}Hf$ and $^{176}Lu/^{177}Hf$ for the individual zircon samples to determine their initial $^{176}Hf/^{177}Hf$ ratios at their crystallization ages. Projection back from zircon crystallization was calculated using a present value of 0.0150 for the estimated $^{176}Lu/^{177}Hf$ of continental crust (Vervoort and Patchett 1996; Goodge and Vervoort 2006). The depleted mantle Hf evolution curve was calculated from present-day depleted mantle values of $^{176}Hf/^{177}Hf$ $DM_{(0)}$ = 0.283240 and $^{176}Lu/^{177}Hf$ DM(0) = 0.03979 (Vervoort et al. 2015).

3.4. Whole-rock geochemistry

X-ray fluorescence (XRF) and inductively coupled plasma-mass spectrometry (ICP-MS) at ALS Minerals determined major oxides and trace elements concentrations. The samples were crushed using a jaw crusher and powered using a tungsten carbide ring mill. The powered samples (0.2 g) were weighed into a graphite crucible and mixed with 1.5 g of $LiBO_2$ flux. The crucibles were heated in a furnace to 1050°C for 15 minutes, and the resulting melt was dissolved in 5% HNO_3. Calibration standards and reagent blanks were added to the sample sequence. Sample solutions were aspirated into an ICP emission spectrograph (Jarrel Ash Atom Comb 975) for determining major oxides and certain trace elements (Ba, Nb, Ni, Sr, Sc, Y, and Zr). In contrast, the sample solutions are aspirated into an ICP-MS (Perkin-Elmer Elan 6000) to determine the trace elements, including rare earth elements. All geochemical analyses were handled and processed using the software GCDKit 5.0 (Janoušek et al., 2006).

4. Results

4.1. Sampling and Petrography

The studied granitoids are distributed along the eastern flank of the Central Cordillera. Field observations let us separate these rocks into mylonitic and massive granitoids. The first group outcrops to the north of the Tolima region, near the municipality of Anzoátegui (Fig. 2) and is characterized by an intense deformation defined by augens of quartz and feldspar enveloped by chloritized mafic minerals (amphibole and biotite). These deformational characteristics are shared by the mafic dikes that intrude on the mylonitic granitoids (Fig. 3). Under the microscope, the rocks are fine- to medium-size grained with granonematoblastic texture where hornblende crystals define a preferred orientation (sample GG-8) and are composed of plagioclase (46%), hornblende (31%), quartz (8%), K-feldspar (5%), biotite

(10%), which is entirely replaced by chlorite, and opaque minerals and zircon as the accessory phases (Fig. 4).

The second group of granitoids are massive and outcrops to the south of the Tolima region, along with the municipality of Planadas (Fig. 2). These rocks are phaneritic, hypidiomorphic, and fine to medium-grained plutonic rocks (samples CLM4A, CLM5, CLM6A, CLM6B); the granitoids are constituted by plagioclase (43-63%), quartz (8-14%), K-feldspar (4-25%), biotite (10-19%), hornblende (3-13%) and pyroxenes (2-18% of orthopyroxene in sample CLM5, and clinopyroxene sample CLM6B). Typical accessory minerals are zircon, apatite, and opaque minerals. Chlorite, epidote, sericite, and calcite are common secondary minerals. In addition, microstructures like undulatory extinction in quartz, bent plagioclase (deformed twins), and myrmekites are present in all samples (Fig. 4B, C, D, E). Sample CLM4B is a felsic volcanic rock found as a dike intruding sample CLM4A (Fig. 3D). It has a porphyritic texture with phenocrysts of quartz with embayed texture and hornblende. The matrix is microcrystalline, composed of quartz, plagioclase, hornblende, and secondary minerals such as chlorite and epidote (Fig. 4F).

Figure 3. Field photographs. A: Outcrop at the north of the Tolima region showing the contact relationship between Permian (left) and Triassic rocks (right). B: Hand specimen of sample GG08. C: Hand specimen of sample E4. D: Outcrop at the north of the municipality of Planadas showing sample CLM4B (dike) intruding sample CLM4A (granitoid). E: Hand specimen of sample CLM5. F: Hand specimen of sample CLM6.

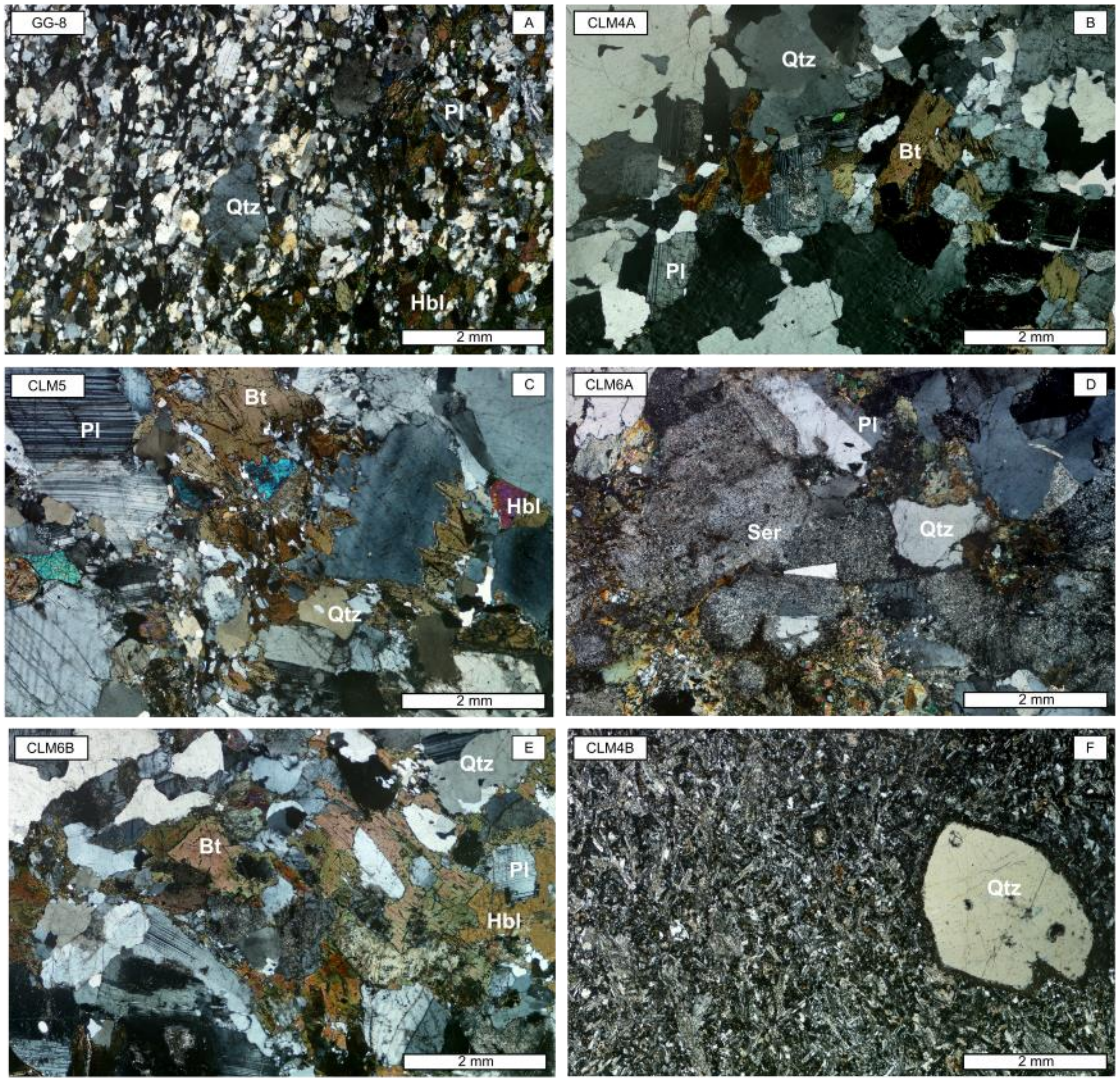

Figure 4. Photomicrographs of samples from the Tolima region. Crossed polarized light: A: GG-8; B: CLM4A; C: CLM5; D: CLM6A; E: CLM6B; F: CLM4B. Qtz = Quartz, Bt= Biotite, Ser= Sericite, Pl=Plagioclase, Hbl= Hornblende.

4.2. Zircon U-Pb ages and Hf isotopes

U-Pb zircon analyses were obtained from five granitoids (samples CLM4A, CLM5, CLM6A, CLM6B, R1) and two mylonitic granitoids (sample E4, GG-8). The resulting U-Pb data are listed in Table 1. Cathodoluminescence (CL) images of representative zircons and weighted average diagrams are shown in Figures 5 and 6. Hf isotope compositions of zircons

from samples CLM4A, CLM5, CLM6A, CLM6B are listed in Table 2 and shown in Figure 7.

Zircon grains from CLM4A (granodiorite) are 120-260 μm in length and 60-140 μm in width. These grains are subhedral, elongated, and present oscillatory zoning as shown in the CL images (Fig. 5A). Th/U ratios vary from 0.2 to 0.8. Thirty zircon grains have $^{206}Pb/^{238}U$ ages (concordance better than 95%) ranging from 269 Ma to 263 Ma and provide a weight average age of 266.8 ± 0.2 Ma (MSWD= 1.1; Fig. 6A), interpreted as the crystallization age. Twenty of the dated zircons have an initial $^{176}Hf/^{177}Hf$ between 0.282602 and 0.282651 and εHf(i) ranging from -0.6 to +1.2 (Fig. 7).

Zircons from CLM5 (diorite) are 150-320 μm in length and 100-200 μm in width. Cathodoluminescence (CL) images show stubby subhedral grains; some exhibit oscillatory or patchy zoning; a few grains are unzoned (Fig. 5B). Th/U ratios range from 0.4 to 0.9. Thirty-eight analyses yield $^{206}Pb/^{238}U$ ages (concordance better than 95%) from 268 Ma to 262 Ma and define a weight average age of 265.9 ± 0.2 Ma (MSWD= 1.1; Fig. 6B), considered as the crystallization age. Twenty of the dated zircons present initial $^{176}Hf/^{177}Hf$ ratios between 0.282602 and 0.282651 and εHf(i) values ranging from -1.5 to +0.9 (Fig. 7).

Zircons grains from CLM6A (diorite) are 120-250 μm in length and 70-120 μm in width. Cathodoluminescence (CL) images show stubby subhedral and anhedral grains that exhibit oscillatory or patchy zoning; there are also unzoned grains (Fig. 5C). Th/U ratios from the analyzed zircons vary from 0.2 to 1.1. Thirty-four zircons yield concordant U–Pb ages (concordance better than 95%) ranging from 275 Ma to 268 Ma and define a weight average age of 272.9 ± 0.2 Ma (MSWD =1.7; Fig. 6C), which represent the crystallization age. One zircon yields a Neoproterozoic age of 594.2 ± 7.8 Ma, interpreted as a xenocrystic

zircon. Eighteen zircons have initial $^{176}Hf/^{177}Hf$ ratios that vary from 0.282589 to 0.282657, and εHf(i) values ranging from -0.9 to +1.6 (Fig. 7).

Zircons from CLM6B (quartz diorite) are 40-300 μm in length and 30-120 μm in width. These grains are stubby and rounded anhedral-subhedral predominantly unzoned as shown in the CL images (Fig. 5D). Th/U ratios vary from 0.2 to 1.0. Thirty-six analyses yield $^{206}Pb/^{238}U$ ages (concordance better than 95%) ranging from 276 Ma to 267 Ma and provide a weight average age of 273 ± 0.2 Ma (MSWD= 2.5; Fig. 6D), interpreted as the crystallization age. One zircon yields a Neoproterozoic age of 577.9 ± 5.1 Ma, representing an inherited zircon. Eighteen zircons have initial $^{176}Hf/^{177}Hf$ ratios of 0.282610 to 0.282660 and εHf(i) values that range from -0.1 to +1.7 (Fig. 7). A xenocrystic zircon (No. 15 with an age of 578 Ma) has an intermediate initial $^{176}Hf/^{177}Hf$ (0.282349) and a lower εHf(i) (-2.5) compared with the other zircons (Fig. 7).

For all the analyzed zircons from sample R1 (granitoid), Th/U ratios range from 0.2 to 1.1. Fourteen analyses yield $^{206}Pb/^{238}U$ ages (concordance better than 95%) ranging from 278 Ma to 271 Ma and provide a weight average age of 275 ± 0.4 Ma (MSWD= 1.5; Fig. 6E), which is considered to represent the time of crystallization (Middle Permian). Two spots yield Mesoproterozoic (1033.4 ± 7.5 Ma) and Neoproterozoic age (930.6 ± 6.4 Ma), related to inherited zircons.

Zircons from sample E4 (mylonitic granitoid) are 52-300 μm in length and 23-130 μm in width. The grains are stubby and elongated subhedral with oscillatory zoning as shown in the CL images (Fig. 5E). Seventy-eight analyses show a range of $^{206}Pb/^{238}U$ ages between 1078 and 145 Ma, where seventy-three analyses yield concordant U–Pb ages (concordance better than 95%), and five analyses are discordant. Th/U ratios vary from 0.01 to 1.2. Twenty-

eight analyses yield $^{206}Pb/^{238}U$ ages ranging from 278 Ma to 252 Ma, providing a weight average age of 273.8 ± 0.4 Ma (MSWD= 1.9; Fig. 6F), which is considered the crystallization age. This sample also presents another significant zircon age population, where twenty-eight spots yield Triassic ages between 250 and 200 Ma. According to CL images and spot ages, some zircons grains have cores yielding Permian ages with rims yielding Triassic ages. These rims (spots CB1-E4-3, 13, 21, 33, 44, 50) define a Concordia age of 228.6 ± 0.8 Ma (MSWD= 1.3; n=6), and present Th/U ratios between 0.05 to 0.2. Four spots are significantly older yielding ages of 1078 ± 18 Ma, 840 ± 14 Ma, 487 ± 15 Ma, and 371.7 ± 6.7 Ma, which is related to xenocrystic zircons; and three spots yield younger age results of ca. 199 – 145 Ma.

Zircons from sample GG-8 (mylonitic granitoid) are 75-190 µm in length and 30-75 µm in width. Cathodoluminescence (CL) images show stubby subhedral and anhedral crystals; some crystals have oscillatory zoning, xenocrystic cores, and signs of local recrystallization. (Fig. 5F). Th/U ratios range from 0.2 to 1.6. Thirty-one analyses show a range of $^{206}Pb/^{238}U$ ages between 373 and 155 Ma, where twenty-four analyses yield concordant ages (concordance better than 95%), and seven analyses are discordant. Eleven analyses yield $^{206}Pb/^{238}U$ ages ranging from 276 Ma to 267 Ma, providing a weight average age of 272.4 ± 0.6 Ma (MSWD= 1.7; Fig. 6G), considered the crystallization age. One spot yield a Devonian age (373.3 ± 8.2 Ma), considered a xenocrystic zircon; six spots yield Triassic ages between 248 and 201 Ma, and two yields younger age results ca. 155 Ma.

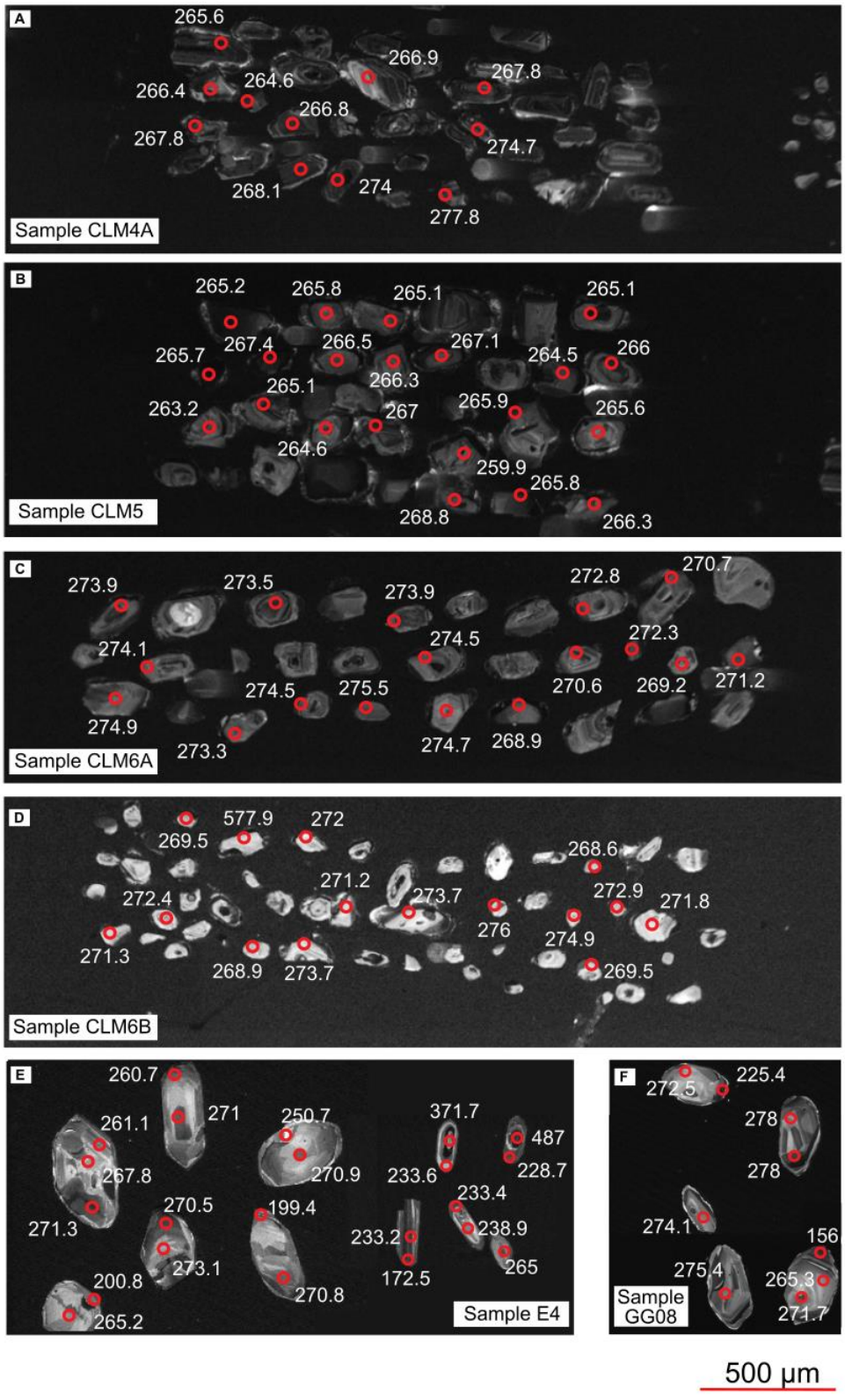

Figure 5. Cathodoluminescence (CL) images of representative zircon grains from samples CLM4A, CLM5, CLM6A, CLM6B, E4, and GG08, showing the location of the analytical spots and age.

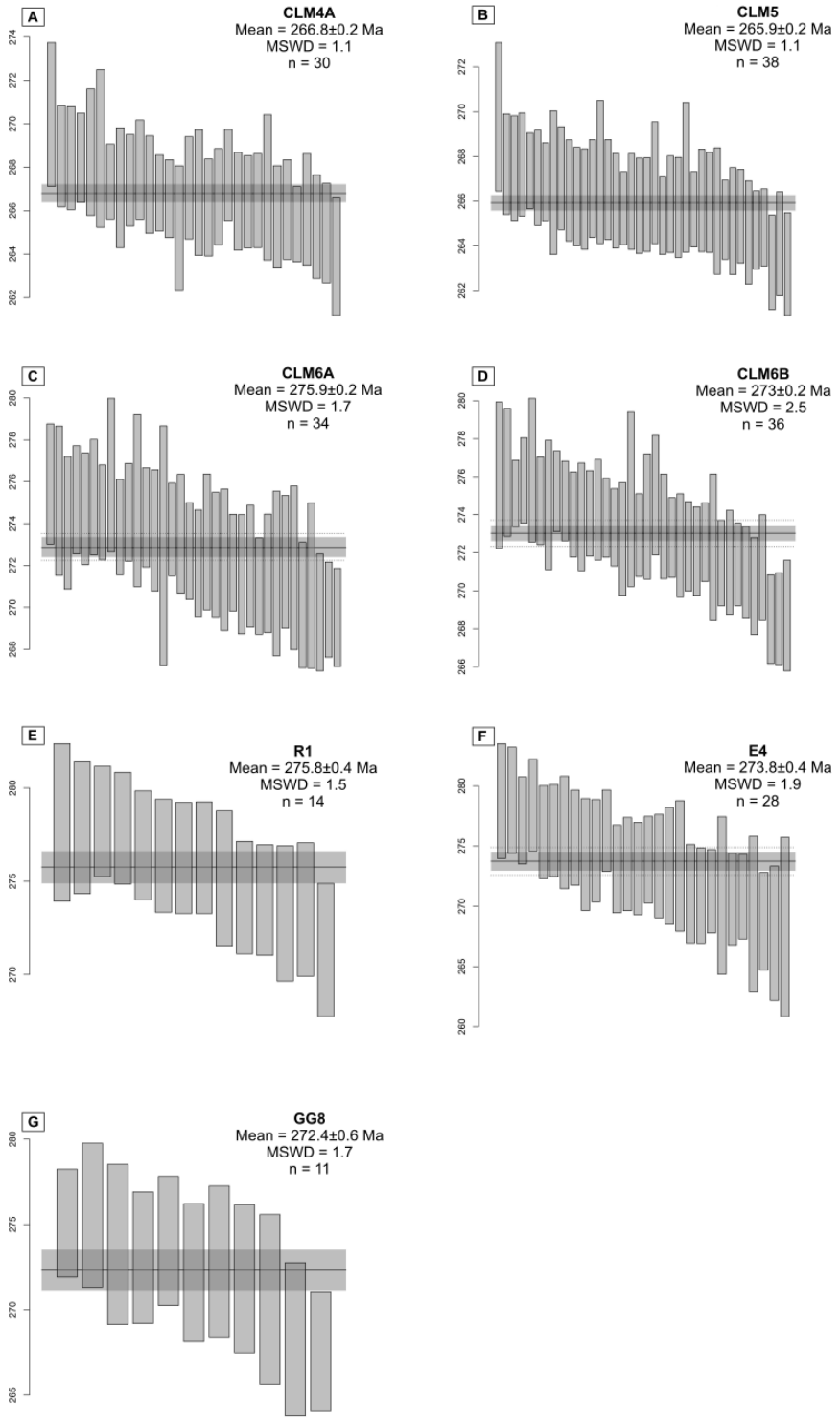

Figure 6. Zircon U-Pb weighted average age diagrams for samples CLM4A, CLM5, CLM6A, CLM6B, R1, E4 and GG8.

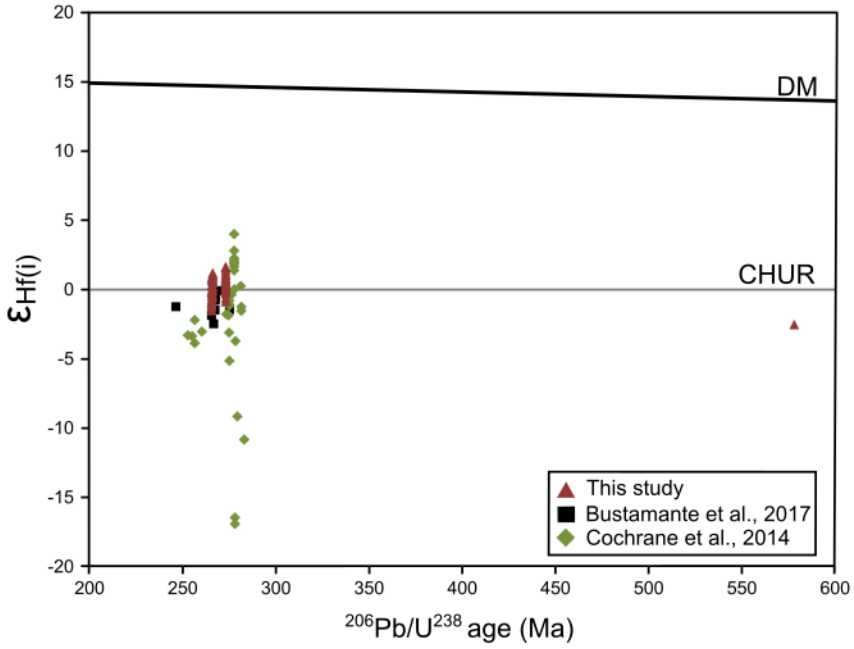

Figure 7. Initial εHf versus $^{206}Pb/^{238}U$ age diagram from samples CLM4A, CLM5, CLM6A, and CLM6B.

4.3. Zircon trace elements

Trace elements in zircons were performed in three samples from the south of the Tolima region (samples CLM4A, CLM5, CLM6). Analytical results are reported in Table 3.

Zircon grains present Hf concentrations ranging from 7890 to 12100 ppm, U vary from 96 to 1234 ppm, Th contents range from 44 to 1735 ppm, Y varies from 225 to 2743, and total REE concentration varies from 217 to 252110 ppm. Th/U ratios range from 0.3 to 1.4, suggesting that they are magmatic zircons (Rubatto, 2002; Hoskin and Schaltegger, 2003; Fig. 8). Chondrite-normalized zircon REE patterns display steep positive slopes from La to Lu ((Lu/La)N = 15.6 – 59118), with enrichment in HREE relative to LREE ((Yb/Sm)N= 19.3–189.8) and positive Ce and negative Eu anomalies (Ce/Ce* = 1.2–126.2; Eu/Eu* = 0.2–0.4; Fig. 9), which is a typical trend for continental arc samples (Hoskin and Schaltegger, 2003).

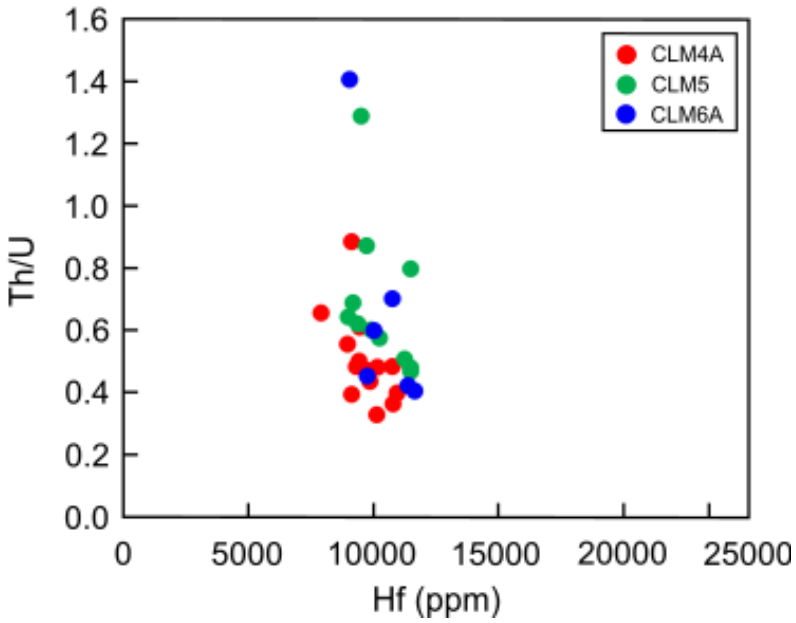

Figure 8. Th/U vs Hf plot for the zircons from the samples CLM4A, CLM5, and CLM6.

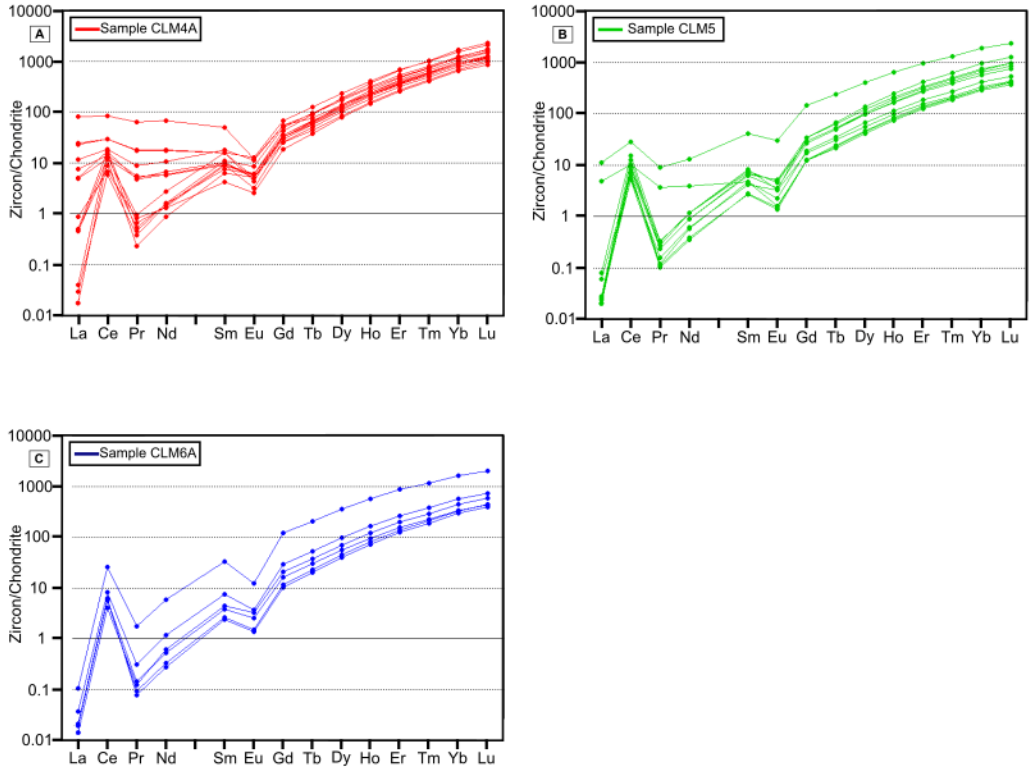

Figure 9. Chondrite-normalized rare earth element (REE) diagrams for samples CLM4A, CLM5, and CLM6 (chondrite values of McDonough and Sun, 1995).

4.4. Whole-rock geochemistry

Major and trace elements data were acquired for six massive granitoids (samples CLM4A, CLM5, CLM6A, A-5, A-6, C-01) and two mylonitic granitoids (samples GG-8, CI12). Analytical results are listed in Table 4.

The granitoids are intermediate to felsic rocks with SiO_2 contents varying from 59.6 to 71.6 wt.% (mean= 64.9 wt.%). The compositional ranges for the other major elements vary between 15.7 and 19.2 wt. % for Al_2O_3, 3.3-10.3 wt.% for Na_2O, 0.3-5.9 wt.% for CaO, 0.1-3.7 wt.% for MgO, and 0.2-3.4 wt.% for K_2O. The mylonitic granitoids range from intermediate to felsic compositions (59.3-71.0 SiO_2 wt.%), and the contents of other major elements vary between 15.5 and 16.9 wt. % for Al_2O_3, 4.2-5.1 wt.% for Na_2O, 3.0-5.5 wt.% for CaO, 0.8-3.6 wt.% for MgO, and 0.9-1.4 wt.% for K_2O.

According to the TAS diagram, the samples are classified as diorite, granodiorite, quartz monzonite, and granite (Fig. 10). In the discrimination diagrams of Frost et al. (2001), the majority of samples plot in the magnesian field, except sample A-5, which plot in the ferroan field (Fig. 10); five samples plot in the calc-alkalic series, whereas samples GG-8, A-5, and A-6 plot in the calcic, alkali-calcic, and alkalic series, respectively (Fig. 10); and the ASI ratios (aluminum saturation index; Al_2O3/ ($CaO + Na_2O + K_2O$) in mol) range between 0.8 and 1.4, indicating a metaluminous to peraluminous nature (Fig. 10). This peraluminous character found in samples CLM-4A, A-5, A-6, and GG-8 could be due to high Al contents produced by the sericitization of plagioclase crystals and the presence of aluminous biotite. Bivariate diagrams show a decrease in TiO_2, Al_2O_3, MgO, CaO, P_2O_5, Fe_2O_3, and Na_2O and an increase in K_2O relative to SiO_2 (Fig. 11).

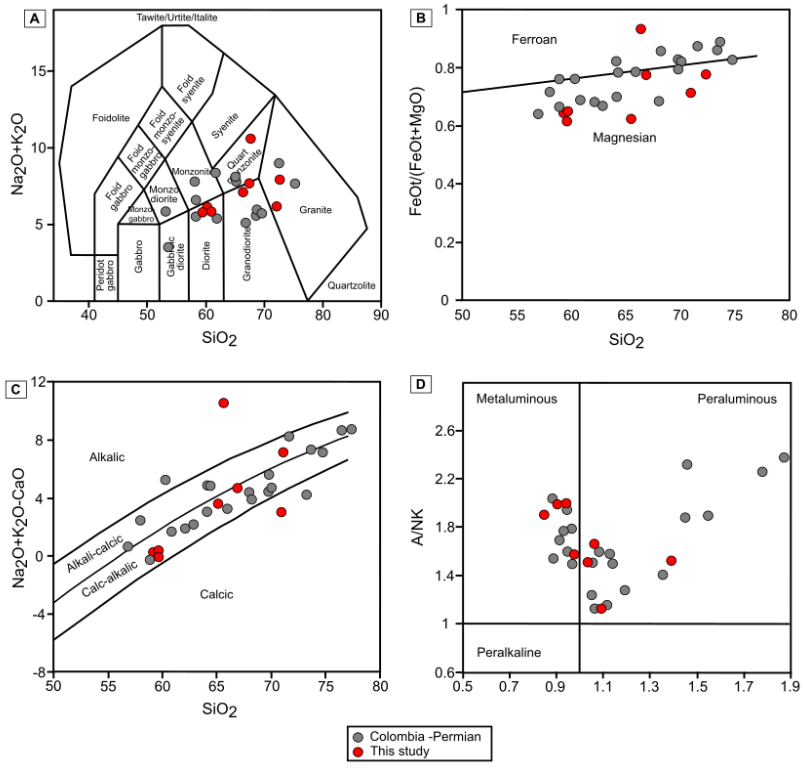

Figure 10. Geochemical classification and discrimination diagrams of plutonic igneous samples from the Tolima region. A: Classification of plutonic rocks based on the TAS diagram of Middlemost (1994). B-D: Discrimination diagrams of Frost et al., (2001). Geochemical data represented in grey circles were compiled from Vinasco et al., (2006), Leal-Mejía (2011), Cochrane et al., (2014), Rodríguez et al., (2014), Rodríguez et al., (2017), and Rodríguez-García et al., (2019).

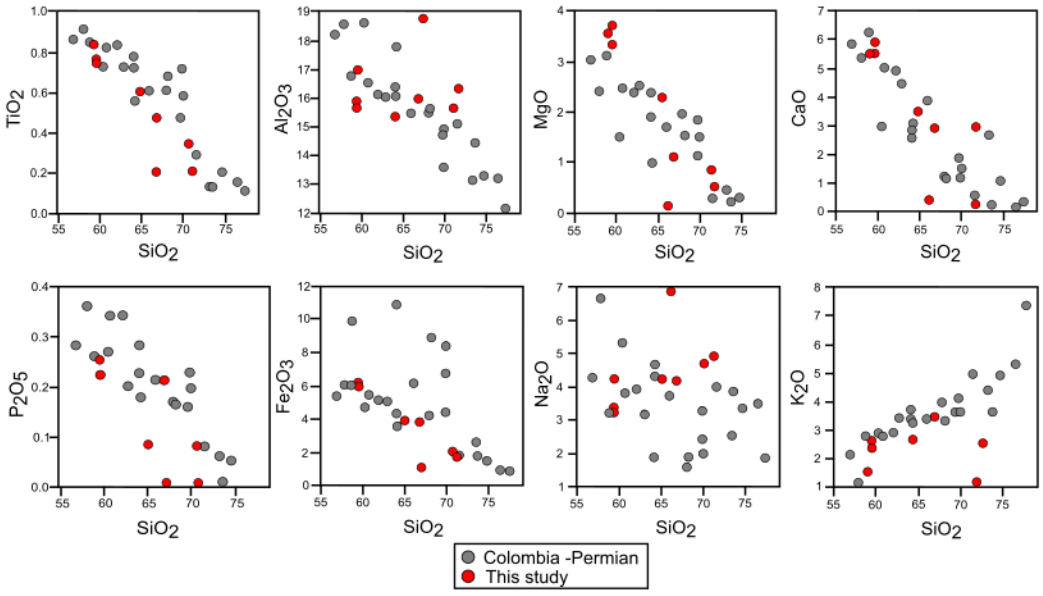

Figure 11. Major elements Harker variation diagrams**.** TiO_2; Al_2O_3; MgO; CaO; P_2O_5; Fe_2O_3; Na_2O; K2O vs. SiO_2. Geochemical data represented in grey circles were compiled from Vinasco et al., (2006), Leal-Mejía (2011), Cochrane et al., (2014), Rodríguez et al., (2014), Rodríguez et al., (2017), and Rodríguez-García et al., (2019).

According to the REE diagram normalized to chondrite from both granitoids and gneisses (Boynton, 1984; Fig. 12), the samples have moderate to steep REE patterns ((La/Yb)N = 9.3-34.3), show enrichment in LREE compared with HREE ((La/Sm)N= 3.4-7.0, (Tb/Yb)N=1.3-2.9), LREE-MREE slope is steep negative ((La/Dy)N=7.6-30.5), and MREE-HREE slope is predominantly flat-shaped ((Dy/Yb)N=1.1-2.2); the HREE slope pattern for samples A-5, A-6, and GG-8 is steep negative and strongly concave-upward; these samples have lower total REE concentrations (37.6 ppm, 61.2 ppm, and 70.9 ppm, respectively). Eu anomalies vary from slightly negative to positive (Eu/Eu*=0.8-1.5). Multi-element diagrams normalized to the primitive mantle (Sun and McDonough, 1989; Fig. 12) show substantial depletion in Nb, P, Ti, and HFSE contents, typical of subduction-related magmatic rocks. Within the tectonic discrimination diagrams of Pearce et al. (1984), all the data points plot within the volcanic arc field (VAG) (Fig. 13).

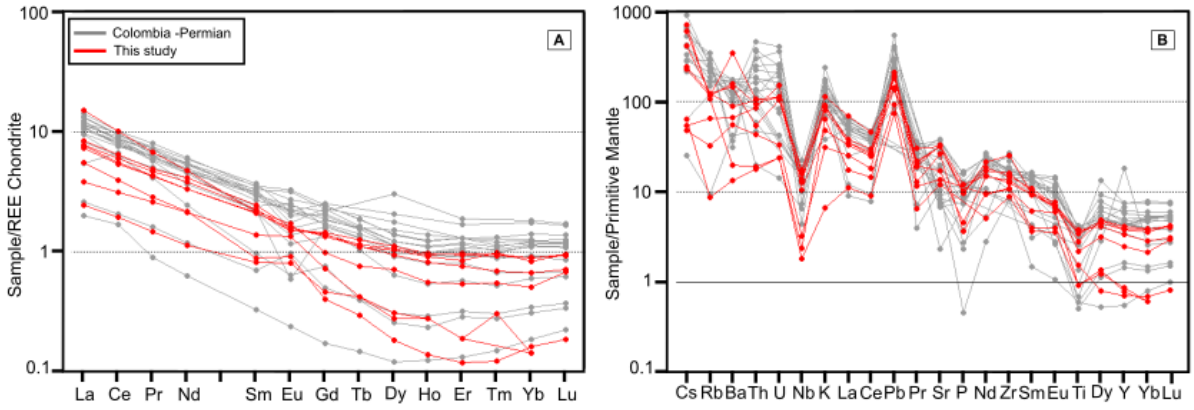

Figure 12. A: Chondrite normalized REE patterns, according to Boynton (1984) and B: Multi-element plot normalized to primitive mantle according to Sun and McDonough (1989). Geochemical

data represented in grey patterns were compiled from Vinasco et al., (2006), Leal-Mejía (2011), Cochrane et al., (2014), Rodríguez et al., (2014), Rodríguez et al., (2017), and Rodríguez-García et al., (2019).

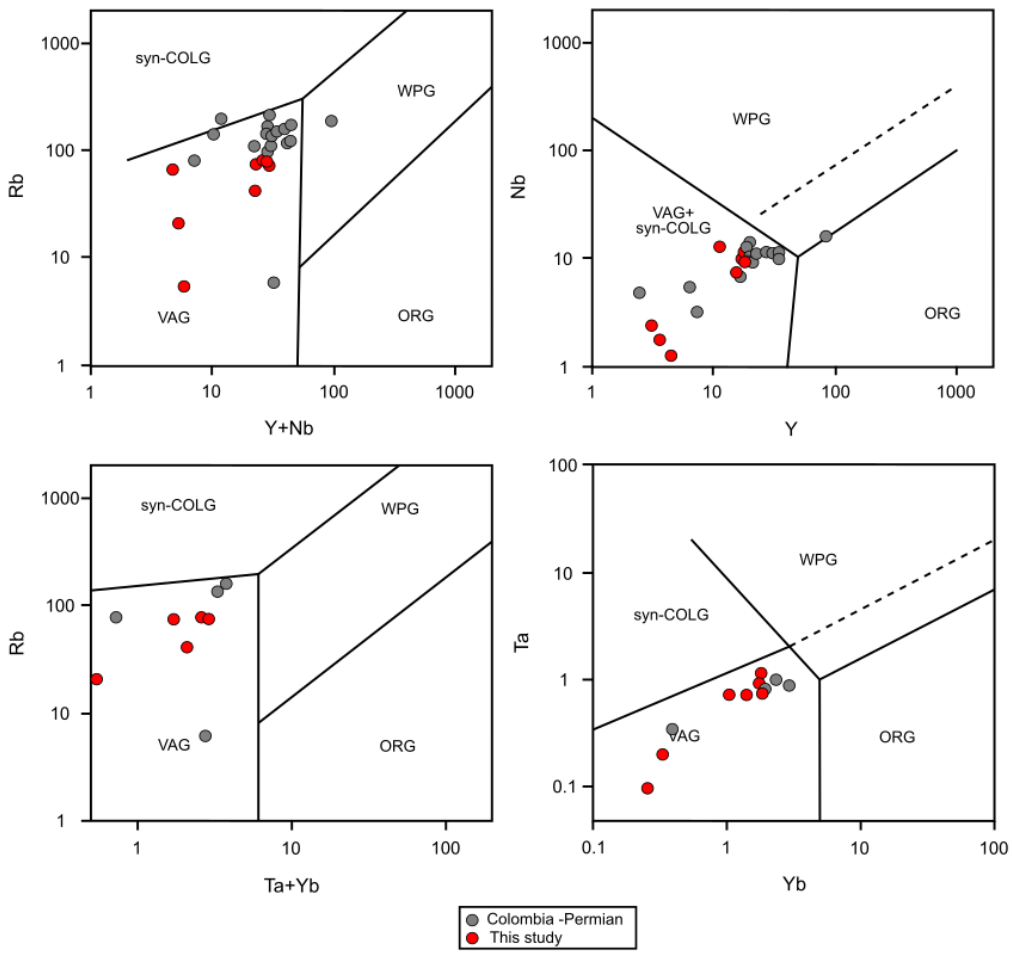

Figure 13. Granitoid tectonic discrimination diagram according to Pearce et al. (1984). Fields for syn-collision (syn-COLG), volcanic arc (VAG), within plate (WPG), and ocean ridge (ORG) granites are indicated. Geochemical data represented in grey circles were compiled from Vinasco et al., (2006), Leal-Mejía (2011), Cochrane et al., (2014), Rodríguez et al., (2014), Rodríguez et al., (2017), and Rodríguez-García et al., (2019).

5. Discussion

5.1. Duration of the Permian arc magmatism

Our new U-Pb crystallization ages record a magmatic activity between 276 and 265 Ma that corresponds to the most significant peak of the Permian magmatism of the Northern Andes (Rodríguez-García et al., 2019; Spikings and Paul, 2019). Furthermore, Th/U ratios between 1.6 and 0.2 in the analyzed zircons suggest that they have a magmatic origin (Rubatto et al., 2002), which means that we are reporting crystallization ages and no metamorphic events were recorded. Intrusive and metamorphic rocks with similar ages have been reported along the Central Cordillera and the Sierra Nevada de Santa Marta, in the Tierradentro gneisses (Bustamante et al., 2017), La Plata and Ortega granites (Rodríguez-García et al., 2019), and El Encanto orthogneiss (Piraquive et al., 2021).

The existence of fragments of Permian magmatism along southern North America and Central America (Weber et al., 2007; Arvizu et al., 2009; Ortega-Obregón et al., 2014; Cecil et al., 2019), the Paraguaná Península in Venezuela (El Baúl Massif: Viscarret et al., 2009; van der Lelij et al., 2016); the Serranía de Perijá and Maracaibo Lake (Espejo et al., 1980; Dasch, 1982; Feo-Codoecido et al., 1984), to the south of the Cordillera Real in Ecuador (Paul et al., 2018), the central Eastern Cordillera of Perú (Mišković et al., 2009), and along the Frontal and Domeyko Cordilleras in Northern Chile (Coloma et al., 2017; Oliveros et al., 2020) account for a protracted magmatic activity during the Permian at the western margin of Gondwana. This is important because we are recording the prolongation of this arc-related magmatism in the northern Andes, where this remained unrecognized for many years (see Rodríguez-García et al., 2019 and Spikings and Paul, 2019 for a review).

Although the Permian crystalline basement is poorly exposed in the northern Andes because it may have been intensively eroded, covered by thick layers of vegetation, or confused during early cartographic works with the youngest intrusive rocks of similar

composition (i.e., Jurassic batholiths); the ~ 40 m.y. of magmatic activity could be imaged in its detrital record (Barth et al., 2013). Detrital zircons from different sedimentary basins along the Middle Magdalena Valley and Eastern Cordillera (Nie et al., 2010; Horton et al., 2010; Saylor et al., 2011; Bayona et al., 2013; Caballero et al., 2013; Silva et al., 2013) show an increase in the crystallization age population between 290 and 260 Ma, which can be related with an increase of the volume of magma produced in this time interval, probably because of the early stages of the magmatic arc (Fig. 14). A comparison of U-Pb ages obtained in both detrital zircons and *in-situ* rocks shows a similar distribution, indicating that the most significant peak of magmatic activity occurred at ~ 270 Ma. The further decrease might be related to plate reorganizations derived in the Pangea break up and the dominance of extensional tectonics (Vinasco et al., 2006; Spikings and Paul, 2019).

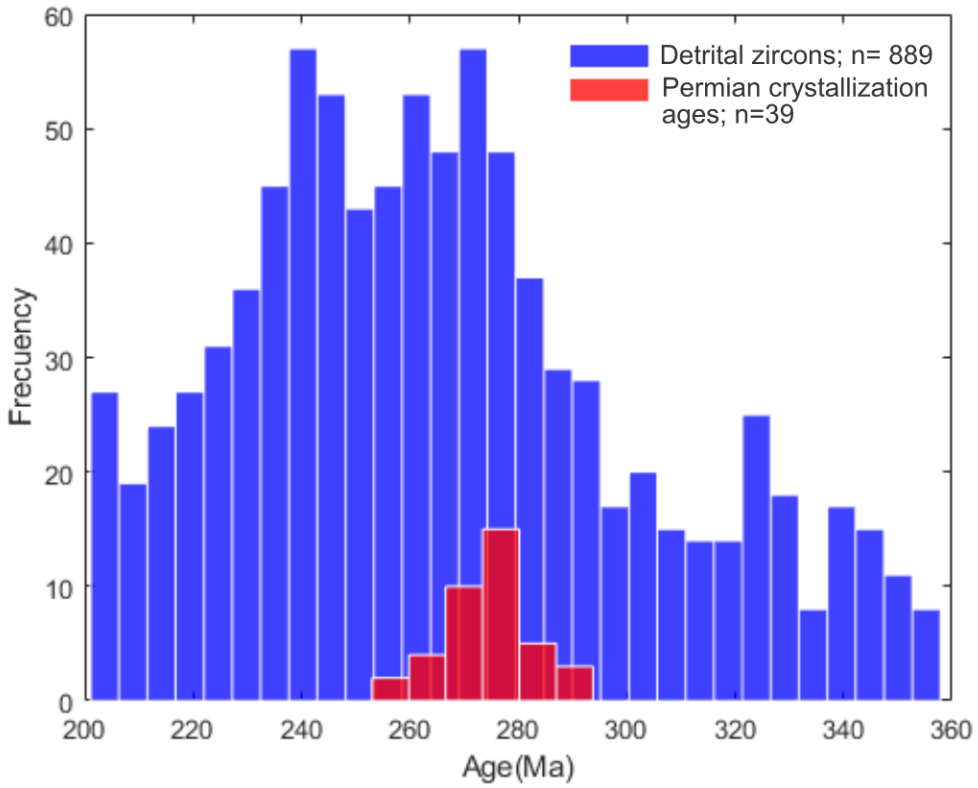

Figure 14. Histogram of detrital U-Pb zircon ages from sedimentary basins from the Middle Magdalena Valley and the Eastern Cordillera (blue bars) and $^{206}Pb/^{238}U$ ages from Permian intrusive

and metamorphic rocks from the Sierra Nevada de Santa Marta, the Serranía de San Lucas, and the Central Cordillera (red bars). Data of detrital U-Pb ages compiled from Nie et al. (2010), Horton et al. (2010), Saylor et al. (2011), Bayona et al. (2013), Caballero et al. (2013), and Silva et al. (2013). Data of Permian intrusive and metamorphic rocks compiled from: Vinasco et al., (2006); Cardona et al., (2010); Villagómez et al., (2011); Cochrane et al., (2014); Bustamante et al., (2017); Rodríguez et al., (2017); Paul et al., (2018); Rodríguez-García et al., (2019); Leal-Mejía et al., (2019); Piraquive et al., (2021).

The magmatic history could be tracked back if we consider the inherited zircons with Paleozoic crystallization ages and even Meso-Neoproterozoic ages. The latter suggests that the Permian intrusives of the Central Cordillera assimilated an older continental crust, probably rocks of a Carboniferous magmatic arc, as suggested in the U-Pb ages reported by Leal-Mejía et al. (2019) to the north of the Central Cordillera. Although it is out of the scope of this work, we speculate that arc magmatism may have been active since the Carboniferous and that the Permian granitoids record the resurgence of this magmatism. Nevertheless, additional work on older lithologies is needed to constrain the magnitude of this older arc-related magmatism fully.

5.2. Origin of the magmas

The models proposed to explain the tectonic setting of the Permian magmatism of the northern Andes includes i) a collisional event that produced partial melting of the continental crust and a regional metamorphic event (Vinasco et al., 2006) and ii) a continental arc which is part of a broader magmatic province that extends along the western margin of Gondwana (Cardona et al., 2010; Spikings and Paul, 2019; Rodríguez-García et al., 2019). The generation of S-type granitoids characterizes the first scenario. These rocks are commonly regarded as products of continental collisions and intraplate orogenies (Healy et al., 2004; Sheppard et al., 2003; Sylvester, 1998). However, this type of granitoids could also be formed in continental arc settings in different situations: during early stages or arc magmatism

(Ducea et al., 2015); associated with back-arc extension (Collins et al., 2008); or as a result of a progressive increase of metasedimentary components towards the interior of the continent (Liew and Hofmann, 1988; Collins, 1998). For example, in Colombia, Permian S-type granitoids have been reported in different units (Vinasco et al., 2006; Leal-Mejía et al., 2019; Cochrane et al., 2014) along with metaluminous I-type granitoids (Fig. 10d; see Rodríguez-García et al., 2019 and references therein), showing that these different types of magmatism formed synchronously. Therefore, the coexistence of these two types of granitoids could be explained by the occurrence of different genetic processes and the participation of different sources (i.e., partial melting of mafic lower crust/lithospheric mantle and crustal metasediments) in variable proportions within a continuous subduction-related setting (Grosse et al., 2011; Pankhurst et al., 2000). Hence, a collisional setting is not required to explain the S-type granitoids (Vinasco et al., 2006), as the evolution of the source seems a more feasible explanation.

Whole-rock geochemistry of the studied granitoids shows a calc-alkaline character. In addition, their trace element concentrations show LREEs and LILEs enrichments and negative Nb and Ti anomalies; these are characteristics of subduction-related magmatic rocks, suggesting that these rocks were formed in a continental arc setting. The trace element discrimination diagram further confirms this interpretation since all the samples fall into the volcanic arc granite field (VAG; Fig. 13). The latter is also supported by zircon trace elements data showing high zircon HREE over LREE chondritic normalized contents and distinct positive Ce and negative Eu anomalies, characteristic of continental arc rocks.

According to the discrimination diagrams of Whalen et al. (1987), most of the granitoids plot in the unfractionated granites field (Fig. 15A, B). Biotite and hornblende are

widespread in the investigated granitoids, and there is an absence of Al-rich minerals such as muscovite, garnet, or cordierite; additionally, the samples are metaluminous to weakly peraluminous and have an A/CNK <1.1, and the P_2O_5 concentrations are negatively correlated with SiO_2 contents (Fig. 11), which favor an I-type affinity. This can be further supported by the Y vs. Rb and Th vs. Rb diagrams (Fig. 15C, D), where most samples lie along with the I-type trend.

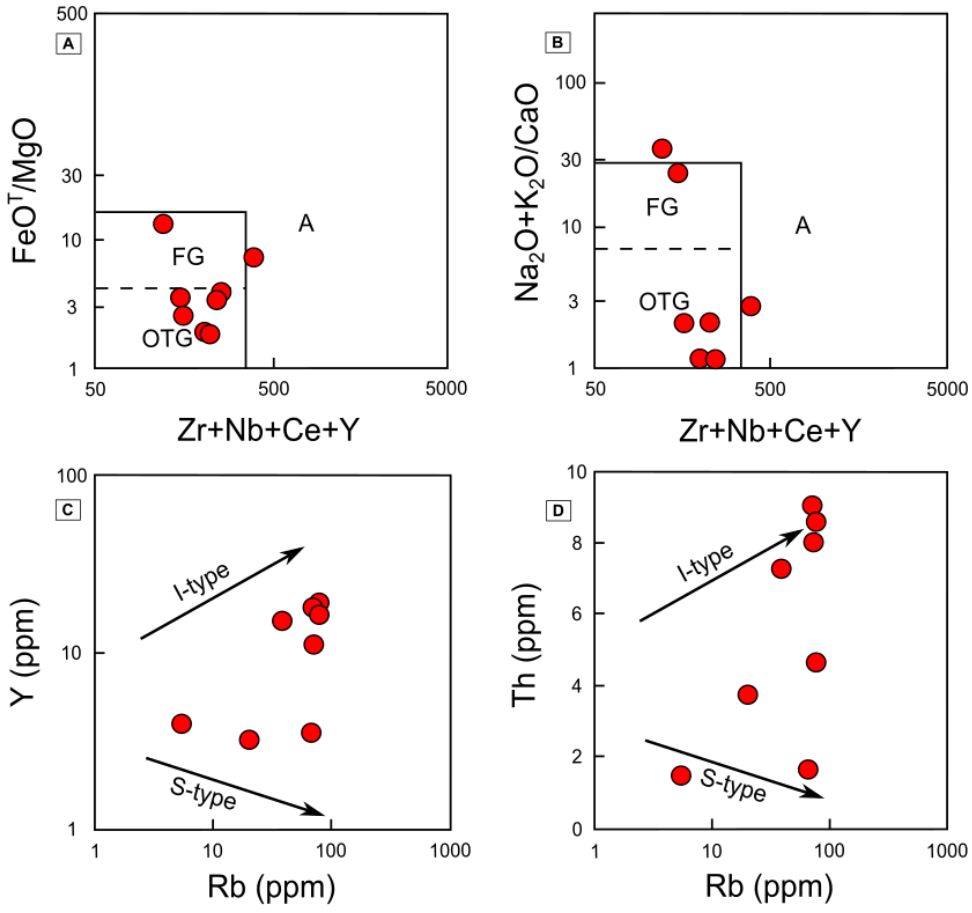

Figure 15. Petrogenetic discrimination diagrams for the massive and mylonitic granitoids from Tolima region. A: FeOT/MgO vs. Zr+Nb+Ce+Y; B: (K2O+Na2O/CaO) vs. Zr+Nb+Ce+Y (after Whalen et al., 1987). FG: Fractionated felsic granites; OTG: unfractionated M-, I- and S-type granites; A: A-type granites. C: Y vs. Rb; D: Th vs Rb (after Chappell, 1999).

The studied granitoids are also characterized by enrichment in LREEs and large-ion lithophile elements (LILEs), a depletion in HREEs and high field strength elements (HFSEs), and negative Eu anomalies, which suggest that the magma was originated from partial melting of crustal material (He et al., 2018). The behavior of La/Sm vs. La, Zr/Nb vs. Zr, and Th/Hf vs. Th support this idea, where the granitoids plot along with the partial melting trend (Xie et al., 2021; Fig. 16), discarding magma mixing and fractional crystallization as potential processes in the genesis of these magmas. The intermediate to high SiO_2 contents (59.3 -71.6 wt%) and high Na_2O/K_2O ratios (1.2-51.5) with moderate Mg# values (22.7-38.2) indicate a strong crustal signature. According to the petrogenetic diagrams of Patiño Douce (1999) and Altherr et al. (2000) (Fig. 17), most of the samples plot in the fields of amphibolite and partial melts from metabasaltic to metatonalitic sources, and two samples (A-5, A-6) plot in the metapelite and partial melts from metapelitic source fields, suggesting that the source may have a combination of basic igneous rocks such as basalts or amphibolites and, to a lesser extent, clay-rich sedimentary rocks.

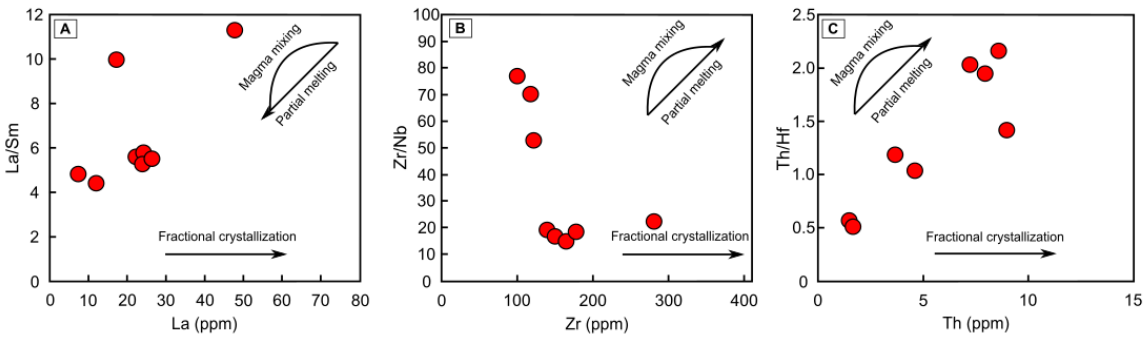

Figure 16. Plots of the massive and mylonitic granitoids from Tolima region. A: La vs. La/Sm; B: Zr vs. Zr/Nb; and C: Th vs. Th/Hf.

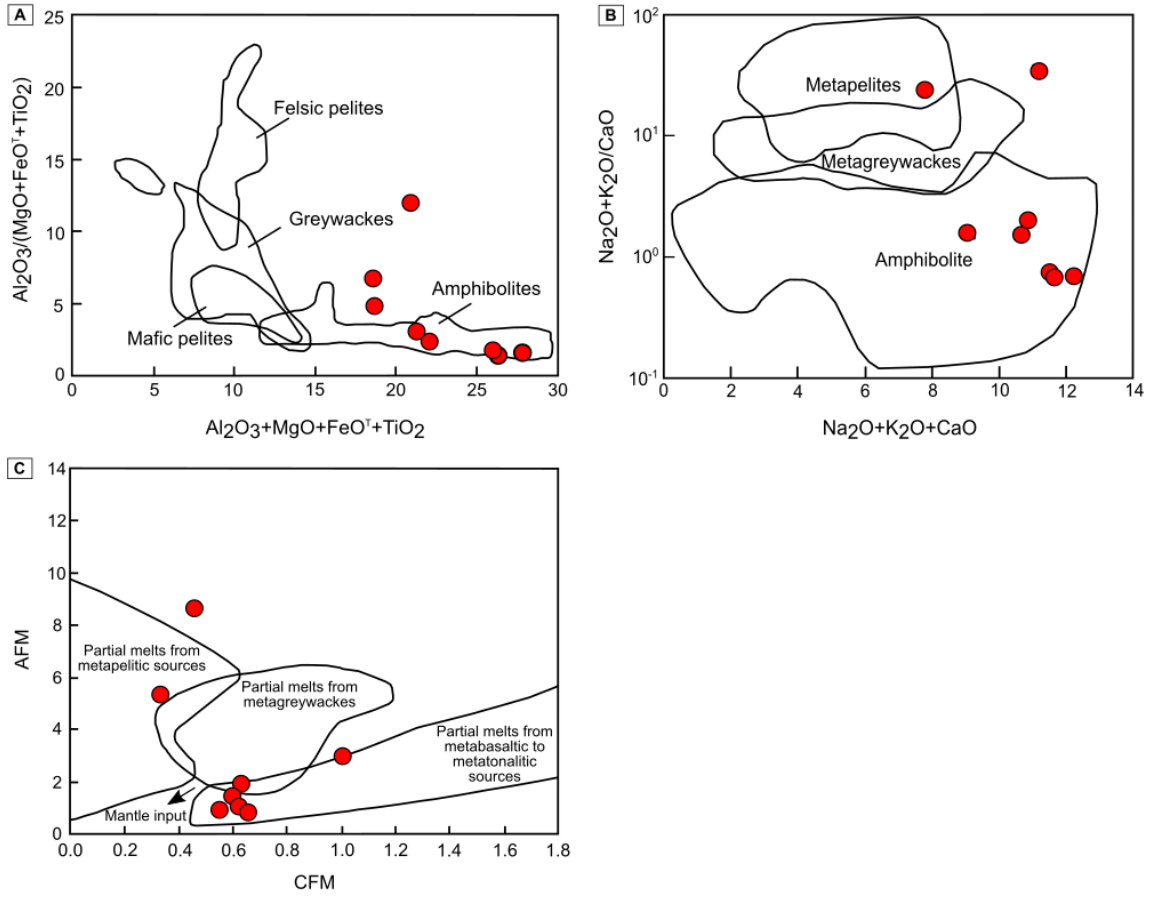

Figure 17. A: Al2O3/(FeO + MgO + TiO2) versus Al2O3 + FeO + MgO + TiO2 diagram, fields and trends are after Patiño Douce (1999) B: Plot of Na2O + K2O + CaO vs. (Na2O + K2O)/CaO after Patiño Douce (1999) C: Molar Al2O3/(FeOT + MgO) (AFM) versus molar CaO/(FeOT + MgO) (CFM) diagram after Altherr et al.(2000).

Furthermore, the variable $\varepsilon Hf_{(i)}$ values ranging from -1.5 to +1.7 reflect the influence of a crustal source in the genesis of these rocks. Although such initial Hf isotopic values suggest a mantelic source and considerable crustal assimilation of the magmas, orthopyroxene-bearing granitoids (sample CLM-5) and the common presence of clinopyroxene mantled by amphibole are indicative of partial melting of a deep and primarily dry heterogeneous crustal basement. However, fluid contribution, probably from the altered subducting slab, that allowed the stabilization of biotite and hornblende in conjunction with

pyroxene is required (Frost et al., 2000). Similar isotopic signatures were reported for Permian lithologies located north of the Tolima region (Cochrane et al., 2014; Bustamante et al., 2017; Fig. 7). In addition, Nd-Sr isotopes obtained in granitic gneisses collected along the western flank of the Central Cordillera by Vinasco et al. (2006) suggest a crustal source with a primary contribution of mantle input. Such continental crust with a Gondwana affinity may have been heterogeneous as imaged in the older xenocrystic zircons with Paleozoic to Proterozoic ages.

Further evidence suggests that partial melting and magmatic differentiation occurred in a thick crust. Our chemical compositions show that Eu anomalies are subtle negative to positive (Eu* from 0.8 to 1.5), suggesting that the plagioclase was not an important residual phase in the source region. Conversely, hornblende and garnet seem to have been the most important fractionating phases during partial melting due to the correlation between Dy/Yb and Nb/Ta (Fig. 18; Xie et al., 2021) and the significant enrichment in LREE when compared with HREE (Fig. 12). The latter is probably the result of a thick continental crust that influenced the degree of magma assimilation.

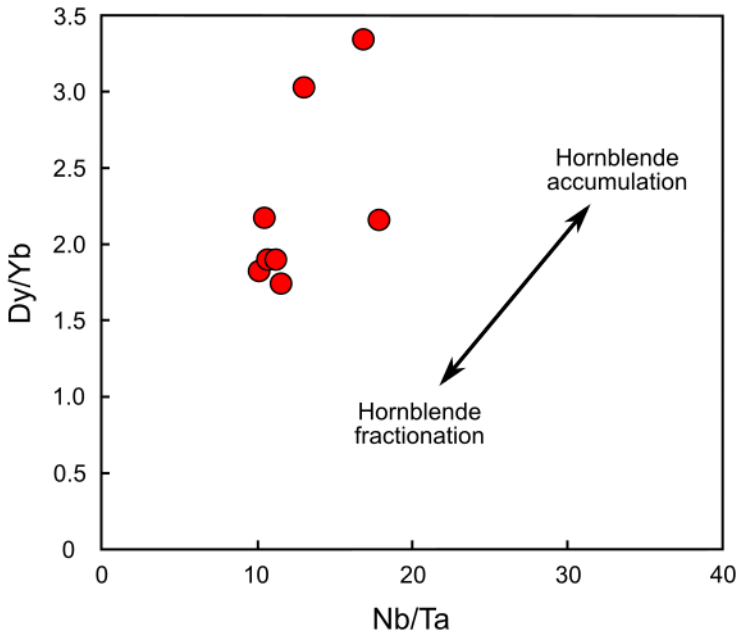

Figure 18. Dy/Yb vs. Nb/Ta (Xie et al., 2021) plot of the massive and mylonitic granitoids from Tolima region.

This scenario is coherent with the high Sr/Y ratios found in samples CLM4A, CLM5, and CLM6A (39.1-59.4; average 45.3), which indicate that the samples could have been formed from a thick crust at elevated pressures where garnet and amphibole are stable (Chapman et al., 2015; Profeta et al., 2016). Additionally, a setting where magma differentiation of the melts occurred in the stability field of garnet at the base of a thick crust could explain the adakite-like signatures of samples GG08, A5, and A6 (Castillo, 2012). Also, information obtained from Ti-in-zircon (T_{ZircTi}; Watson et al., 2006 Eq [7]) and zircon saturation thermometers ($T_{Zircsat}$; Watson and Harrison, 1983 Eq [2]) follows these assumptions. T_{ZircTi} shows an average crystallization temperature for zircon ranging from 620-755 °C. $T_{Zircsat}$ is slightly low and varies from 754 to 805 °C (average 784 °C). According to Miller et al. (2003), granitoids with zircon saturation temperatures lower than 800°C were emplaced in environments of crustal thickening. The coincidence of the thick crust

characteristics with the time interval of peak magmatic production suggests that the crustal growth was probably controlled by magmatic addition.

5.3. Tectonic setting of the magmatism

The geochemical and isotopic data have shown that the samples from the Tolima region were formed within a convergent arc-related setting originated as a consequence of the subduction of the Panthalassa oceanic crust at the western Gondwana margin, where the magmas were generated by partial melting of a heterogeneous thick crust (Fig. 19). Additionally, the massive and mylonitic granitoids are temporally and compositionally correlated with other Permian rocks in Colombia and rocks found along the Andes.

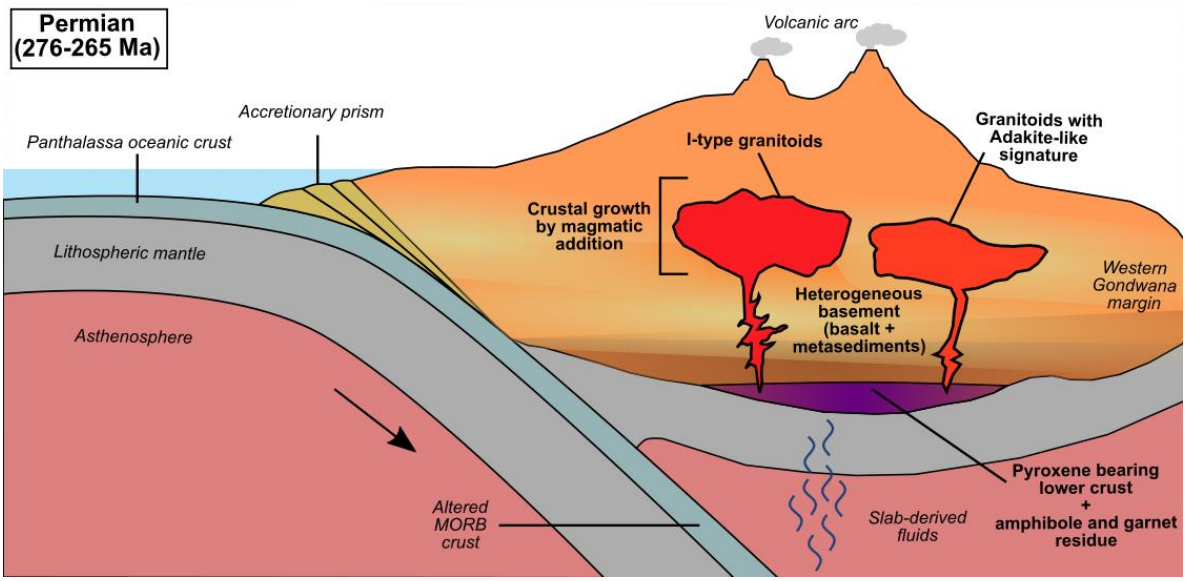

Figure 19. Schematic diagram (not at scale) showing the processes involved during the formation of the granitoids from the Tolima region. The granitoids were formed within a continental arc at the western Gondwana margin between 276 and 265 Ma, where magmas were originated by the partial melting of a heterogeneous crust (composed of a combination of basalts and metasedimentary rock), at the base of a thick crust where pyroxene, garnet, and amphibole are stable.

The timing and cause of the deformation and metamorphism that affected Permian intrusions in the Central Cordillera and the Sierra Nevada de Santa Marta have not been fully

constrained. Vinasco et al. (2006) and Piraquive et al. (2021) suggest a regional metamorphic event at ca. 280-260 Ma coeval with the magmatic event due to a collisional setting associated with the agglutination of the Pangea supercontinent. In contrast, Cardona et al. (2010) and Spikings and Paul (2019) suggest a high-temperature deformational event at ~250 Ma produced by compression along the western margin of Pangea. However, Bustamante et al. (2017) reported Triassic mafic rocks intruding Permian felsic rocks, and both record a mylonitic deformation that may have occurred during or after the Triassic. This intrusive relationship is also registered in sample E4 in both field relationships (Fig. 3c) and the presence of zircon grains characterized by having Permian cores with Triassic rims (Fig. 6). The latter indicates that the Triassic event, dominated mainly by mafic dikes due to the extensional tectonics (Spikings and Paul, 2019), allowed the partial melting of the Permian quartz-feldspathic basement that re-intruded the mafic rocks (back-veining). Later, the Permian arc-related rocks and the Triassic mafic intrusions were mylonitized. A possibility is that such deformation occurred when these rocks were located in a tectonic position different from their place of emplacement in the crust, and the deformation may have been related to the transpressive to transtensive setting recorded in the Jurassic (Bustamante et al., 2016; Bayona et al., 2020). However, additional structural and geochronological data are needed to refine this hypothesis.

6. Conclusion

U-Pb geochronology of Permian massive and mylonitic granitoids from the Central Cordillera of Colombia, combined with geochemical and isotopic signatures, suggests that these rocks are part of a continental arc formed as a consequence of the subduction of an oceanic crust beneath the western margin of Gondwana. The studied rocks are metaluminous

to weakly peraluminous I-type granitoids between 273 and 265 Ma (peak interval). The magmas were originated from the high-temperature partial melting of a heterogeneous crustal source as suggested by the common presence of pyroxene, the zircon inheritances, the geochemical characteristics, and the Hf isotopes in zircons. The deformation patterns observed in the field, which also affected Triassic mafic dikes, may be related to a broad strike-slip deformation that was identified during the Jurassic. The intrusion of these mafic dikes produced a back-veining during the Triassic extension, as recorded in the ca. 229 Ma zircon overgrowths.

7. Acknowledgments

This study was funded by the Vicerrectoría de Ciencia, Tecnología e Innovación of Universidad EAFIT and it is part of the project "El supercontinente Pangea y su registro en los Andes de Colombia" (Project N° 000037). Authors are grateful to Agustin Cardona, Alejandro Beltrán, Victor A. Valencia, Cyril Chelle-Michou, and Luisa Fernanda Chavarría for providing support in the acquisition of geochemical, geochronological, and isotopic data. This is a contribution to the Semillero de Investigación en Mineralogía y Petrología.

References

Acosta, J.E., Guatame, R., Caicedo, J.C., Cárdenas, J.I., 2002. Memoria explicativa de la plancha geológica 245 Girardot. INGEOMINAS.

Altherr, R., Holl, A., Hegner, E., Langer, C., Kreuzer, H., 2000. High-potassium, calc-alkaline I-type plutonism in the European Variscides: northern Vosges (France) and northern Schwarzwald (Germany). Lithos, 50, 51–73. https://doi.org/10.1016/S0024-4937(99)00052-3

Arvizu, H.E., Iriondo, A., Izaguirre, A., Chávez–Cabello, G., Kamenov, G.D., Solís–Pichardo, G., Foster, D.A., Lozano–Santa Cruz, R., 2009. Rocas graníticas pérmicas en la Sierra Pinta, NW de Sonora, México: Magmatismo de subducción asociado al inicio del

margen continental activo del SW de Norteamérica. Revista Mexicana de Ciencias Geológicas, 26(3): 709–728.

Avellaneda-Jiménez, D.S., Cardona, A., Valencia, V., Barbosa, J.S., Jaramillo, J.S., Monsalve, G., Ramírez-Hoyos, L., 2020. Erosion and regional exhumation of an Early Cretaceous subduction/accretion complex in the Northern Andes. International Geology Review, 62, 186-209. https://doi.org/10.1080/00206814.2019.1596042

Barth, A. P., Wooden, J. L., Jacobson, C. E., Economos, R. C., 2013. Detrital zircon as a proxy for tracking the magmatic arc system: The California arc example. Geology, 41(2), 223-226. https://doi.org/10.1130/G33619.1

Bayona, G., Cardona, A., Jaramillo, C., Mora, A., Montes, C., Caballero, V., Mahecha, H., Lamus, F., Montenegro, O., Jimenez, G., Mesa, A., Valencia, V., 2013, Onset of fault reactivation in the Eastern Cordillera of Colombia and proximal Llanos Basin; response to the Caribbean–South American convergence in early Palaeogene time, in Nemčok, M., Mora, A., and Cosgrove, J.W., eds., Thick-Skin–Dominated Orogens: From Initial Inversion to Full Accretion: Geological Society of London Special Publication 377, 285–314

Bayona, G., Bustamante, C., Nova, G., Salazar–Franco, A.M., 2020. Jurassic evolution of the northwestern corner of Gondwana: Present knowledge and future challenges in studying Colombian Jurassic rocks. In: Gómez, J. & Pinilla–Pachon, A.O. (editors), The Geology of Colombia, Volume 2 Mesozoic. Servicio Geológico Colombiano, Publicaciones Geológicas Especiales 36, p. 171–207. Bogotá. https://doi.org/10.32685/pub.esp.36.2019.05

Blanco-Quintero, I.F., García–Casco, A., Toro, L.M., Moreno, M., Ruiz, E.C., Vinasco, C.J., Cardona, A., Lázaro, C., Morata, D., 2014. Late Jurassic terrane collision in the northwestern margin of Gondwana (Cajamarca Complex, eastern flank of the Central Cordillera, Colombia). International Geology Review, 56, 1852–1872. http://dx.doi.org/10.1080/00206814.2014.963710.

Boynton, W.V., 1984. Geochemistry of the rare earth elements: meteorite studies. In: Henderson, P. (Ed.), Rare Earth Element Geochemistry. Elsevier, Volume 2, Chapter 3. 63–114. https://doi.org/10.1016/B978-0-444-42148-7.50008-3

Bustamante, C., Cardona, A., Bayona, G., Mora, A., Valencia, V., Gehrels, G., Vervoort, J., 2010. U-Pb LA-ICP-MS geochronology and regional correlation of Middle Jurassic intrusive rocks from the Garzon Massif, Upper Magdalena Valley and Central Cordillera, Southern Colombia. Boletín de Geología, 32, 93-109.

Bustamante, A., Juliani, C., Hall, C.M., Essene, E.J., 2011. 40Ar/39Ar ages from blueschists of the Jambaló region, Central Cordillera of Colombia: implications on the styles

of accretion in the Northern Andes. Geologica Acta, 9, 351-362. https://doi.org/10.1344/105.000001697

Bustamante, A., Juliani, C., Essene, E.J., Hall, C.M., Hyppolito, T., 2012. Geochemical constraints on blueschist– and amphibolite–facies rocks of the Central Cordillera of Colombia: The Andean Barragán region. International Geology Review, 54, 1013–1030. https://doi.org/10.1080/00206814.2011.594226

Bustamante, C., Archanjo, C.J., Cardona, A., Vervoort, J.D., 2016. Late Jurassic to Early Cretaceous plutonism in the Colombian Andes: a record of long-term arc maturity. Geological Society of America Bulletin, 128, 1762–1779. https://doi.org/10.1130/B31307.1.

Bustamante, C., Archanjo, C.J., Cardona, A., Bustamante, A., Valencia, V.A., 2017. U-Pb Ages and Hf Isotopes in zircons from parautochthonous Mesozoic terranes in the Western margin of Pangea: Implications for the terrane configurations in the Northern Andes. The Journal of Geology, 125, 487-500. https://doi.org/10.1086/693014

Bustamante A., Bustamante, C., Cardona, A., Juliani, C., Pereira da Silva, S., 2021. Protoliths of the Jambaló blueschist and greenschist in the Central Colombian Andes and its tectonic implications with the Late Cretaceous Caribbean-South American interaction. Journal of South American Earth Sciences. 102977 https://doi.org/10.1016/j.jsames.2020.102977

Caballero, V., Parra, M., Mora, A., López, C., Rojas, L.E., Quintero, I., 2013, Factors controlling selective abandonment and reactivation in thick-skin orogens: A case study in the Magdalena Valley, Colombia, *in* Nemčok, M., Mora, A., and Cosgrove, J.W., eds., Thick-Skin-Dominated Orogens: From Initial Inversion to Full Accretion: Geological Society of London Special Publication 377, 343–367.

Cardona, A., Valencia, V., Garzón, A., Montes, C., Ojeda, G., Ruiz, J., Weber, M., 2010. Permian to Triassic I to S–type magmatic switch in the northeast Sierra Nevada de Santa Marta and adjacent regions, Colombian Caribbean: Tectonic setting and implications within Pangea paleogeography. Journal of South American Earth Sciences, 29, 772–783. https://doi.org/10.1016/j.jsames.2009.12.005

Castillo, P.R., 2012. Adakite petrogenesis. Lithos 134-135, 304–316. https://doi.org/10.1016/j.lithos.2011.09.013

Cawood, P. A. 2005. Terra Australis Orogen: Rodinia breakup and development of the Pacific and Iapetus margins of Gondwana during the Neoproterozoic and Paleozoic. Earth-Science Reviews, 69, 249–279.

Cawood, P. A. & Buchan, C. 2007. Linking accretionary orogenesis with supercontinent assembly. Earth-Science Reviews, 82, 217–256.

Cecil, M. R., Ferrer, M. A., Riggs, N. R., Marsaglia, K., Kylander-Clark, A., Ducea, M. N., Stone, P., 2019. Early arc development was recorded in Permian–Triassic plutons of the northern Mojave Desert region, California, USA. Bulletin, 131(5-6), 749-765.

Chapman, J.B., Ducea, M.N., DeCelles, P.G., Profeta, L., 2015. Tracking changes in crustal thickness during orogenic evolution with Sr/Y; an example from the North American Cordillera. Geology 43, 919–922. doi:10.1130/G36996.1

Chappell, B.W., 1999. Aluminium saturation in I- and S-type granites and the characterization of fractionated haplogranites. Lithos 46 (3), 535–551.

Charrier, R., Pinto, L. Rodríguez, M.P. 2007. Tectonostratigraphic evolution of the Andean Orogen in Chile. In: Moreno, T. & Gibbons, W. (editors), The geology of Chile. The Geological Society, p. 21–114. London. https://doi.org/10.1144/GOCH.3

Cochrane, R., Spikings, R., Gerdes, A., Ulianov, A., Mora, A., Villagómez, D., Putlitz, B., Chiaradia, M., 2014. Permo-Triassic anatexis, continental rifting, and the disassembly of western Pangaea. Lithos, 190, 383-402. https://doi.org/10.1016/j.lithos.2013.12.020

Coloma, F., Valin, X., Oliveros, V., Vásquez, P., Creixell, C., Salazar, E., Ducea, M. N., 2017. Geochemistry of Permian to Triassic igneous rocks from northern Chile (28º-30º15'S): Implications on the dynamics of the proto-Andean margin. Andean Geology, 44(2), 147-178.

Collins, W.J., 1998. Evaluation of petrogenetic models for Lachlan Fold Belt granitoids: Implications for crustal architecture and tectonic models, Australian Journal of Earth Sciences, 45:4, 483-500. DOI: 10.1080/08120099808728406

Collins, W. J., Richards, S. W., 2008. Geodynamic significance of S-type granites in circum-Pacific orogens. Geology, 36(7), 559-562. https://doi.org/10.1130/G24658A.1

Cortés, M., Colletta, B., Angelier, J., 2006. Structure and tectonics of the central segment of the Eastern Cordillera of Colombia. Journal of South American Earth Sciences, 21, 437–465. https://doi.org/10.1016/j.jsames.2006.07.004

Ducea, M. N., Saleeby, J. B., Bergantz, G., 2015. The architecture, chemistry, and evolution of continental magmatic arcs. Annual Review of Earth and Planetary Sciences, 43, 299-331. https://doi.org/10.1146/annurev-earth-060614-105049

Dasch, L.E., 1982. U–Pb Geochronology of the Sierra de Perijá. Ph.D. Thesis. Case Western Reserve University, 163.

DuFrane, S. A., Vervoort, J. D., Hart, G. L., 2007. Uncertainty of Hf isotope analysis in zircon using LAMC-ICPMS techniques: full disclosure. Geochim. Cosmochim. Acta 71, A241

Duque-Trujillo, J.F., Bustamante, C., Solari, L., Gómez-Mafla, Á., Toro-Villegas, G., Hoyos, S., 2019. Reviewing the Antioquia batholith and satellite bodies: a record of Late Cretaceous to Eocene syn-to post-collisional arc magmatism in the Central Cordillera of Colombia. Andean Geology, 46, 82-101. http://dx.doi.org/10.5027/andgeoV46n1-3120

Espejo, A., Etchart, H., Cordani, U., Kawashita, K., 1980. Geocronología de intrusívas ácidas en la Sierra de Perijá, Venezuela. Boletín Dirección, General de Minas y Geología XIV, 245–254.

Feo-Codoecido, G., Smith, F., Aboud, N., Di Giacomo, E., 1984. Basement Paleozoic rocks of the Venezuelan Llanos basin. Geological Society of America, Memoir 162, 175–187.

Frost, B.R., Frost, C. D., Hulsebosch, T. P., Swapp, S. M., 2000. Origin of the charnockites of the Louis lake Batholith, wind River Range, Wyoming. Journal of Petrology, 41(12), 1759-1776. https://doi.org/10.1093/petrology/41.12.1759

Frost, B.R., Barnes, C.G., Collins, W.J., Arculus, R.J., Ellis, D.J., Frost, C.D., 2001. A geochemical classification for granitic rocks. Journal of petrology, 42, 2033-2048. https://doi.org/10.1093/petrology/42.11.2033

Goodge, J. W., Vervoort, J. D., 2006. Origin of Mesoproterozoic A-type granites in Laurentia: Hf isotope evidence. Earth Planet. Sci. Lett. 243, 711–731.

Guillong, M., von Quadt, A., Sakata, S., Peytcheva, I., Bachmann, O., 2014. LA-ICP-MS Pb-U dating of young zircons from the Kos-Nisyros volcanic center, SE Aegean arc. Journal of Analytical Atomic Spectrometry, 29, 963. https://doi.org/10.1039/C4JA00009A

Grosse, P., Bellos, L. I., de los Hoyos, C.R., Larrovere, M. A., Rossi, J. N., Toselli, A. J., 2011. Across-arc variation of the Famatinian magmatic arc (NW Argentina) exemplified by I-, S-and transitional I/S-type Early Ordovician granitoids of the Sierra de Velasco. Journal of South American Earth Sciences, 32(1), 110-126. https://doi.org/10.1016/j.jsames.2011.03.014

He, Y., He, Z. H., Ge, W. C., Yang, H., Wang, Z. H., Dong, Y., Bi, J., Zhao, D., 2018. Petrogenesis and tectonic implications of Late Jurassic–Early Cretaceous granitic magmatism in the Xing'an Block, Northeast China: geochronological, geochemical, and Hf

isotopic evidence. Canadian Journal of Earth Sciences. 55(6): 571-588. https://doi.org/10.1139/cjes-2017-0226

Healy, B., Collins, W.J., Richards, S.W., 2004. A hybrid origin for Lachlan S-type granites: the Murrumbidgee Batholith example. Lithos 78, 197–216. https://doi.org/10.1016/j.lithos.2004.04.047

Hincapié-Gómez, S., Cardona, A., Jiménez, G., Monsalve, G., Ramírez-Hoyos, L., Bayona, G., 2018. Paleomagnetic and gravimetrical reconnaissance of Cretaceous volcanic rocks from the Western Colombian Andes: Paleogeographic connections with the Caribbean Plate. Studia Geophysica et Geodaetica, 62, 485-511. https://doi.org/10.1007/s11200-016-0678-y.

Horton, B.K., Saylor, J.E., Nie, J., Mora, A., Parra, M., Reyes-Harker, A., Stocki, D.F., 2010, Linking sedimentation in the Northern Andes to basement configuration, Mesozoic extension, and Cenozoic shortening: Evidence from detrital zircon U-Pb ages, Eastern Cordillera, Colombia: Geological Society of America Bulletin, 122 (9–10), 1423–1442, DOI: 10 .1130/B30118.1

Hoskin, P.W., Schaltegger, U., 2003. The composition of zircon and igneous and metamorphic petrogenesis. Reviews in mineralogy and geochemistry, 53, 27-62. https://doi.org/10.2113/0530027

Jaramillo, J.S., Cardona, A., León, S., Valencia, V., Vinasco, C., 2017. Geochemistry and geochronology from Cretaceous magmatic and sedimentary rocks at 6°35′ N, western flank of the Central cordillera (Colombian Andes): Magmatic record of arc growth and collision. Journal of South American Earth Sciences, 76, 460-481. https://doi.org/10.1016/j.jsames.2017.04.012

Janoušek, V., Farrow, C.M., Erban, V., 2006. Interpretation of whole-rock geochemical data in igneous geochemistry: introducing Geochemical Data Toolkit (GCDkit). Journal of Petrology, 47, 1255–1259.

Kay, S.M., Ramos, V.A., Mpodozis, C. Sruoga, P. 1989. Late Paleozoic to Jurassic silicic magmatism at the Gondwana margin: Analogy to the middle Proterozoic in North America? Geology, 17(4): 324–328. https://doi.org/10.1130/0091-7613(1989)017<0324:LPTJSM>2.3.CO;2

Kerr, A.C., Marriner, G.F., Tarney, J., Nivia, A., Saunders, A.D., Thirlwall, M.F., Sinton, C.W., 1997. Cretaceous basaltic terranes in western Colombia: elemental, chronological and Sr-Nd constraints on petrogenesis. Journal of Petrology, 38, 677–702. https://doi.org/10.1093/petroj/38.6.677

Leal-Mejía, H., Shaw, R.P., Melgarejo, J.C., 2019. Spatial-Temporal Migration of Granitoid Magmatism and the Phanerozoic Tectono-Magmatic Evolution of the Colombian Andes. In: Cediel, F. and Shaw, R.P. (Eds.), Geology and Tectonics of Northwestern South America. Frontiers in Earth Sciences. Springer. Part IV. Chapter 5. 253- 254. https://doi.org/10.1007/978-3-319-76132-9_5

Liew, T. C., Hofmann, A. W., 1988. Precambrian crustal components, plutonic associations, plate environment of the Hercynian Fold Belt of central Europe: Indications from a Nd and Sr isotopic study. Contributions to Mineralogy and Petrology, 98(2), 129–138. doi:10.1007/bf00402106

Mange, M.A., Maurer, H., 1992. Heavy Minerals in Colour. Springer, Part I, Chapter 3, 11-22. https://doi.org/10.1007/978-94-011-2308-2

Maya, M., and González, H., 1995, Unidades litodémicas en la Cordillera Central de Colombia: Boletín Geológico, Ingeominas, v. 35, no. 2–3, 43–57.

McDonough, W.F., and Sun, S.-S., 1995, The composition of the Earth: Chemical Geology, v. 120, p. 223–253, doi:10.1016/ 0009-2541(94)00140-4.

Middlemost, E., 1994. Naming materials in magma/igneous rock system. Earth-Science Reviews, 37, 215–224. https://doi.org/10.1016/0012-8252(94)90029-9

Miller, C. F., McDowell, S. M., Mapes, R. W., 2003. Hot and cold granites? Implications of zircon saturation temperatures and preservation of inheritance. Geology, 31(6), 529-532. https://doi.org/10.1130/0091-7613(2003)031<0529:HACGIO>2.0.CO;2

Mišković, A., Spikings, R.A., Chew, D.M., Košler, J., Ulianov, A. & Schaltegger, U. 2009. Tectonomagmatic evolution of western Amazonia: Geochemical characterization and zircon U–Pb geochronologic constraints from the Peruvian eastern cordilleran granitoids. Geological Society of America Bulletin, 121(9–10): 1298–1324. https://doi.org/10.1130/B26488.1

Mora, A., Gaona, T., Kley, J., Montoya, D., Parra, M., Quiroz, L., Reyes, G., Strecker, M., 2009. The Role of inherited extensional fault segmentation and linkage in contractional orogenesis: a reconstruction of Lower Cretaceous inverted rift basins in the Eastern Cordillera of Colombia. Basin Research, 21, 111-137. https://doi.org/10.1111/j.1365-2117.2008.00367.x.

Nance, R. D., Linnemann, U. 2008. The Rheic Ocean: origin, evolution, and significance. Gsa Today, 18(12), 4-12.

Nie, J., Horton, B.K., Mora, A., Saylor, J.E., Housh, T.B., Rubiano, J., Naranjo, J., 2010, Tracking exhumation of Andean ranges bounding the Middle Magdalena Valley Basin, Colombia: Geological Society of America Bulletin, 38, 451–454.

Oliveros, V., Vásquez, P., Creixell, C., Lucassen, F., Ducea, M. N., Ciocca, I., González, J., Espinoza, M., Salazar, E., Coloma, F., Kasemann, S. A., 2020. Lithospheric evolution of the Pre-and Early Andean convergent margin, Chile. Gondwana Research, 80, 202-227.

Ortega–Obregón, C., Solari, L., Gómez–Tuena, A., Elías–Herrera, M., Ortega–Gutiérrez, F., Macías–Romo, C., 2014. Permian – Carboniferous arc magmatism in southern Mexico: U–Pb dating, trace element and Hf isotopic evidence on zircons of earliest subduction beneath the western margin of Gondwana. International Journal of Earth Sciences, 103(5): 1287–1300. https://doi.org/10.1007/s00531-013-0933-1

Pankhurst, R.J., Rapela, C.W., Fanning, C.M., 2000. Age and origin of coeval TTG, I, and S-type granites in the Famatinian belt of NW Argentina. Transactions of the Royal Society of Edinburgh: Earth Sciences 91, 151-168. doi:10.1017/S0263593300007343

Patiño Douce, A.E., 1999. What do experiments tell us about the relative contributions of crust and mantle to the origin of granitic magmas? Geological Society, London, Special Publications 168 (1), 55–75. https://doi.org/10.1144/GSL.SP.1999.168.01.05

Paul, A. N., Spikings, R. A., Ulianov, A., Ovtcharova, M., 2018. High temperature (> 350° C) thermal histories of the long-lived (> 500 Ma) active margin of Ecuador and Colombia: Apatite, titanite, and rutile U-Pb thermochronology. Geochimica et Cosmochimica Acta, 228, 275-300. https://doi.org/10.1016/j.gca.2018.02.033

Pearce, J.A., Harris, N.B.W., Tindle, A.G., 1984. Trace element discrimination diagrams for the tectonic interpretation of granitic rocks. Journal of Petrology, 25, 956–983.

Piraquive, A., Kammer, A., Bernet, M., Cramer, T., von Quadt, A., Gómez, C., 2021. Neoproterozoic to Jurassic tectono-metamorphic events in the Sierra Nevada de Santa Marta Massif, Colombia: insights from zircon U-Pb geochronology and trace element geochemistry. International Geology Review, 1-33. https://doi.org/10.1080/00206814.2021.1961317

Profeta, L., Ducea, M.N., Chapman, J.B., Paterson, S.R., Henríquez-Gonzáles, S.M., Kirsch, M., Petrescu, L., DeCelles, P.G., 2015. Quantifying crustal thickness over time in magmatic arcs. Scientific Reports 5, 17786. DOI: 10.1038/srep17786

Restrepo, J.J., Ordóñez–Carmona, O., Armstrong, R., Pimentel, M.M., 2011. Triassic metamorphism in the northern part of the Tahamí Terrane of the Central

Cordillera of Colombia. Journal of South American Earth Sciences, 32, 497–507. https://doi.org/10.1016/j.jsames.2011.04.009

Riel, N., Jaillard, E., Martelat, J. E., Guillot, S., Braun, J., 2018. Permian-Triassic Tethyan realm reorganization: Implications for the outward Pangea margin. Journal of South American Earth Sciences, 81, 78-86.

Rodríguez, G., Arango, M. I., Zapata, G., Bermúdez, J. G., 2014. Petrografía y geoquímica del Neis de Nechí. Boletín de Geología, 36, 71-84.

Rodríguez, G., Zapata, G., Arango, M.I., Bermúdez, J.G., 2017. Caracterización petrográfica, geoquímica y geocronología de rocas granitoides Pérmicas al occidente de La Plata y Pacarní – Huila, Valle Superior del Magdalena – Colombia. Boletín de Geología, 39, 41-68.

Rodríguez–García, G., Correa–Martínez, A.M., Zapata–Villada, J.P., Obando–Erazo, G., 2019. Fragments of a Permian arc on the western margin of the Neoproterozoic basement of Colombia. In: Gómez, J. and Mateus–Zabala, D. (Eds.), The Geology of Colombia, Volume 1 Proterozoic – Paleozoic. Servicio Geológico Colombiano, Publicaciones Geológicas Especiales 35, 34 p. Bogotá. https://doi.org/10.32685/pub.esp.35.2019.10

Rubatto, D., 2002. Zircon trace element geochemistry: partitioning with garnet and linking U-Pb ages and metamorphism. Chemical Geology, 184, 123–138. https://doi.org/10.1016/S0009-2541(01)00355-2

Sarmiento-Rojas, L.F., 2019. Cretaceous Stratigraphy and Paleo-Facies Maps of Northwestern South America. In: Cediel F. and Shaw R.P. (Eds.), Geology and Tectonics of Northwestern South America. Frontiers in Earth Sciences. Springer, Part V, Chapter 10, 673-748. https://doi.org/10.1007/978-3-319-76132-9_10

Saylor, J.E., Horton, B., Nie, J., Corredor, J., Mora, A., 2011, Evaluating foreland basin partitioning in the Northern Andes using Cenozoic fill of the Floresta Basin, Eastern Cordillera, Colombia: Basin Research, 23, 377–402, DOI: 10 .1111 /j .1365 - 2117.2010.00493.x

Sheppard, S., Occhipinti, S.A., Tyler, I.M., 2003. The relationship between tectonism and composition of granitoid magmas, Yarlarweelor Gneiss Complex, Western Australia. Lithos 66, 133–154. https://doi.org/10.1016/S0024-4937(02)00216-5

Silva, A., Mora, A., Caballero, V., Rodríguez, G., Ruiz, G., Moreno, N., Parra, M., Ramírez-Arias, J.C., Ibáñez, M., Quintero, I., 2013, Tectonic controls on sedimentation in an intermontane hinterland basin adjacent to inversion structures: The Nuevo Mundo syncline, Middle Magdalena Valley, Colombia, *in* Nemčok, M., Mora, A., and Cosgrove, J.W., eds., Thick-Skin-Dominated Orogens: From Initial Inversion to Full Accretion: Geological Society of London Special Publication 377, 369–409.

Spikings, R., Cochrane, R., Villagómez, D., van der Lelij, R., Vallejo, C., Winkler, W., Beate, B. 2015. The geological history of northwestern South America: From Pangaea to the early collision of the Caribbean Large Igneous Province (290–75 Ma). Gondwana Research, 27(1): 95–139. https://doi.org/10.1016/j.gr.2014.06.004

Spikings, R., Reitsma, M.J., Boekhout, F., Mišković, A., Ulianov, A., Chiaradia, M., Gerdes, A., Schaltegger, U. 2016. Characterization of Triassic rifting in Peru and implications for the early disassembly of western Pangaea. Gondwana Research, 35: 124–143. https://doi.org/10.1016/j.gr.2016.02.008

Spikings, R. Paul, A. 2019. The Permian – Triassic history of magmatic rocks of the northern Andes (Colombia and Ecuador): Supercontinent assembly and disassembly. In: Gómez, J. & Pinilla–Pachon, A.O. (editors), The Geology of Colombia, Volume 2 Mesozoic. Servicio Geológico Colombiano, Publicaciones Geológicas Especiales 36, p. 1–43. Bogotá. https://doi.org/10.32685/pub.esp.36.2019.01

Sun, S.S., McDonough, W.F., 1989. Chemical and isotopic systematics of oceanic basalts: implications for mantle composition and processes. In: Saunders, A.D., and Norry, M.J. (Eds.), Magmatism in oceanic basins. Geological Society of London, Special Publications, 42, 313-345.

Sylvester, P.J., 1998. Post-collisional strongly peraluminous granites. Lithos, 45, 29–44. https://doi.org/10.1016/S0024-4937(98)00024-3

van der Lelij, R., Spikings, R., Ulianov, A., Chiaradia, M. Mora, A. 2016. Palaeozoic to Early Jurassic history of the northwestern corner of Gondwana and implications for the evolution of the Iapetus, Rheic, and Pacific Oceans. Gondwana Research, 31: 271–294. https://doi.org/10.1016/j.gr.2015.01.011

van der Lelij, R., Spikings, R., Gerdes, A., Chiaradia, M., Vennemann, T., Mora, A. 2019. Multi-proxy isotopic tracing of magmatic sources and crustal recycling in the Palaeozoic to Early Jurassic active margin of North-Western Gondwana. Gondwana Research, 66, 227-245.

Vásquez, M., Altenberger, U., Romer, R.L., Sudo, M., Moreno-Murillo, J.M., 2010. Magmatic evolution of the Andean Eastern Cordillera of Colombia during the Cretaceous: Influence of previous tectonic processes. Journal of South American Earth Sciences, 2, 171-186. https://doi.org/10.1016/j.jsames.2009.02.003

Vermeesch, P., 2018. IsoplotR: a free and open toolbox for geochronology. Geoscience Frontiers, 9, 1479-1493. https://doi.org/10.1016/j.gsf.2018.04.001.

Vervoort, J. D., Patchett, P. J., 1996. The behavior of hafnium and neodymium isotope derived granites. Geochim. Cosmochim. Acta 60, 3717–3733.

Vervoort, J. D., Patchett, P. J., Soderlund, U., Baker, M., 2004. Isotopic composition of Yb and the determination of Lu concentrations and Lu/Hf ratios by isotope dilution using MC-ICPMS. Geochem. Geophys. Geosyst. 5, 15.

Vervoort, J. D., Kemp, A. I. S., Fisher, C., Bauer, A., 2015. The rock record has it about right—no significant continental crust formation prior to 3.8 Ga. Am. Geophys. Union Fall Meeting 2015, abstract V43D-05.

Vesga, C. J., Barrero, D., 1978. Edades K/Ar en rocas ígneas y metamórficas de la Cordillera Central de Colombia y su implicación geológica. Bogotá, II Congreso Colombiano de Geología: Resúmenes.

Vilas, J.F., Valencio, D.A., 1978. Palaeomagnetism and K–Ar age of the Upper Ordovician Alcaparrosa Formation, Argentina. Geophysical Journal International, 55(1): 143–154. https://doi.org/10.1111/j.1365-246X.1978.tb04753.x

Villagómez, D., Spikings, R., Magna, T., Kammer, A., Winkler, W., Beltrán, A., 2011. Geochronology, geochemistry, and tectonic evolution of Western and Central Cordilleras of Colombia. Lithos, 125, 875–896. https://doi.org/10.1016/j.lithos.2011.05.003

Vinasco, C., Cordani, U., González, H., Weber, M., Peláez, C., 2006. Geochronological, isotopic, and geochemical data from Permo-Triassic granitic gneisses and granitoids of the Colombian Central Andes. Journal of South American Earth Sciences, 21, 355-371. https://doi.org/10.1016/j.jsames.2006.07.007

Vinasco, C., 2019. The Romeral Shear Zone. In: Cediel, F., Shaw, R.P. (eds) Geology and Tectonics of Northwestern South America. Frontiers in Earth Sciences. Springer, Cham. https://doi.org/10.1007/978-3-319-76132-9_12

Viscarret, P., Wright, J., Urbani, F. 2009. New U-Pb zircon ages of El Baúl Massif, Cojedes State, Venezuela. Revista Tecnica de la Facultad de Ingenieria Universidad del Zulia, 32(3), 210-221.

von Quadt, A., Wotzlaw, J.F., Buret, Y., Large, S.J.E., Peytcheva, I., Trinquir, A., 2016. High-precision zircon U/Pb geochronology by ID-TIMS using new 1013 ohm resistors. Journal of Analytical Atomic Spectrometry, 31, 658. https://doi.org/10.1039/C5JA00457H.

Watson, E.B., Harrison, T.M., 1983. Zircon saturation revisited: temperature and composition effects in various crustal magma types. Earth and Planetary Science Letters, 64 (2), 295–304. https://doi.org/10.1016/0012-821X(83)90211-X

Watson, E.B., Wark, D.A., Thomas, J.B., 2006. Crystallization thermometers for zircon and rutile. Contrib. Mineral. Petrol. 151 (4), 413–433. https://doi.org/10.1007/s00410-006-0068-5

Weber, B., Iriondo, A., Premo, W.R., Hecht, L., Schaaf, P., 2007. New insights into the history and origin of the southern Maya Block, SE México: U–Pb SHRIMP zircon geochronology from metamorphic rocks of the Chiapas Massif. International Journal of Earth Sciences, 96(2): 253–269. https://doi.org/10.1007/s00531-006-0093-7

Whalen, J.B., Currie, K.L., and Chappell, B.W. 1987. A-type granites: geochemical characteristics, discrimination, and petrogenesis. Contributions to Mineralogy and Petrology, 95: 407–419. doi:10.1007/BF00402202.

Xie, F., Wu, J., Sun, Y., Wang, L., Wu, J., Jia, W., 2021. Permian to Triassic tectonic evolution of the Alxa Tectonic Belt, NW China: Constraints from petrogenesis and geochronology of felsic intrusions. Lithos, 384, 105980. https://doi.org/10.1016/j.lithos.2021.105980

Zapata, S., Cardona, A., Jaramillo, J.S., Patiño, A., Valencia, V., León, S., Mejía, D., Pardo-Trujillo, A., Castañeda, J.P., 2019. Cretaceous extensional and compressional tectonics in the Northwestern Andes, prior to the collision with the Caribbean oceanic plateau. Gondwana Research, 66, 207-226. https://doi.org/10.1016/j.gr.2018.10.008

Appendix

Table 1. Zircon U-Pb geochronology results.

Spot no.	Th (ppm)	U (ppm)	Th/U	207Pb/235U	2σ error	206Pb/238U	2σ error	Corr. Coef	207Pb/206Pb	2σ error	206Pb/238U Age (Ma)	2σ error	207Pb/206Pb Age (Ma)	2σ error	Preferred age	2σ error
CLM4A																
CLM-4A_1	54.3	171.3	0.3	0.3028	0.0034	0.0425	0.0004	0.3490	0.0517	0.0006	268.1	2.2	266	27	268.1	2.2
CLM-4A_2	48.0	160.7	0.3	0.3044	0.0039	0.0423	0.0004	0.5094	0.0523	0.0006	266.8	2.4	290	26	266.8	2.4
CLM-4A_3	30.1	56.8	0.5	0.3008	0.0050	0.0423	0.0005	0.3742	0.0516	0.0009	266.9	2.9	257	38	266.9	2.9
CLM-4A_4	47.8	154.4	0.3	0.3026	0.0036	0.0419	0.0003	0.3691	0.0524	0.0006	264.8	2.1	292	27	264.8	2.1
CLM-4A_5	40.0	123.0	0.3	0.3130	0.0048	0.0434	0.0005	0.2173	0.0523	0.0008	274.0	2.9	298	38	274.0	2.9
CLM-4A_6	24.8	71.6	0.3	0.3030	0.0058	0.0420	0.0004	0.2827	0.0524	0.0010	264.9	2.6	286	43	264.9	2.6
CLM-4A_8	78.7	237.0	0.3	0.3018	0.0034	0.0423	0.0004	0.4204	0.0518	0.0006	266.9	2.3	269	25	266.9	2.3
CLM-4A_9	10.1	45.8	0.2	0.2940	0.0052	0.0422	0.0005	0.4528	0.0506	0.0008	266.4	2.9	208	37	266.4	2.9
CLM-4A_10	47.9	144.1	0.3	0.3023	0.0046	0.0421	0.0004	0.3052	0.0521	0.0008	265.6	2.2	281	34	265.6	2.2
CLM-4A_11	122.7	209.0	0.6	0.3087	0.0062	0.0424	0.0005	0.3754	0.0528	0.0009	267.8	3.1	310	37	267.8	3.1
CLM-4A_12	78.1	125.3	0.6	0.3045	0.0054	0.0419	0.0004	0.4016	0.0527	0.0009	264.6	2.6	308	37	264.6	2.6
CLM-4A_13	152.4	237.4	0.6	0.3025	0.0036	0.0422	0.0003	0.4002	0.0520	0.0006	266.4	2.0	278	26	266.4	2.0
CLM-4A_14	37.4	134.0	0.3	0.3467	0.0080	0.0456	0.0009	0.4050	0.0552	0.0013	287.3	5.3	403	54	287.3	5.3
CLM-4A_15	64.8	176.1	0.4	0.3005	0.0039	0.0421	0.0004	0.4322	0.0518	0.0006	266.0	2.3	267	27	266.0	2.3
CLM-4A_16	85.2	164.9	0.5	0.2983	0.0052	0.0417	0.0005	0.2908	0.0519	0.0009	263.6	2.8	275	38	263.6	2.8
CLM-4A_17	81.9	229.4	0.4	0.3013	0.0042	0.0422	0.0005	0.7303	0.0519	0.0005	266.2	3.1	277	23	266.2	3.1
CLM-4A_18	98.1	207.9	0.5	0.3008	0.0037	0.0418	0.0004	0.5696	0.0522	0.0005	264.2	2.2	289	24	264.2	2.2
CLM-4A_19	58.2	204.6	0.3	0.3023	0.0036	0.0420	0.0004	0.3695	0.0522	0.0006	265.4	2.3	290	27	265.4	2.3
CLM-4A_20	130.7	217.1	0.6	0.3143	0.0054	0.0430	0.0004	0.5043	0.0531	0.0008	271.2	2.7	330	34	271.2	2.7
CLM-4A_21	121.5	173.5	0.7	0.3042	0.0051	0.0420	0.0006	0.5888	0.0526	0.0008	265.1	3.6	300	33	265.1	3.6
CLM-4A_22	99.5	175.4	0.6	0.3043	0.0054	0.0420	0.0004	0.2627	0.0526	0.0010	264.9	2.8	306	42	264.9	2.8
CLM-4A_23	56.1	186.5	0.3	0.3029	0.0038	0.0420	0.0004	0.3604	0.0523	0.0007	265.2	2.4	291	30	265.2	2.4
CLM-4A_24	139.9	246.0	0.6	0.3122	0.0061	0.0440	0.0008	0.4205	0.0515	0.0010	277.4	4.8	264	46	277.4	4.8

CLM-4A_25	43.8	98.7	0.4	0.3033	0.0047	0.0421	0.0004	0.2542	0.0523	0.0008	265.8	2.3	287	36	265.8	2.3
CLM-4A_26	68.5	127.5	0.5	0.3014	0.0043	0.0422	0.0003	0.4102	0.0519	0.0007	266.4	2.1	269	31	266.4	2.1
CLM-4A_27	52.4	176.9	0.3	0.3043	0.0046	0.0422	0.0004	0.4751	0.0524	0.0007	266.2	2.5	293	31	266.2	2.5
CLM-4A_28	57.8	176.2	0.3	0.3024	0.0035	0.0423	0.0003	0.3652	0.0518	0.0006	267.2	2.1	272	24	267.2	2.1
CLM-4A_29	72.8	124.7	0.6	0.3036	0.0043	0.0425	0.0004	0.5007	0.0518	0.0006	268.6	2.4	269	27	268.6	2.4
CLM-4A_30	106.1	139.3	0.8	0.3033	0.0044	0.0425	0.0004	0.5514	0.0518	0.0006	268.2	2.6	269	27	268.2	2.6
CLM-4A_31	58.5	196.6	0.3	0.3032	0.0040	0.0422	0.0004	0.4244	0.0521	0.0006	266.5	2.2	284	28	266.5	2.2
CLM-4A_32	9.8	35.4	0.3	0.3140	0.0062	0.0433	0.0005	0.2883	0.0526	0.0011	273.4	3.3	289	45	273.4	3.3
CLM-4A_33	58.5	150.7	0.4	0.3054	0.0038	0.0421	0.0004	0.2682	0.0527	0.0007	265.6	2.4	305	31	265.6	2.4
CLM-4A_34	38.6	156.2	0.2	0.3022	0.0045	0.0419	0.0005	0.2754	0.0523	0.0008	264.7	3.1	290	35	264.7	3.1
CLM-4A_35	60.1	134.2	0.4	0.3045	0.0054	0.0424	0.0007	0.5100	0.0521	0.0010	267.8	4.6	277	43	267.8	4.6
CLM-4A_36	51.0	190.8	0.3	0.3107	0.0041	0.0432	0.0005	0.4672	0.0522	0.0007	272.5	3.2	284	32	272.5	3.2
CLM-4A_37	95.4	168.3	0.6	0.3146	0.0040	0.0435	0.0005	0.4452	0.0524	0.0007	274.7	2.8	296	28	274.7	2.8
CLM-4A_38	57.0	172.0	0.3	0.3158	0.0055	0.0440	0.0006	0.3521	0.0520	0.0009	277.8	3.9	284	42	277.8	3.9
CLM-4A_39	25.2	95.6	0.3	0.3197	0.0089	0.0441	0.0010	0.5119	0.0526	0.0014	278.2	6.1	291	61	278.2	6.1
CLM-4A_40	100.3	135.8	0.7	0.3090	0.0079	0.0427	0.0006	0.1574	0.0525	0.0014	269.6	3.9	300	63	269.6	3.9
								CLM5								
CLM-5_1	172.0	248.2	0.7	0.3004	0.0044	0.0417	0.0004	0.4579	0.0523	0.0007	263.2	2.3	291.0	30	263.2	2.3
CLM-5_2	206.2	471	0.4	0.2992	0.0033	0.0420	0.0003	0.4334	0.0517	0.0006	265.2	2.1	264.0	24	265.2	2.1
CLM-5_3	121.5	173.5	0.7	0.3042	0.0051	0.0420	0.0006	0.5888	0.0526	0.0008	265.1	3.6	300.0	33	265.1	3.6
CLM-5_4	132.5	187.1	0.7	0.2938	0.0041	0.0417	0.0003	0.3292	0.0512	0.0007	263.1	2.1	242.0	32	263.1	2.1
CLM-5_5	83.9	155.4	0.5	0.3044	0.0051	0.0419	0.0003	0.2310	0.0527	0.0009	264.6	2.1	302.0	38	264.6	2.1
CLM-5_7	234.4	297.7	0.8	0.3026	0.0039	0.0423	0.0003	0.2351	0.0519	0.0007	267.0	2.1	274.0	30	267.0	2.1
CLM-5_8	104.2	193	0.5	0.3087	0.0053	0.0417	0.0004	0.3334	0.0537	0.0010	263.6	2.5	345.0	40	263.6	2.5
CLM-5_9	140.3	212.1	0.7	0.3002	0.0048	0.0422	0.0004	0.2927	0.0516	0.0008	266.3	2.4	256.0	35	266.3	2.4
CLM-5_10	210.7	343	0.6	0.3030	0.0038	0.0422	0.0003	0.3524	0.0521	0.0007	266.5	2.1	280.0	29	266.5	2.1
CLM-5_11	164.7	264.9	0.6	0.3020	0.0039	0.0421	0.0004	0.4406	0.0521	0.0006	265.8	2.4	281.0	28	265.8	2.4
CLM-5_12	226.1	352	0.6	0.3008	0.0037	0.0420	0.0003	0.2461	0.0520	0.0007	265.1	2.0	275.0	29	265.1	2.0
CLM-5_13	259.8	297.7	0.9	0.2958	0.0037	0.0417	0.0004	0.3241	0.0515	0.0007	263.2	2.3	256.0	29	263.2	2.3

CLM-5_14	147.2	207.4	0.7	0.3055	0.0060	0.0423	0.0004	0.2161	0.0524	0.0011	267.1	2.7	290.0	45	267.1	2.7
CLM-5_15	202.6	344	0.6	0.3061	0.0054	0.0426	0.0006	0.4955	0.0522	0.0009	268.8	3.6	282.0	38	268.8	3.6
CLM-5_17	290.7	457	0.6	0.3000	0.0036	0.0419	0.0004	0.3331	0.0520	0.0006	264.5	2.3	278.0	28	264.5	2.3
CLM-5_18	150.9	366	0.4	0.2999	0.0038	0.0421	0.0004	0.3011	0.0517	0.0007	265.8	2.3	264.0	30	265.8	2.3
CLM-5_19	154.9	271.8	0.6	0.3032	0.0044	0.0422	0.0004	0.4251	0.0522	0.0007	266.3	2.7	283.0	31	266.3	2.7
CLM-5_20	169.3	239.6	0.7	0.3241	0.0054	0.0421	0.0004	0.1881	0.0559	0.0010	265.6	2.6	433.0	40	265.6	2.6
CLM-5_21	269.8	368.3	0.7	0.3016	0.0035	0.0421	0.0004	0.4868	0.0520	0.0006	266.0	2.4	275.0	25	266.0	2.4
CLM-5_22	236.1	330.3	0.7	0.3008	0.0043	0.0420	0.0004	0.3432	0.0520	0.0008	265.1	2.3	275.0	33	265.1	2.3
CLM-5_23	146.6	249.4	0.6	0.3021	0.0037	0.0418	0.0003	0.3826	0.0524	0.0006	264.1	2.1	298.0	29	264.1	2.1
CLM-5_24	115.7	271	0.4	0.3007	0.0039	0.0421	0.0004	0.3894	0.0518	0.0006	266.1	2.4	273.0	28	266.1	2.4
CLM-5_25	152.9	205.5	0.7	0.3017	0.0049	0.0419	0.0005	0.4630	0.0522	0.0009	264.8	3.3	282.0	37	264.8	3.3
CLM-5_26	104.7	164.2	0.6	0.3066	0.0065	0.0419	0.0004	0.3870	0.0531	0.0010	264.5	2.6	330.0	44	264.5	2.6
CLM-5_27	106.7	171.7	0.6	0.3047	0.0047	0.0419	0.0004	0.2801	0.0527	0.0008	264.9	2.2	304.0	35	264.9	2.2
CLM-5_28	97.6	176.6	0.6	0.3028	0.0047	0.0419	0.0004	0.5341	0.0524	0.0008	264.5	2.6	293.0	33	264.5	2.6
CLM-5_29	163.6	244.7	0.7	0.3031	0.0041	0.0423	0.0004	0.5501	0.0520	0.0006	267.3	2.6	273.0	27	267.3	2.6
CLM-5_30	93.2	145.5	0.6	0.2998	0.0039	0.0421	0.0004	0.3055	0.0517	0.0007	265.7	2.3	262.0	30	265.7	2.3
CLM-5_31	89.6	241.6	0.4	0.3036	0.0044	0.0420	0.0005	0.4609	0.0524	0.0007	265.4	3.0	296.0	32	265.4	3.0
CLM-5_32	175.0	302.4	0.6	0.3010	0.0047	0.0422	0.0006	0.5814	0.0517	0.0008	266.5	3.9	265.0	35	266.5	3.9
CLM-5_33	63.1	146.3	0.4	0.3025	0.0039	0.0418	0.0003	0.2807	0.0525	0.0007	263.8	2.1	299.0	30	263.8	2.1
CLM-5_34	52.1	83.6	0.6	0.3009	0.0049	0.0418	0.0004	0.3483	0.0522	0.0009	264.1	2.7	280.0	37	264.1	2.7
CLM-5_35	83.2	219	0.4	0.2993	0.0036	0.0421	0.0004	0.3350	0.0516	0.0007	265.6	2.3	258.0	29	265.6	2.3
CLM-5_36	47.2	76.2	0.6	0.3045	0.0057	0.0420	0.0004	0.2229	0.0527	0.0010	265.0	2.6	307.0	42	265.0	2.6
CLM-5_37	105.8	133.9	0.8	0.2991	0.0042	0.0421	0.0004	0.2297	0.0516	0.0007	265.6	2.3	261.0	33	265.6	2.3
CLM-5_38	137.3	212.1	0.6	0.3021	0.0038	0.0422	0.0004	0.3192	0.0519	0.0007	266.7	2.6	280.0	30	266.7	2.6
CLM-5_39	50.2	116.1	0.4	0.3004	0.0041	0.0421	0.0004	0.4065	0.0517	0.0007	266.0	2.4	264.0	30	266.0	2.4
CLM-5_40	84.4	109.3	0.8	0.3056	0.0064	0.0411	0.0004	0.1347	0.0539	0.0012	259.9	2.7	354.0	49	259.9	2.7
CLM-5_41	58.2	158.1	0.4	0.3036	0.0051	0.0421	0.0006	0.4475	0.0523	0.0009	265.9	3.6	288.0	40	265.9	3.6
CLM-5_42	56.1	129.6	0.4	0.3015	0.0039	0.0424	0.0004	0.4547	0.0516	0.0006	267.4	2.3	259.0	28	267.4	2.3
CLM-5_43	124.8	300	0.4	0.2987	0.0029	0.0421	0.0003	0.3712	0.0515	0.0005	265.7	2.0	257.0	23	265.7	2.0

CLM-5_44	65.8	108.7	0.6	0.3005	0.0035	0.0420	0.0004	0.4512	0.0519	0.0006	265.2	2.4	274.0	25	265.2	2.4
CLM-5_45	36.1	71.9	0.5	0.3023	0.0057	0.0415	0.0004	0.2168	0.0528	0.0010	262.4	2.6	306.0	44	262.4	2.6
								CLM6A								
CLM-6A_1	80.4	146.2	0.6	0.3111	0.0045	0.0435	0.0005	0.3972	0.0519	0.0008	274.7	2.9	270.0	33.0	274.7	2.9
CLM-6A_2	314.3	436.6	0.7	0.3094	0.0050	0.0432	0.0006	0.5282	0.0520	0.0008	272.3	3.6	283.0	34.0	272.3	3.6
CLM-6A_3	132.2	229.9	0.6	0.3047	0.0044	0.0428	0.0006	0.4868	0.0517	0.0007	270.0	3.6	261.0	32.0	270.0	3.6
CLM-6A_4	103.5	154.7	0.7	0.3089	0.0047	0.0429	0.0005	0.5216	0.0522	0.0007	270.9	2.9	284.0	31.0	270.9	2.9
CLM-6A_5	22.8	133.9	0.2	0.9040	0.0170	0.0966	0.0013	0.6192	0.0679	0.0010	594.2	7.8	859.0	29.0	594.2	7.8
CLM-6A_6	77.0	117.2	0.7	0.3130	0.0059	0.0437	0.0005	0.3689	0.0520	0.0010	275.6	3.0	271.0	45.0	275.6	3.0
CLM-6A_7	48.2	80.8	0.6	0.3084	0.0055	0.0432	0.0004	0.2881	0.0518	0.0009	272.9	2.6	263.0	39.0	272.9	2.6
CLM-6A_8	81.5	168.5	0.5	0.3262	0.0110	0.0452	0.0015	0.4667	0.0524	0.0022	284.8	9.4	280.0	89.0	284.8	9.4
CLM-6A_9	47.6	132.2	0.4	0.3085	0.0057	0.0428	0.0008	0.4701	0.0523	0.0011	270.2	4.7	280.0	45.0	270.2	4.7
CLM-6A_10	62.4	118.6	0.5	0.3083	0.0060	0.0431	0.0006	0.4483	0.0519	0.0009	272.3	3.6	270.0	41.0	272.3	3.6
CLM-6A_11	67.4	153	0.4	0.3449	0.0095	0.0431	0.0004	0.3639	0.0581	0.0015	271.9	2.8	499.0	49.0	271.9	2.8
CLM-6A_12	60.8	113.6	0.5	0.3248	0.0047	0.0452	0.0004	0.3164	0.0522	0.0008	284.9	2.4	282.0	33.0	284.9	2.4
CLM-6A_13	193.8	177.7	1.1	0.3085	0.0046	0.0429	0.0006	0.3327	0.0521	0.0009	271.1	3.5	283.0	39.0	271.1	3.5
CLM-6A_14	60.2	142.6	0.4	0.3074	0.0057	0.0429	0.0008	0.4852	0.0520	0.0010	270.7	5.0	269.0	44.0	270.7	5.0
CLM-6A_15	120.4	119.2	1.0	0.3073	0.0057	0.0426	0.0005	0.2957	0.0523	0.0010	269.2	2.8	285.0	42.0	269.2	2.8
CLM-6A_16	80.9	119.6	0.7	0.3068	0.0042	0.0429	0.0004	0.4659	0.0519	0.0007	271.0	2.6	274.0	30.0	271.0	2.6
CLM-6A_17	54.7	112.1	0.5	0.3072	0.0050	0.0430	0.0005	0.4729	0.0519	0.0008	271.2	3.1	271.0	34.0	271.2	3.1
CLM-6A_18	37.2	103	0.4	0.3134	0.0072	0.0434	0.0008	0.2885	0.0524	0.0012	273.8	4.8	288.0	51.0	273.8	4.8
CLM-6A_19	141.3	163.3	0.9	0.3098	0.0052	0.0429	0.0006	0.4046	0.0524	0.0008	270.6	3.7	296.0	36.0	270.6	3.7
CLM-6A_20	75.6	128.9	0.6	0.3064	0.0045	0.0432	0.0005	0.2598	0.0514	0.0008	272.8	3.1	251.0	37.0	272.8	3.1
CLM-6A_21	79.4	120.2	0.7	0.3077	0.0049	0.0426	0.0004	0.4191	0.0524	0.0007	268.9	2.4	298.0	32.0	268.9	2.4
CLM-6A_22	50.6	127.8	0.4	0.3112	0.0055	0.0431	0.0005	0.5673	0.0523	0.0008	272.3	3.1	286.0	33.0	272.3	3.1
CLM-6A_23	117.4	212	0.6	0.3106	0.0039	0.0435	0.0004	0.4815	0.0518	0.0006	274.5	2.7	268.0	28.0	274.5	2.7
CLM-6A_24	44.8	63.9	0.7	0.3127	0.0050	0.0435	0.0005	0.1964	0.0521	0.0010	274.7	3.3	279.0	40.0	274.7	3.3
CLM-6A_25	86.0	125.7	0.7	0.3078	0.0042	0.0426	0.0004	0.4213	0.0524	0.0007	269.1	2.7	291.0	30.0	269.1	2.7
CLM-6A_26	56.3	118.7	0.5	0.3076	0.0060	0.0428	0.0007	0.6124	0.0522	0.0010	270.0	4.5	287.0	41.0	270.0	4.5

CLM-6A_27	110.0	165.9	0.7	0.3111	0.0036	0.0434	0.0005	0.3297	0.0520	0.0006	273.9	3.0	277.0	27.0	273.9	3.0
CLM-6A_28	60.4	104	0.6	0.3103	0.0057	0.0437	0.0007	0.3933	0.0516	0.0010	275.5	4.3	252.0	42.0	275.5	4.3
CLM-6A_29	99.2	155	0.6	0.3130	0.0045	0.0435	0.0005	0.4933	0.0522	0.0008	274.5	3.1	285.0	34.0	274.5	3.1
CLM-6A_30	102.6	147.8	0.7	0.3108	0.0049	0.0433	0.0005	0.5668	0.0520	0.0007	273.5	2.9	276.0	30.0	273.5	2.9
CLM-6A_31	53.3	127.7	0.4	0.3080	0.0090	0.0433	0.0011	0.4337	0.0516	0.0015	273.3	6.9	247.0	65.0	273.3	6.9
CLM-6A_32	79.7	135.2	0.6	0.3084	0.0048	0.0436	0.0006	0.5140	0.0514	0.0008	274.9	3.9	245.0	34.0	274.9	3.9
CLM-6A_33	62.3	113.1	0.6	0.3094	0.0046	0.0434	0.0004	0.3590	0.0517	0.0008	274.1	2.8	258.0	34.0	274.1	2.8
CLM-6A_36	151.3	258	0.6	0.3200	0.0088	0.0434	0.0008	0.5607	0.0535	0.0011	273.9	5.1	343.0	48.0	273.9	5.1
CLM-6A_37	127.9	285.1	0.4	0.3078	0.0042	0.0431	0.0004	0.4808	0.0519	0.0006	271.8	2.5	278.0	28.0	271.8	2.5
CLM-6A_38	107.1	157.7	0.7	0.3110	0.0045	0.0433	0.0004	0.2854	0.0521	0.0008	273.2	2.4	281.0	33.0	273.2	2.4
CLM-6A_39	182.8	302	0.6	0.3156	0.0059	0.0435	0.0007	0.4248	0.0527	0.0010	274.3	4.1	301.0	42.0	274.3	4.1
CLM-6A_40	383.2	463.7	0.8	0.3097	0.0044	0.0433	0.0005	0.6150	0.0519	0.0006	273.1	2.9	280.0	25.0	273.1	2.9
CLM-6A_41	133.4	192.7	0.7	0.3136	0.0052	0.0434	0.0004	0.4230	0.0525	0.0009	273.7	2.8	294.0	37.0	273.7	2.8
								CLM6B								
CLM-6B_1	180.6	315.2	0.6	0.3087	0.0052	0.0431	0.0005	0.2970	0.0519	0.0009	272.3	3.1	272.0	40.0	272.3	3.1
CLM-6B_2	144.0	214	0.7	0.3173	0.0065	0.0444	0.0008	0.4853	0.0519	0.0009	279.9	4.9	276.0	43.0	279.9	4.9
CLM-6B_3	40.5	68.5	0.6	0.3093	0.0043	0.0431	0.0004	0.1447	0.0521	0.0008	271.8	2.4	278.0	35.0	271.8	2.4
CLM-6B_4	59.2	112.4	0.5	0.3108	0.0050	0.0427	0.0005	0.3934	0.0528	0.0008	269.5	3.1	310.0	35.0	269.5	3.1
CLM-6B_6	32.5	131.8	0.2	0.3149	0.0060	0.0436	0.0007	0.4916	0.0524	0.0009	274.9	4.4	293.0	39.0	274.9	4.4
CLM-6B_7	72.8	124.7	0.6	0.3036	0.0043	0.0425	0.0004	0.5007	0.0518	0.0006	268.6	2.4	269.0	27.0	268.6	2.4
CLM-6B_8	82.9	230.2	0.4	0.3126	0.0043	0.0432	0.0006	0.6949	0.0525	0.0006	272.9	3.5	296.0	26.0	272.9	3.5
CLM-6B_9	43.6	89.7	0.5	0.3109	0.0049	0.0432	0.0005	0.3927	0.0522	0.0008	272.6	3.3	283.0	35.0	272.6	3.3
CLM-6B_10	63.2	120.3	0.5	0.3135	0.0073	0.0437	0.0007	0.3351	0.0520	0.0012	276.0	4.2	274.0	51.0	276.0	4.2
CLM-6B_12	21.6	49.7	0.4	0.3104	0.0051	0.0434	0.0004	0.2281	0.0519	0.0009	273.7	2.3	269.0	40.0	273.7	2.3
CLM-6B_13	45.9	76.1	0.6	0.3125	0.0038	0.0434	0.0004	0.2856	0.0523	0.0007	273.7	2.4	293.0	31.0	273.7	2.4
CLM-6B_15	23.4	56.8	0.4	0.3068	0.0052	0.0430	0.0005	0.3147	0.0518	0.0009	271.2	2.8	264.0	38.0	271.2	2.8
CLM-6B_16	64.0	97.2	0.7	0.3101	0.0054	0.0431	0.0004	0.3700	0.0522	0.0009	272.0	2.7	285.0	37.0	272.0	2.7
CLM-6B_17	91.7	155.3	0.6	0.3139	0.0038	0.0436	0.0004	0.4937	0.0522	0.0006	275.2	2.4	286.0	25.0	275.2	2.4
CLM-6B_18	152.3	158.9	1.0	0.3126	0.0050	0.0426	0.0003	0.6464	0.0533	0.0008	268.9	1.9	331.0	34.0	268.9	1.9

CLM-6B_19	38.6	71.9	0.5	0.7661	0.0100	0.0938	0.0008	0.4953	0.0593	0.0007	577.9	5.1	574.0	26.0	577.9	5.1
CLM-6B_20	77.5	123.5	0.6	0.3086	0.0040	0.0432	0.0004	0.2419	0.0519	0.0007	272.4	2.7	273.0	33.0	272.4	2.7
CLM-6B_21	69.0	109.2	0.6	0.3122	0.0047	0.0433	0.0005	0.3162	0.0523	0.0008	273.4	3.3	287.0	34.0	273.4	3.3
CLM-6B_22	109.0	295	0.4	0.3133	0.0047	0.0439	0.0006	0.4974	0.0518	0.0007	276.7	3.5	276.0	33.0	276.7	3.5
CLM-6B_23	79.4	127.2	0.6	0.3129	0.0040	0.0428	0.0003	0.3284	0.0531	0.0007	270.1	2.1	326.0	27.0	270.1	2.1
CLM-6B_24	53.1	101.3	0.5	0.3062	0.0045	0.0427	0.0005	0.2692	0.0520	0.0008	269.5	3.1	274.0	37.0	269.5	3.1
CLM-6B_25	105.2	243	0.4	0.3030	0.0039	0.0425	0.0005	0.3014	0.0518	0.0007	268.1	3.0	271.0	33.0	268.1	3.0
CLM-6B_26	35.5	79.2	0.4	0.3067	0.0045	0.0430	0.0004	0.3313	0.0518	0.0008	271.3	2.4	263.0	33.0	271.3	2.4
CLM-6B_27	116.3	177.9	0.7	0.3081	0.0054	0.0430	0.0008	0.5425	0.0519	0.0008	271.7	4.7	276.0	37.0	271.7	4.7
CLM-6B_28	57.3	106.1	0.5	0.3074	0.0043	0.0433	0.0004	0.2759	0.0516	0.0008	273.0	2.4	253.0	36.0	273.0	2.4
CLM-6B_29	122.7	209	0.6	0.3087	0.0062	0.0424	0.0005	0.3754	0.0528	0.0009	267.8	3.1	310.0	37.0	267.8	3.1
CLM-6B_30	54.3	130.6	0.4	0.3131	0.0044	0.0429	0.0005	0.5604	0.0529	0.0006	271.0	3.2	317.0	27.0	271.0	3.2
CLM-6B_31	203.1	208	1.0	0.3086	0.0058	0.0429	0.0004	0.4199	0.0522	0.0009	271.0	2.6	281.0	40.0	271.0	2.6
CLM-6B_32	68.0	125.5	0.5	0.3148	0.0073	0.0433	0.0008	0.6000	0.0528	0.0010	273.0	5.0	308.0	45.0	273.0	5.0
CLM-6B_33	82.7	111.8	0.7	0.3113	0.0049	0.0436	0.0003	0.2212	0.0518	0.0008	275.3	2.0	266.0	36.0	275.3	2.0
CLM-6B_35	385.0	534	0.7	0.3078	0.0041	0.0433	0.0006	0.5956	0.0516	0.0007	273.2	3.7	260.0	29.0	273.2	3.7
CLM-6B_36	104.8	149.6	0.7	0.3108	0.0038	0.0433	0.0004	0.2700	0.0521	0.0007	273.4	2.3	280.0	30.0	273.4	2.3
CLM-6B_37	234.0	270	0.9	0.3151	0.0043	0.0434	0.0004	0.2043	0.0527	0.0007	273.8	2.6	310.0	32.0	273.8	2.6
CLM-6B_38	213.3	275.1	0.8	0.3075	0.0037	0.0431	0.0004	0.6444	0.0518	0.0005	271.9	2.6	272.0	23.0	271.9	2.6
CLM-6B_39	21.7	92.5	0.2	0.3119	0.0048	0.0435	0.0004	0.3699	0.0521	0.0008	274.3	2.4	277.0	34.0	274.3	2.4
CLM-6B_40	139.8	178.3	0.8	0.3076	0.0036	0.0429	0.0004	0.4453	0.0520	0.0006	271.1	2.6	275.0	27.0	271.1	2.6
CLM-6B_41	48.2	128.7	0.4	0.3097	0.0057	0.0434	0.0005	0.3429	0.0518	0.0009	273.6	2.9	269.0	40.0	273.6	2.9
CLM-6B_42	159.1	215.6	0.7	0.3118	0.0067	0.0433	0.0006	0.2682	0.0523	0.0012	273.0	4.0	291.0	51.0	273.0	4.0
CLM-6B_44	255.6	282.2	0.9	0.3277	0.0044	0.0456	0.0005	0.5837	0.0521	0.0006	287.5	3.0	283.0	24.0	287.5	3.0
CLM-6B_45	109.9	202.4	0.5	0.3121	0.0056	0.0434	0.0006	0.5399	0.0521	0.0008	274.0	3.4	282.0	36.0	274.0	3.4
CLM-6B_46	71.5	106.8	0.7	0.3141	0.0056	0.0433	0.0004	0.1779	0.0526	0.0010	273.5	2.6	298.0	42.0	273.5	2.6
CLM-6B_47	85.4	171.6	0.5	0.3141	0.0060	0.0437	0.0006	0.4341	0.0522	0.0010	275.7	3.8	279.0	41.0	275.7	3.8
CLM-6B_48	241.1	277	0.9	0.3160	0.0037	0.0440	0.0004	0.5329	0.0521	0.0005	277.5	2.4	284.0	23.0	277.5	2.4
CLM-6B_49	87.1	164.4	0.5	0.3179	0.0066	0.0433	0.0006	0.2537	0.0533	0.0012	273.1	3.4	321.0	49.0	273.1	3.4

CLM-6B_50	93.9	180	0.5	0.3091	0.0040	0.0433	0.0004	0.1652	0.0518	0.0007	273.2	2.2	270.0	32.0	273.2	2.2
								R1								
R1_1	7594.8	8210	0.9	0.3120	0.0120	0.0434	0.0005	0.1328	0.0542	0.0021	273.8	3.4	368.0	82.0	273.8	3.4
R1_2	633.9	710	0.9	0.3236	0.0098	0.0440	0.0005	0.1878	0.0553	0.0017	277.4	2.9	426.0	66.0	277.4	2.9
R1_3	145.2	211	0.7	0.3150	0.0180	0.0429	0.0009	0.3318	0.0539	0.0033	270.7	5.2	370.0	130.0	270.7	5.2
R1_4	424.0	480	0.9	0.3350	0.0140	0.0445	0.0006	0.1550	0.0563	0.0024	280.3	3.7	426.0	92.0	280.3	3.7
R1_6	118.2	179	0.7	0.4500	0.0320	0.0446	0.0006	0.0003	0.0732	0.0045	281.4	3.9	930.0	120.0	281.4	3.9
R1_7	651.9	899	0.7	0.2980	0.0120	0.0437	0.0005	0.1241	0.0518	0.0020	275.6	3.4	243.0	83.0	275.6	3.4
R1_8	196.6	335.2	0.6	0.3230	0.0130	0.0440	0.0005	0.1803	0.0555	0.0023	277.4	3.2	394.0	89.0	277.4	3.2
R1_9	161.4	231	0.7	0.3930	0.0240	0.0451	0.0006	0.0007	0.0668	0.0041	284.5	3.5	730.0	120.0	284.5	3.5
R1_10	80.9	138	0.6	0.3040	0.0160	0.0445	0.0006	0.1082	0.0511	0.0027	280.8	3.5	250.0	100.0	280.8	3.5
R1_12	47.8	57	0.8	0.3900	0.0320	0.0447	0.0013	0.2153	0.0664	0.0053	282.0	7.7	730.0	170.0	282.0	7.7
R1_14	23.3	32.17	0.7	0.3110	0.0110	0.0438	0.0005	0.1754	0.0532	0.0019	276.0	2.8	325.0	81.0	276.0	2.8
R1_15	9.8	10.5	0.9	0.3060	0.0130	0.0440	0.0005	0.2529	0.0528	0.0024	277.4	2.8	283.0	95.0	277.4	2.8
R1_16	45.8	81.16	0.6	0.3180	0.0140	0.0421	0.0005	0.0576	0.0568	0.0025	265.8	3.2	422.0	89.0	265.8	3.2
R1_17	49.3	59.8	0.8	0.3190	0.0140	0.0426	0.0006	0.1580	0.0562	0.0026	268.6	3.6	428.0	93.0	268.6	3.6
R1_19	56.8	54.35	1.0	0.3190	0.0140	0.0453	0.0006	0.3043	0.0539	0.0026	286.5	3.7	320.0	98.0	286.5	3.7
R1_20	62.6	91.6	0.7	0.3370	0.0130	0.0446	0.0005	0.1604	0.0568	0.0022	281.2	3.3	444.0	83.0	281.2	3.3
R1_21	63.7	68.8	0.9	0.3290	0.0150	0.0437	0.0005	0.1100	0.0554	0.0024	275.7	3.1	400.0	93.0	275.7	3.1
R1_23	45.0	63.9	0.7	0.3240	0.0180	0.0444	0.0006	0.0786	0.0543	0.0029	279.8	3.6	410.0	110.0	279.8	3.6
R1_25	76.1	77.5	1.0	0.2980	0.0220	0.0440	0.0006	0.3092	0.0516	0.0039	277.3	3.6	190.0	140.0	277.3	3.6
R1_26	113.0	151.1	0.7	0.3090	0.0200	0.0436	0.0006	0.3344	0.0517	0.0036	274.9	3.7	240.0	140.0	274.9	3.7
R1_27	57.9	57	1.0	0.3180	0.0110	0.0440	0.0006	0.1999	0.0529	0.0018	277.6	3.6	310.0	74.0	277.6	3.6
R1_28	377.0	469	0.8	0.3045	0.0079	0.0429	0.0005	0.3030	0.0526	0.0014	270.8	3.1	305.0	59.0	270.8	3.1
R1_29	15.3	41.6	0.4	1.5120	0.0220	0.1553	0.0011	0.2867	0.0713	0.0011	930.6	6.4	974.0	31.0	930.6	6.4
R1_30	51.2	52.5	1.0	0.3670	0.0190	0.0449	0.0006	0.1702	0.0597	0.0031	283.2	3.6	560.0	110.0	283.2	3.6
R1_31	197.8	214	0.9	0.3080	0.0150	0.0438	0.0005	0.2855	0.0518	0.0026	276.3	3.2	260.0	100.0	276.3	3.2
R1_32	384.7	484	0.8	0.3130	0.0130	0.0439	0.0005	0.0285	0.0524	0.0020	277.1	3.1	311.0	80.0	277.1	3.1
R1_33	161.3	216.2	0.7	0.3750	0.0130	0.0466	0.0007	0.3217	0.0588	0.0022	293.7	4.3	533.0	79.0	293.7	4.3

R1_34	36.6	64.8	0.6	0.3180	0.0200	0.0441	0.0007	0.3452	0.0532	0.0036	278.2	4.2	330.0	130.0	278.2	4.2
R1_35	71.1	93.6	0.8	0.3260	0.0130	0.0424	0.0005	0.3270	0.0562	0.0023	267.7	2.9	440.0	86.0	267.7	2.9
R1_36	118.8	124.4	1.0	0.3050	0.0100	0.0425	0.0005	0.1535	0.0524	0.0018	268.1	2.8	301.0	74.0	268.1	2.8
R1_37	20.7	122.6	0.2	0.2970	0.0071	0.0412	0.0006	0.2525	0.0524	0.0011	260.4	3.6	298.0	51.0	260.4	3.6
R1_38	12.2	55	0.2	1.7410	0.0260	0.1738	0.0014	0.2854	0.0728	0.0011	1033.4	7.5	1008.0	29.0	1008.0	29.0
R1_39	101.2	139.9	0.7	0.2968	0.0089	0.0417	0.0005	0.1791	0.0524	0.0015	263.1	2.8	290.0	64.0	263.1	2.8
R1_40	184.2	209.1	0.9	0.3060	0.0180	0.0433	0.0006	0.2961	0.0519	0.0034	273.1	3.9	220.0	130.0	273.1	3.9
R1_41	1012.2	914	1.1	0.3130	0.0120	0.0433	0.0006	0.2240	0.0522	0.0020	272.9	3.5	300.0	85.0	272.9	3.5
R1_42	151.9	179.5	0.8	0.3050	0.0130	0.0430	0.0006	0.1652	0.0509	0.0022	271.4	3.5	238.0	88.0	271.4	3.5
R1_44	172.6	201.8	0.9	0.3230	0.0150	0.0434	0.0005	0.1750	0.0539	0.0026	273.8	3.3	330.0	100.0	273.8	3.3
								E4								
CB1-E4 - 1	194	476	0.4	0.293	0.011	0.04127	0.00076	0.7416	0.0529	0.0014	260.7	4.7	320.0	61.0	260.7	4.7
CB1-E4 - 2	252	207	1.2	0.3069	0.0085	0.04294	0.00069	-0.026	0.0518	0.0015	271.0	4.2	269.0	65.0	271.0	4.2
CB1-E4 - 3	11.23	88.8	0.1	0.287	0.013	0.03965	0.00077	0.109	0.0524	0.0023	250.7	4.8	319.0	100.0	250.7	4.8
CB1-E4 - 4	195.5	178.3	1.1	0.308	0.025	0.0429	0.0011	0.1636	0.0523	0.0042	270.9	7.1	280.0	180.0	270.9	7.1
CB1-E4 - 5	6.58	106	0.1	0.238	0.011	0.03142	0.00082	0.3974	0.0541	0.0018	199.4	5.1	366.0	77.0	199.4	5.1
CB1-E4 - 6	175	224	0.8	0.3046	0.0082	0.0429	0.00068	0.2557	0.0521	0.0014	270.8	4.2	294.0	64.0	270.8	4.2
CB1-E4 - 7	346	584	0.6	0.3076	0.0086	0.04286	0.0006	0.2912	0.053	0.0014	270.5	3.7	323.0	63.0	270.5	3.7
CB1-E4 - 8	94.3	143.9	0.7	0.3102	0.0097	0.04328	0.00074	0.3262	0.0522	0.0016	273.1	4.6	286.0	70.0	273.1	4.6
CB1-E4 - 9	162	246	0.7	0.2996	0.0097	0.04133	0.00075	-0.042	0.053	0.0019	261.1	4.7	315.0	84.0	261.1	4.7
CB1-E4 - 10	115.9	138.2	0.8	0.301	0.012	0.04241	0.00092	0.6175	0.0518	0.0017	267.8	5.7	268.0	76.0	267.8	5.7
CB1-E4 - 11	163.1	503	0.3	0.3058	0.0059	0.04299	0.00094	0.372	0.0519	0.0013	271.3	5.8	278.0	57.0	271.3	5.8
CB1-E4 - 12	236	236	1.0	0.298	0.016	0.04199	0.00078	-0.157	0.0518	0.003	265.2	4.8	260.0	130.0	265.2	4.8
CB1-E4 - 13	32	402	0.1	0.2234	0.0085	0.03164	0.00052	0.3814	0.051	0.0017	200.8	3.3	248.0	81.0	200.8	3.3
CB1-E4 - 20	164	212	0.8	0.3139	0.0098	0.04375	0.00069	0.1298	0.0519	0.0017	276.0	4.3	272.0	73.0	276.0	4.3
CB1-E4 - 21	8.48	821	0.0	0.2565	0.0063	0.0366	0.00066	0.5225	0.0507	0.0012	231.7	4.1	224.0	54.0	231.7	4.1
CB1-E4 - 22	160.1	205.9	0.8	0.311	0.012	0.04375	0.00078	0.6298	0.0527	0.0016	276.0	4.8	309.0	71.0	276.0	4.8
CB1-E4 - 25	126.5	143.9	0.9	0.3132	0.01	0.04364	0.00076	0.0116	0.0519	0.0018	275.4	4.7	272.0	80.0	275.4	4.7
CB1-E4 - 26	62	342.8	0.2	0.2924	0.0069	0.04109	0.00067	0.5902	0.05196	0.0011	259.6	4.1	280.0	50.0	259.6	4.1
CB1-E4 - 27	262	236	1.1	0.2991	0.0095	0.04231	0.00075	0.5151	0.0513	0.0014	267.1	4.7	268.0	62.0	267.1	4.7

CB1-E4 - 28	169.3	211	0.8	0.3043	0.01	0.0423	0.00067	0.2727	0.0529	0.0016	267.1	4.2	332.0	74.0	267.1	4.2
CB1-E4 - 31	167	432	0.4	0.3035	0.0077	0.04226	0.00076	0.6033	0.05172	0.0011	266.8	4.7	269.0	50.0	266.8	4.7
CB1-E4 - 32	130.1	531	0.2	1.426	0.053	0.1391	0.0024	0.472	0.0756	0.0026	840.0	14.0	1080.0	69.0	1080.0	69.0
CB1-E4 - 33	29.7	547	0.1	0.2506	0.0058	0.03612	0.0007	0.6165	0.05075	0.0011	228.7	4.4	225.0	50.0	228.7	4.4
CB1-E4 - 34	126.2	145	0.9	0.3196	0.0084	0.04392	0.00072	0.1332	0.0522	0.0014	277.1	4.4	294.0	63.0	277.1	4.4
CB1-E4 - 35	220	304	0.7	0.3115	0.007	0.04327	0.00069	0.2086	0.0524	0.0012	273.1	4.2	299.0	53.0	273.1	4.2
CB1-E4 - 36	128.5	169	0.8	0.3185	0.0072	0.04341	0.00067	0.0799	0.0533	0.0013	273.9	4.1	335.0	55.0	273.9	4.1
CB1-E4 - 37	172.5	234	0.7	0.3083	0.0079	0.04329	0.00065	0.448	0.0518	0.0013	273.2	4.0	270.0	57.0	273.2	4.0
CB1-E4 - 38	163	431	0.4	0.3122	0.0076	0.04342	0.00077	0.394	0.0523	0.0012	274.0	4.8	301.0	51.0	274.0	4.8
CB1-E4 - 39	175	275	0.6	0.3108	0.0098	0.04325	0.00084	0.3894	0.0524	0.0016	273.0	5.2	308.0	64.0	273.0	5.2
CB1-E4 - 40	135	156	0.9	0.3113	0.01	0.0433	0.00066	0.2759	0.052	0.0016	273.3	4.1	274.0	72.0	273.3	4.1
CB1-E4 - 43	182	197	0.9	0.3072	0.01	0.04334	0.00072	-0.078	0.0513	0.0017	273.5	4.4	278.0	63.0	273.5	4.4
CB1-E4 - 44	51.08	267	0.2	0.2577	0.01	0.03581	0.00091	0.5435	0.0534	0.0019	226.8	5.7	336.0	81.0	226.8	5.7
CB1-E4 - 45	128	410	0.3	0.3111	0.0093	0.0432	0.00095	0.5071	0.0529	0.0014	272.6	5.9	331.0	64.0	272.6	5.9
CB1-E4 - 46	255	703	0.4	0.2876	0.0095	0.04056	0.00082	0.7708	0.0519	0.0015	256.3	5.1	278.0	66.0	256.3	5.1
CB1-E4 - 47	145	176.6	0.8	0.3168	0.0095	0.04416	0.00082	0.4339	0.0526	0.0014	278.6	5.1	306.0	60.0	278.6	5.1
CB1-E4 - 48	429	823	0.5	0.3036	0.011	0.0424	0.0013	0.6788	0.0518	0.0016	267.7	8.1	272.0	71.0	267.7	8.1
CB1-E4 - 49	119	213	0.6	0.3009	0.0082	0.04215	0.00063	0.3407	0.0518	0.0014	266.1	3.9	271.0	60.0	266.1	3.9
CB1-E4 - 50	20.9	381	0.1	0.2793	0.0099	0.03951	0.00063	0.4998	0.0514	0.0017	249.8	3.9	254	74	249.8	3.9
CB1-E4 - 51	232	246.9	0.9	0.307	0.013	0.04258	0.0011	0.4214	0.053	0.0019	268.8	6.8	320	83	268.8	6.8
CB2-E4 - 3	103	297	0.3	0.258	0.013	0.03615	0.00084	0.2361	0.0516	0.0027	228.9	5.2	290	100	228.9	5.2
CB2-E4 - 4	64	469	0.1	0.19	0.0097	0.02709	0.00064	0.4625	0.0508	0.0021	172.3	4	249	85	172.3	4
CB2-E4 - 5	168	555	0.3	0.2886	0.0071	0.0412	0.00096	0.3681	0.0509	0.0014	260.2	5.9	243	60	260.2	5.9
CB2-E4 - 6	74.4	345.4	0.2	0.2844	0.007	0.04	0.00059	0.2627	0.0513	0.0014	252.8	3.7	248	65	252.8	3.7
CB2-E4 - 7	424	425	1.0	0.3122	0.008	0.04396	0.00061	0.4179	0.05144	0.0011	277.4	3.8	257	48	277.4	3.8
CB2-E4 - 8	170.7	233.9	0.7	0.3101	0.0081	0.04382	0.00065	0.4638	0.0512	0.0013	276.5	4	244	57	276.5	4
CB2-E4 - 11	187	496	0.4	0.2708	0.0089	0.03877	0.00089	0.3642	0.0512	0.0015	245.2	5.5	243	68	245.2	5.5
CB2-E4 - 12	549	1160	0.5	0.2526	0.006	0.03616	0.00078	0.3313	0.0512	0.0014	229	4.9	244	63	229	4.9
CB2-E4 - 16	260	425	0.6	0.4598	0.011	0.05935	0.0011	0.4256	0.0563	0.0013	371.7	6.7	460	52	371.7	6.7
CB2-E4 - 17	109	423	0.3	0.2567	0.0083	0.0369	0.0006	0.5486	0.0512	0.0014	233.6	3.7	241	61	233.6	3.7

CB2-E4 - 18	916	1120	0.8	0.623	0.028	0.0786	0.0024	0.7032	0.0579	0.002	487	15	522	75	487	15
CB2-E4 - 19	188.7	572	0.3	0.2537	0.01	0.03611	0.00074	0.5618	0.0507	0.0017	228.7	4.6	219	78	228.7	4.6
CB2-E4 - 20	130	454	0.3	0.2547	0.0065	0.03657	0.00063	0.3622	0.0507	0.0012	231.5	3.9	230	56	231.5	3.9
CB2-E4 - 21	261.5	405	0.6	0.306	0.011	0.04252	0.00069	0.2602	0.0523	0.0018	268.4	4.3	291	80	268.4	4.3
CB2-E4 - 22	102	1188	0.1	0.2455	0.0062	0.03396	0.00074	0.363	0.0527	0.0013	215.3	4.6	312	56	215.3	4.6
CB2-E4 - 23	487	456	1.1	0.3092	0.0089	0.04349	0.00078	0.5504	0.0509	0.0013	274.4	4.8	241	60	274.4	4.8
CB2-E4 - 24	11.21	517	0.0	0.2571	0.0062	0.03681	0.00056	0.3105	0.05031	0.0011	233.1	3.5	214	48	233.1	3.5
CB2-E4 - 25	479	523	0.9	0.2989	0.0077	0.04196	0.00097	0.6334	0.0523	0.0013	265	6	297	54	265	6
CB2-E4 - 26	335	912	0.4	0.2648	0.0063	0.03775	0.0008	0.4225	0.05007	0.001	238.9	5	195	48	238.9	5
CB2-E4 - 27	293	677	0.4	0.2594	0.0067	0.03688	0.00063	0.4972	0.05118	0.0011	233.4	3.9	250	53	233.4	3.9
CB2-E4 - 28	389	1094	0.4	0.2599	0.0084	0.03684	0.00082	0.5711	0.05052	0.001	233.2	5.1	217	47	233.2	5.1
CB2-E4 - 29	151.6	752	0.2	0.1881	0.0067	0.02712	0.00064	0.3299	0.0503	0.0018	172.5	4	200	82	172.5	4
CB2-E4 - 30	260	721	0.4	0.2572	0.0049	0.03591	0.0006	0.4812	0.05183	0.0011	227.4	3.8	276	50	227.4	3.8
CB2-E4 - 31	467.1	882	0.5	0.2395	0.0049	0.03483	0.00064	0.1034	0.04969	0.00095	220.7	4	178	45	220.7	4
CB2-E4 - 32	402	1075	0.4	0.2543	0.0087	0.03579	0.001	0.4706	0.0523	0.0016	226.7	6.2	294	70	226.7	6.2
CB2-E4 - 33	410	739	0.6	0.2476	0.0064	0.03548	0.00052	0.3481	0.05071	0.0011	224.7	3.2	234	54	224.7	3.2
CB2-E4 - 34	300	427	0.7	0.3212	0.01	0.04402	0.00078	0.2533	0.053	0.0016	277.7	4.8	320	71	277.7	4.8
CB2-E4 - 35	274	342	0.8	0.3047	0.0076	0.04298	0.00073	0.2828	0.0512	0.0013	271.3	4.5	255	64	271.3	4.5
CB2-E4 - 36	208	368	0.6	1.903	0.033	0.1821	0.0033	0.5898	0.0755	0.0015	1078	18	1080	40	1080	40
CB2-E4 - 37	13.41	366	0.0	0.2559	0.0089	0.03589	0.00089	-0.075	0.0518	0.0022	227.3	5.5	268	97	227.3	5.5
CB2-E4 - 40	422	810	0.5	0.2524	0.0053	0.03574	0.00075	0.2439	0.0512	0.0013	226.4	4.7	253	55	226.4	4.7
CB2-E4 - 41	168.6	508	0.3	0.271	0.0075	0.03653	0.00059	0.319	0.0535	0.0016	231.3	3.7	368	61	231.3	3.7
CB2-E4 - 42	112.5	464	0.2	0.2541	0.0064	0.03595	0.00058	0.3053	0.052	0.0013	227.7	3.6	286	58	227.7	3.6
CB2-E4 - 43	156	406	0.4	0.2657	0.008	0.037	0.00095	0.6524	0.0525	0.0014	234.2	5.9	302	60	234.2	5.9
CB2-E4 - 44	251	629	0.4	0.2462	0.0054	0.03519	0.00064	0.4635	0.05068	0.0011	222.9	4	222	50	222.9	4
CB2-E4 - 45	23.9	164	0.1	0.167	0.011	0.02289	0.00055	0.3618	0.0534	0.0032	145.9	3.5	370	120	145.9	3.5
CB2-E4 - 46	275.2	521	0.5	0.2587	0.007	0.03641	0.00061	0.7367	0.05154	0.0011	230.5	3.8	270	45	230.5	3.8
CB2-E4 - 47	242.9	531	0.5	0.2571	0.0065	0.03694	0.00059	0.4909	0.05056	0.0011	233.8	3.7	215	51	233.8	3.7
CB2-E4 - 48	407	856	0.5	0.2547	0.0057	0.03602	0.00056	0.5819	0.05133	0.00098	228.1	3.5	252	44	228.1	3.5

CB1-GG08 - 5	207	412	0.5	0.2916	0.0074	0.04067	0.00073	0.4249	0.0522	0.0013	257	4.5	289	58	257	4.5
CB1-GG08 - 6	174	176.2	1.0	0.3073	0.011	0.04374	0.00065	-0.242	0.0514	0.0019	276	4	248	86	276	4
CB1-GG08 - 7	205.3	304	0.7	0.318	0.011	0.04529	0.001	0.3825	0.0512	0.0019	285.6	6.2	245	86	285.6	6.2
CB1-GG08 - 10	131.3	183.7	0.7	0.3095	0.0099	0.04317	0.00083	0.134	0.0524	0.0017	272.5	5.1	294	71	272.5	5.1
CB1-GG08 - 11	8.89	473	0.0	0.2503	0.0072	0.03558	0.00076	0.5966	0.0505	0.0014	225.4	4.7	228	67	225.4	4.7
CB1-GG08 - 12	209	243	0.9	0.3108	0.0092	0.04416	0.00078	0.4855	0.0511	0.0013	278.6	4.8	239	61	278.6	4.8
CB1-GG08 - 13	369.6	792.6	0.5	0.3118	0.0086	0.04408	0.00075	0.67	0.05126	0.0011	278.1	4.6	249	50	278.1	4.6
CB1-GG08 - 14	337	361	0.9	0.307	0.013	0.04345	0.00082	0.1654	0.0521	0.0016	274.1	5.1	285	72	274.1	5.1
CB1-GG08 - 18	126.5	559	0.2	0.1904	0.0086	0.0245	0.00051	0.3961	0.0563	0.0024	156	3.2	457	95	156	3.2
CB1-GG08 - 19	152.8	183.8	0.8	0.302	0.012	0.04202	0.00073	0.3513	0.052	0.002	265.3	4.5	274	89	265.3	4.5
CB1-GG08 - 20	270	277	1.0	0.302	0.0092	0.04304	0.00088	0.4048	0.0509	0.0016	271.7	5.5	243	75	271.7	5.5
CB1-GG08 - 21	270	307	0.9	0.3156	0.01	0.04364	0.0007	0.4797	0.0528	0.0018	275.4	4.3	315	77	275.4	4.3
CB2-GG08 - 1	172	171	1.0	0.325	0.0094	0.04497	0.00088	0.2807	0.0524	0.0016	283.5	5.5	290	71	283.5	5.5
CB2-GG08 - 2	241	362	0.7	0.3122	0.0069	0.04332	0.00066	0.4642	0.05228	0.0011	273.4	4.1	313	44	273.4	4.1
CB2-GG08 - 9	302	306	1.0	0.2836	0.0087	0.04005	0.00068	0.1015	0.0513	0.0016	253.2	4.2	262	76	253.2	4.2
CB2-GG08 - 10	151.3	282	0.5	0.2538	0.0089	0.03668	0.00076	0.1255	0.0507	0.0019	232.2	4.7	218	85	232.2	4.7
CB2-GG08 - 11	69.9	176	0.4	0.267	0.012	0.0318	0.0014	-0.124	0.0607	0.0043	201.7	8.6	600	160	201.7	8.6
CB2-GG08 - 13	232	186	1.2	0.3086	0.0074	0.04295	0.00079	0.4323	0.0517	0.0014	271.7	4.7	264	61	271.7	4.7
CB2-GG08 - 14	225	364	0.6	0.305	0.0093	0.04245	0.00075	0.5042	0.05249	0.0012	268	4.7	304	50	268	4.7
CB2-GG08 - 15	49.46	43.3	1.1	0.455	0.024	0.0596	0.0013	0.6695	0.0551	0.0024	373.3	8.2	405	98	373.3	8.2
CB2-GG08 - 16	31.3	117.4	0.3	0.322	0.016	0.03855	0.00074	-0.055	0.0606	0.0031	243.8	4.6	600	110	243.8	4.6
CB2-GG08 - 17	19.09	79.5	0.2	0.283	0.011	0.03929	0.00096	0.5427	0.0532	0.002	248.4	5.9	325	84	248.4	5.9
CB2-GG08 - 18	47.4	261.4	0.2	0.253	0.012	0.03607	0.00065	0.5025	0.0511	0.0017	228.4	4.1	238	79	228.4	4.1
CB2-GG08 - 19	97.8	122.2	0.8	0.3047	0.01	0.04334	0.00066	0.2765	0.0505	0.0017	273.5	4.1	218	76	273.5	4.1
CB2-GG08 - 20	262	245	1.1	0.304	0.0073	0.04227	0.00063	0.2497	0.05203	0.0012	267.4	4	281	51	267.4	4
CB2-GG08 - 21	76.1	247	0.3	0.1706	0.007	0.02448	0.00044	-0.108	0.0507	0.0023	155.9	2.8	240	110	155.9	2.8
CB2-GG08 - 22	2090	1321	1.6	0.1676	0.0043	0.02434	0.0004	0.4418	0.04966	0.00099	155	2.5	176	46	155	2.5
CB2-GG08 - 23	122.3	143.1	0.9	0.3053	0.0076	0.04328	0.00077	0.2362	0.0507	0.0016	273.1	4.7	219	72	273.1	4.7
CB2-GG08 - 24	136	207.3	0.7	0.2976	0.008	0.04216	0.00077	0.2942	0.0512	0.0014	266.2	4.8	253	67	266.2	4.8

CB2-GG08 - 25	354	300	1.2	0.318	0.011	0.0425	0.00067	0.025 1	0.0543	0.0019	268.3	4.2	376	80	268.3	4.2
CB2-GG08 - 26	234.2	482	0.5	0.31	0.011	0.04295	0.00098	0.094 8	0.0527	0.0015	271.1	6	312	68	271.1	6

Table 2. Hf isotopic compositions of the analyzed standard zircons.

Spot No.	176Hf/177Hf	2σ	176Lu/177Hf	2σ	176Yb/177Hf	2σ	(176Hf/177Hf)i	ƐHf0	2σ	ƐHfi
CLM4A										
CLM4A_1	0.282644	0.000017	0.001418	0.000057	0.049	0.0019	0.282637	-4.986120	0.601514	0.680085
CLM4A_2	0.282659	0.000017	0.001519	0.00006	0.0539	0.0031	0.282651	-4.455682	0.601482	1.193045
CLM4A_3	0.282612	0.000031	0.0011199	0.0000025	0.04099	0.00079	0.282606	-6.117722	1.097003	-0.399673
CLM4A_4	0.282623	0.000014	0.00172	0.00011	0.0606	0.0049	0.282614	-5.728734	0.495402	-0.116168
CLM4A_5	0.282656	0.000021	0.002062	0.000044	0.07468	0.00073	0.282646	-4.561770	0.743016	0.991240
CLM4A_6	0.282606	0.000024	0.000852	0.000043	0.0309	0.0025	0.282602	-6.329897	0.849311	-0.564781
CLM4A_7	0.282658	0.000021	0.001734	0.000053	0.062	0.0012	0.282649	-4.491044	0.743010	1.119787
CLM4A_8	0.28263	0.000021	0.00125	0.000095	0.0451	0.0043	0.282624	-5.481196	0.743084	0.214311
CLM4A_9	0.282623	0.000024	0.001365	0.000079	0.0507	0.0044	0.282616	-5.728734	0.849260	-0.053632
CLM4A_10	0.282659	0.000026	0.002053	0.00005	0.072	0.0019	0.282649	-4.455682	0.919911	1.098976
CLM4A_11	0.28264	0.000022	0.00169	0.00012	0.0659	0.007	0.282632	-5.127570	0.778439	0.490636
CLM4A_12	0.282659	0.000032	0.0019	0.00024	0.0672	0.0099	0.282650	-4.455682	1.132202	1.125929
CLM4A_13	0.282645	0.000024	0.00158	0.000064	0.0564	0.0027	0.282637	-4.950758	0.849191	0.686931
CLM4A_14	0.282628	0.000024	0.001299	0.000064	0.0462	0.0022	0.282622	-5.551921	0.849245	0.134912
CLM4A_15	0.282651	0.000026	0.00163	0.00012	0.0633	0.0034	0.282643	-4.738582	0.919940	0.890424
CLM4A_16	0.282656	0.000019	0.001677	0.00002	0.05984	0.00084	0.282648	-4.561770	0.672250	1.059062
CLM4A_17	0.282646	0.000024	0.001487	0.000082	0.0527	0.0037	0.282639	-4.915395	0.849188	0.738697
CLM4A_18	0.282634	0.000021	0.001811	0.000036	0.0646	0.0015	0.282625	-5.339746	0.743071	0.257020
CLM4A_19	0.282633	0.00002	0.001553	0.000088	0.0535	0.0022	0.282625	-5.375108	0.707692	0.267085
CLM4A_20	0.282645	0.000022	0.001849	0.000069	0.0663	0.0021	0.282636	-4.950758	0.778425	0.639544
CLM5										
CLM5_1	0.282613	0.000021	0.0006	0.000022	0.02122	0.00098	0.282610	-6.082359	0.743129	-0.283659
CLM5_2	0.282647	0.000038	0.001173	0.000025	0.03942	0.00087	0.282641	-4.880033	1.344543	0.818630
CLM5_3	0.282595	0.000019	0.000388	0.00001	0.01362	0.00054	0.282593	-6.718885	0.672397	-0.883285
CLM5_4	0.282589	0.000016	0.0003884	0.0000059	0.01379	0.00027	0.282587	-6.931061	0.566241	-1.095656
CLM5_5	0.282577	0.000021	0.000399	0.0000062	0.01427	0.00012	0.282575	-7.355411	0.743221	-1.522122
CLM5_6	0.28264	0.00003	0.000745	0.000012	0.02531	0.00047	0.282636	-5.127570	1.061507	0.646199

CLM5_7	0.282579	0.000019	0.0003664	0.0000049	0.01311	0.00019	0.282577	-7.284686	0.672433	-1.445623
CLM5_8	0.28262	0.000019	0.0006269	0.0000031	0.0228	0.00053	0.282617	-5.834822	0.672336	-0.040704
CLM5_9	0.282585	0.000017	0.0003259	0.0000056	0.01145	0.00013	0.282583	-7.072511	0.601640	-1.226201
CLM5_10	0.282593	0.000016	0.000455	0.0000019	0.01619	0.00021	0.282591	-6.789610	0.566231	-0.965833
CLM5_11	0.282607	0.000023	0.0004762	0.0000061	0.01709	0.00019	0.282605	-6.294535	0.813920	-0.474192
CLM5_12	0.282633	0.000029	0.001291	0.000097	0.0434	0.0036	0.282627	-5.375108	1.026149	0.302514
CLM5_13	0.282646	0.000039	0.0006824	0.0000068	0.02742	0.00039	0.282643	-4.915395	1.379930	0.869507
CLM5_14	0.282629	0.000017	0.000614	0.000025	0.02232	0.00055	0.282626	-5.516559	0.601546	0.280015
CLM5_15	0.28259	0.000021	0.000402	0.000013	0.01533	0.00064	0.282588	-6.895698	0.743189	-1.062664
CLM5_16	0.282595	0.000017	0.0004579	0.0000067	0.01702	0.00039	0.282593	-6.718885	0.601617	-0.895576
CLM5_17	0.2826	0.000013	0.0003474	0.0000042	0.01288	0.00025	0.282598	-6.542073	0.460052	-0.699230
CLM5_18	0.282592	0.000022	0.000365	0.00001	0.01356	0.00018	0.282590	-6.824973	0.778571	-0.985392
CLM5_19	0.282618	0.000023	0.000899	0.000017	0.03212	0.00089	0.282614	-5.905547	0.813886	-0.159314
CLM5_20	0.282597	0.00002	0.000482	0.000013	0.01787	0.00085	0.282595	-6.648160	0.707779	-0.829046
					CLM6A					
CLM6A_1	0.282608	0.000017	0.000557	0.000013	0.02021	0.00038	0.282605	-6.259172	0.601593	-0.288481
CLM6A_2	0.282641	0.000036	0.001044	0.000069	0.0431	0.0019	0.282636	-5.092208	1.273813	0.791138
CLM6A_3	0.282659	0.000017	0.001254	0.000081	0.0476	0.0019	0.282653	-4.455682	0.601482	1.390080
CLM6A_4	0.282636	0.000018	0.000969	0.00006	0.0363	0.0019	0.282631	-5.269021	0.636918	0.627778
CLM6A_5	0.282618	0.000019	0.000522	0.000014	0.02	0.00034	0.282615	-5.905547	0.672343	0.071687
CLM6A_7	0.282612	0.00002	0.000333	0.0000052	0.01256	0.00015	0.282610	-6.117722	0.707747	-0.106444
CLM6A_9	0.282636	0.000027	0.001168	0.000062	0.0385	0.0018	0.282630	-5.269021	0.955373	0.591797
CLM6A_10	0.282638	0.000026	0.000466	0.0000075	0.0183	0.00038	0.282636	-5.198296	0.919983	0.789493
CLM6A_11	0.282636	0.000016	0.000558	0.000014	0.02057	0.00042	0.282633	-5.269021	0.566149	0.702091
CLM6A_12	0.282625	0.000015	0.0004918	0.0000025	0.01821	0.00045	0.282622	-5.658009	0.530786	0.324836
CLM6A_13	0.28262	0.00002	0.000822	0.000026	0.0303	0.0016	0.282616	-5.834822	0.707724	0.088212
CLM6A_14	0.28259	0.000018	0.0002605	0.0000061	0.00879	0.00017	0.282589	-6.895698	0.637019	-0.871784
CLM6A_15	0.282616	0.000014	0.000684	0.000012	0.02496	0.00091	0.282613	-5.976272	0.495414	-0.028372
CLM6A_16	0.282623	0.000018	0.0005015	0.0000086	0.01791	0.00057	0.282620	-5.728734	0.636945	0.252314
CLM6A_17	0.282608	0.000023	0.000645	0.000018	0.02363	0.0007	0.282605	-6.259172	0.813920	-0.304393
CLM6A_18	0.282598	0.000019	0.0004436	0.0000072	0.01611	0.00052	0.282596	-6.612798	0.672390	-0.621818
CLM6A_19	0.282628	0.000019	0.000718	0.000021	0.02679	0.0009	0.282624	-5.551921	0.672321	0.390089
CLM6A_20	0.282662	0.000021	0.000892	0.000065	0.0332	0.0027	0.282657	-4.349594	0.743000	1.561685
					CLM6B					
CLM6B_2	0.282613	0.000024	0.000595	0.0000097	0.02389	0.00059	0.282610	-6.082359	0.849290	-0.118432
CLM6B_3	0.282665	0.000033	0.000973	0.000039	0.034	0.0012	0.282660	-4.243507	1.167559	1.653192

CLM6B_4	0.282646	0.000025	0.000703	0.000015	0.02499	0.00087	0.282642	-4.915395	0.884574	1.029714
CLM6B_5	0.282663	0.000017	0.000794	0.00004	0.02924	0.00086	0.282659	-4.314232	0.601474	1.614789
CLM6B_6	0.282627	0.000018	0.000484	0.0000045	0.01765	0.00027	0.282625	-5.587284	0.636938	0.397014
CLM6B_7	0.282612	0.000018	0.0004187	0.0000034	0.01602	0.00052	0.282610	-6.117722	0.636972	-0.121939
CLM6B_8	0.282641	0.000023	0.000518	0.000014	0.0197	0.001	0.282638	-5.092208	0.813825	0.886243
CLM6B_9	0.28265	0.000021	0.000634	0.00006	0.0255	0.0025	0.282647	-4.773945	0.743031	1.183726
CLM6B_10	0.282619	0.000021	0.000734	0.000038	0.0263	0.0017	0.282615	-5.870184	0.743113	0.068740
CLM6B_11	0.282632	0.00002	0.000765	0.000021	0.02739	0.00045	0.282628	-5.410471	0.707694	0.523127
CLM6B_12	0.282621	0.000025	0.000992	0.000064	0.0362	0.002	0.282616	-5.799459	0.884652	0.092859
CLM6B_13	0.282621	0.000025	0.0004761	0.0000058	0.01819	0.00034	0.282619	-5.799459	0.884652	0.186139
CLM6B_14	0.282636	0.000018	0.000426	0.000011	0.01567	0.00078	0.282634	-5.269021	0.636916	0.725958
CLM6B_15	0.282357	0.000021	0.000709	0.000015	0.02635	0.00092	0.282349	-15.135173	0.743803	-2.519034
CLM6B_16	0.28264	0.00002	0.000772	0.000031	0.02847	0.00064	0.282636	-5.127570	0.707674	0.804934
CLM6B_17	0.282639	0.000012	0.000634	0.000011	0.02404	0.00097	0.282636	-5.162933	0.424604	0.794501
CLM6B_18	0.28263	0.000021	0.000545	0.000028	0.02055	0.00095	0.282627	-5.481196	0.743084	0.492137
CLM6B_19	0.282626	0.000017	0.000513	0.000014	0.01988	0.00049	0.282623	-5.622646	0.601553	0.356387
CLM6B_20	0.282641	0.000019	0.000628	0.000028	0.02289	0.00082	0.282638	-5.092208	0.672288	0.866354

Table 3. Zircon trace elements (ppm) and related calculations.

Spot no.	Al	P	Ti	V	Cr	Zn	Y	Zr	Nb	Ba	Hf	206Pb	208Pb	Th	U
Sample CLM4A															
PJ1_CLM4A_2		2220	1.41	0.2		0.57	1013	503000	6.3	0.3	10720	119.4	8.22	332.4	684
PJ1_CLM4A_3	2.3	570	1.5		1.2	0.66	906	480600	5.4	0.2	10120	105.9	7.41	282	584
PJ1_CLM4A_6		195	2.78			0.39	1071	488000	3.4	0.1	9300	42.1	3.05	113.7	234
PJ1_CLM4A_7	12.3	6210	1.92	0.2		0.69	1175	494000	7.2	1.8	10920	103.5	6.04	239	595
PJ1_CLM4A_8	16.3	800	2.95	0.1		1.25	1444	484500	2.9	0.3	8940	48.2	3.98	152.3	273
PJ1_CLM4A_9	1.26	390	1.27			0.62	723	483000	4.4	0.2	10740	72.8	4.06	151	412
PJ1_CLM4A_10		230	1.71			0.56	1110	488000	2.7	0.1	9100	39.6	2.41	89	224
PJ2_CLM4A_2	69	1330	2.5	0.2		1.55	783	470000	3.4	0.2	9390	44	3.44	112.9	224
PJ2_CLM4A_4	8.2	790	2.12			0.53	1211	487100	7.7	0.1	9840	77.5	5.08	190.7	435
PJ2_CLM4A_5	1.14	1580	2			0.48	1341	479500	9.9	0.4	10100	88.3	4.22	160	483
PJ2_CLM4A_6	22.7	273	3.06	0.2		0.5	1610	470000	5.9	0.2	9110	69.8	8.6	336	379
PJ2_CLM4A_7		167.4	2.36			0.32	1029	476300	4.8	0.1	9430	71.8	6.24	243.8	398.8
PJ2_CLM4A_8	186	323	3.63	0.5		0.58	2057	469000	5.5	4.2	7890	75.4	7.16	266	405
PJ2_CLM4A_9	2.53	233	2.91	0.7		0.29	1835	484300	14.6	0.1	9750	103.6	6.74	273.1	579

Sample CLM5															
PJ1_CLM5_2		259.0	10.4	0.8		0.6	941.0	470300	2.5	0.2	8970.0	68.1	6.2	244.5	380.0
PJ1_CLM5_6	1.1	170.5	11.4	0.2		0.4	472.4	488000	1.2	0.1	9330.0	32.4	3.0	116.0	186.4
PJ1_CLM5_7	7.3	430.0	7.6	0.7		0.6	359.0	485800	1.4	0.1	11450.0	38.8	2.7	99.7	211.9
PJ1_CLM5_9	1.2	168.5	9.2	0.6		0.6	558.0	485000	1.5	0.1	10200.0	41.3	3.6	136.1	236.0
PJ1_CLM5_10		227.0	11.3	0.6		0.7	823.0	501100	1.8	0.1	9690.0	70.3	8.3	360.0	413.0
PJ2_CLM5_2		207.9	6.4	2.0		0.4	850.0	493000	2.2	0.1	9880.0	59.8	5.3	206.0	342.0
PJ2_CLM5_5	1.2	134.4	7.5	0.5		0.4	394.4	486300	1.4	0.1	11210.0	35.9	2.8	105.1	205.9
PJ2_CLM5_8		201.2	2.6	0.1		0.7	1207.0	478000	7.6	0.2	9150.0	113.4	10.8	422.4	613.0
PJ2_CLM5_9	9.0	271.0	6.5	1.7		0.4	1042.0	477000	3.3	0.3	11440.0	128.8	14.2	575.0	720.0
PJ2_CLM5_10		112.3	6.9	1.2		0.3	410.0	476300	1.1	0.0	11440.0	35.9	2.7	92.9	192.9
PJ2_CLM5_13	1.8	940.0	7.2	7.6		0.4	3010.0	473300	3.8	0.3	9490.0	142.4	25.0	1028.0	798.0
Sample CLM6A															
PJ2_CLM6_1	0.94	172.4	11.7	0.449		0.28	452	493000	1.365	0.049	10000	30.17	2.763	103	171.7
PJ2_CLM6_2		139.9	6.64	0.634		0.31	349	484400	1.587	0.053	11620	37.44	2.26	85.7	210.2
PJ2_CLM6_3		128.1	5.47	0.571		0.31	581	502000	1.397	0.05	9710	16.69	1.25	43.5	95.5
PJ2_CLM6_4	0.9	127.9	6.73	1.081		0.29	405.3	472300	1.278	0.063	11330	34	2.233	80.1	189
PJ2_CLM6_6	53	187.2	8	1.52		0.51	814	485100	1.75	0.72	10730	60.9	6.26	245	348
PJ2_CLM6_7		453	11.1	2.21		0.69	2743	456000	4.71	0.58	9020	227.5	45	1735	1234

Table 3. Continued

La	Ce	Pr	Nd	Sm	Eu	Gd	Tb	Dy	Ho	Er	Tm	Yb	Lu	ΣREE	Lu/LaN
15.9	49	4.6	22.7	6.36	0.8	17.77	5.8	75.4	30.77	151.6	36.9	377	76.9	871.5	46.1
4.9	23.2	1.4	7.2	3.7	0.5	14.3	4.9	67.7	27.36	137.2	33.2	340.7	69.5	735.8	135.2
0.3	14.9	0.1	1.95	3.05	0.9	17.64	6	78.9	32.1	161.2	39.1	399	85	840.2	2777.8
52.2	140	16.4	83.4	20	1.8	29.4	7.5	91.4	35.21	175.1	41.4	420	85.5	1199.3	15.6
7.6	30.7	2.2	13.1	7.3	1.7	29.4	9.2	114.7	44.3	211.1	50.4	505	103.6	1130.3	129.9
0.6	11.26	0.2	1.62	1.71	0.4	9.93	3.7	53.6	21.94	113	27.5	284	57.7	587.1	964.2
0.0	10	0.1	1.82	3.8	1.0	19.1	6.7	88	34	169	40	405	82	860.5	40196.0
3.2	20.1	1.3	8.4	4.18	0.8	13.8	4.4	57.3	23.45	120	29.2	301	64.6	651.7	192.3
3.3	27.8	1.2	7.3	3.87	0.8	17.27	6.3	85.8	35.7	188.2	45	473	100.3	995.8	289.8
15.1	48.5	4.4	21.7	6.5	0.7	19.1	6.6	92.6	38.7	207.5	50.2	531	116.7	1159.2	73.7
0.0	25.4	0.1	2.02	4.39	1.3	26.7	9.4	124	47.9	235	54.7	547	112.6	1190.6	41397.0
0.0	19.74	0.1	1.07	2.55	0.8	16.11	5.6	75.7	30.81	156	36.2	372.8	79.3	796.8	58309.0

0.3	21.16	0.2	3.38	6.47	2.0	37.3	12.5	157.4	60.6	298	67.2	679	142.8	1488.3	4666.7
0.3	28.92	0.2	1.71	3.59	0.9	23.2	8.9	126.5	54.47	289	70.5	740	156.3	1504.5	4690.9
0.0	15.1	0.1	1.5	2.9	0.8	16.0	5.3	71.1	28.5	140.4	32.2	308.2	65.8	687.7	48382.5
0.0	9.4	0.0	0.8	1.7	0.5	9.5	3.1	38.4	14.4	67.9	15.0	148.3	29.7	338.7	21867.5
3.2	17.3	0.9	5.0	1.9	0.2	6.7	2.1	28.0	11.2	54.4	12.7	125.8	25.4	295.0	75.7
0.0	11.8	0.0	0.7	1.9	0.3	10.5	3.5	45.2	17.2	82.1	18.5	183.0	36.5	411.5	26838.0
0.0	16.3	0.1	1.5	3.2	0.7	16.1	5.2	65.3	24.9	117.4	26.5	253.0	50.6	580.7	24804.0
0.0	13.7	0.1	1.1	2.5	0.6	14.4	5.0	65.4	25.8	125.7	29.0	284.0	57.9	625.1	42573.5
0.0	10.4	0.0	0.5	1.1	0.2	6.7	2.3	30.7	11.9	59.0	13.6	135.2	27.6	299.2	6759.8
0.0	21.1	0.1	1.1	2.8	0.8	18.9	6.8	92.8	36.6	183.2	42.1	424.0	87.6	917.9	42941.3
0.1	25.9	0.1	1.5	3.4	0.5	18.7	6.4	81.7	31.6	149.2	34.0	333.2	65.8	752.0	12095.6
0.0	8.7	0.0	0.4	1.1	0.2	7.0	2.4	31.8	12.4	62.0	14.1	136.9	28.6	305.7	14005.0
7.2	47.4	2.3	16.4	17.0	4.6	79.8	23.6	273.0	95.1	425.0	89.3	826.0	158.7	2065.4	210.1
0.0126	9.66	0.0369	0.673	1.56	0.393	8.93	2.96	37.7	14.35	68.2	15.44	148	29.7	337.6155	21838.0
0.014	10.57	0.0201	0.346	0.991	0.211	5.62	2.017	27.15	10.79	54.9	12.86	132.1	26.98	284.5691	19838.0
0.0094	6.87	0.032	0.77	1.82	0.504	11.5	3.71	47.3	18.21	87.7	19.9	199	40.2	437.5254	59118.0
0.0129	9.49	0.0237	0.423	1.082	0.231	6.32	2.298	30.53	12.15	60.4	14.22	143.6	29.98	310.7606	22044.0
0.024	13.97	0.0798	1.5	3.11	0.575	16.23	5.28	65.5	24.5	116.6	25.7	252	50	575.0688	18382.3
0.0683	43.3	0.447	7.4	13.54	1.906	67.1	20.59	241.2	85.6	379.3	79.2	715	136.8	1791.4513	18288.7

Table 3. Continued

Sm/LaN	Lu/GdN	Yb/SmN	Eu/Eu*	Ce/Ce*	Th/U
0.6	34.6	54.6	0.2	1.4	0.5
1.2	38.9	84.8	0.2	2.1	0.5
16.7	38.5	120.5	0.4	18.0	0.5
0.6	23.3	19.3	0.2	1.2	0.4
1.5	28.2	63.7	0.4	1.8	0.6
4.8	46.5	153.0	0.3	7.9	0.4
312.0	34.3	98.1	0.3	29.1	0.4
2.1	37.4	66.3	0.3	2.4	0.5
1.9	46.5	112.5	0.3	3.4	0.4
0.7	48.9	75.2	0.2	1.4	0.3

270.3	33.7	114.7	0.4	60.6	0.9
314.0	39.4	134.6	0.4	94.3	0.6
35.4	30.6	96.6	0.4	17.9	0.7
18.0	53.9	189.8	0.3	30.0	0.5
353.5	32.9	98.9	0.4	60.1	0.6
208.0	25.2	80.8	0.4	62.3	0.6
1.0	30.5	60.1	0.2	2.4	0.5
239.0	27.7	86.8	0.2	101.0	0.6
258.7	25.1	73.9	0.3	55.6	0.9
310.5	32.1	103.7	0.3	62.7	0.6
45.3	33.2	112.7	0.2	73.2	0.5
225.7	37.0	142.0	0.3	93.4	0.7
104.4	28.1	90.5	0.2	75.3	0.8
92.3	32.7	112.1	0.3	80.3	0.5
3.8	15.9	44.7	0.4	2.8	1.3
192.0	26.6	87.4	0.3	67.9	0.6
122.0	38.4	122.8	0.3	126.2	0.4
448.0	28.0	100.7	0.3	58.6	0.5
133.5	37.9	122.0	0.3	103.1	0.4
191.5	24.6	74.6	0.3	47.7	0.7
303.2	16.3	48.6	0.2	27.6	1.4

Table 4. Whole-rock analyses

Sample	**CLM4A**	**CLM5**	**CLM6A**	**GG-8**	**CI12**	**A-5**	**A-6**	**C-01**
wt. %								
SiO2	66.9	59.6	59.6	71.0	59.3	66.8	71.6	65.0
TiO2	0.5	0.8	0.7	0.3	0.8	0.2	0.2	0.6
Al2O3	16.0	15.7	15.9	15.5	16.9	19.2	16.1	15.4
Fe2O3	4.2	6.7	6.8					
FeO*	3.7	6.0	6.1	2.0	6.4	1.3	1.7	3.9
MgO	1.1	3.7	3.3	0.8	3.6	0.1	0.5	2.2
CaO	2.9	5.9	5.5	3.0	5.5	0.3	0.3	3.4
Na2O	4.2	3.3	3.3	5.1	4.2	10.3	5.5	4.2

K2O	3.4	2.6	2.4	0.9	1.4	0.2	1.9	2.7
P2O5	0.2	0.2	0.2	0.1	0.3	0.0	0.0	0.1
MnO	0.1	0.1	0.1	0.0	0.1	0.0	0.0	0.1
Cr2O3	0.0	0.0	0.0					
SrO	0.1	0.1	0.1					
BaO	0.3	0.1	0.1					
LOI	1.1	1.0	1.4	1.3	1.9	1.0	1.6	1.9
TOTAL	100.8	99.8	99.4	100.2	98.6	98.4	97.9	97.5
ppm								
Li	20	20	20					
Cr	20	90	80					
Co	5	18	21					
Ni	1	24	20					
Cu	5	55	53					
Zn	58	74	81					
Ga	20.5	20.4	23.6					
As	5	8	6					
Rb	72.9	73.6	77.8	20.5	40.9	5.5	67.2	78
Sr	665	665	668	553	697.6	255.6	288	357
Sn	5	2	2					
Cs	1.8	4.73	3.26	0.38	0.4	0.5	5.6	1.9
Ba	2420	1105	1010	386	459.9	92.5	136.5	622.7
Pb	10	15	13	15	13.8	5.2	6.6	9.6
Th	8.99	7.96	4.62	3.66	7.2	1.5	1.6	8.6
U	2.27	2.37	2.21	0.69	3.2	0.5	0.5	2.4
Nb	12.4	11.4	9.6	2.3	7.4	1.3	1.7	9.1
Zr	280	165	178	122	139.9	99.6	119	148.6
V	42	155	171					
Hf	6.4	4.1	4.5	3.1	3.6	2.7	3.1	4
Ta	0.7	1.1	0.9	0.2	0.7	0.1	0.1	0.8
W	3	3	3					
La	47.6	26.1	24.2	17.3	22.9	7.6	11.9	23.9
Ce	82	52.9	48.9	32.1	44.1	15.9	25.6	45.5
Pr	8.34	6.03	5.78	3.52	5.2	1.8	3.2	5.3
Nd	28.8	25.1	23	13	20.3	6.8	12.8	20.1
Sm	4.28	4.79	4.46	1.74	4.1	1.6	2.7	4.2

Eu	1.27	1.18	1.13	0.67	1.2	0.6	1	1.1
Gd	2.58	3.63	3.65	1.05	3.5	1.2	1.9	3.8
Tb	0.36	0.55	0.52	0.14	0.5	0.2	0.2	0.6
Dy	2.3	3.47	3.32	0.59	3.0	0.9	1	3.6
Ho	0.4	0.68	0.66	0.1	0.6	0.2	0.2	0.7
Er	1.14	2.04	1.78	0.25	1.6	0.4	0.4	2
Tm	0.18	0.31	0.32	0.04	0.2	0.1	0	0.3
Yb	1.06	1.86	1.76	0.34	1.4	0.3	0.3	1.9
Lu	0.22	0.31	0.31	0.06	0.2	0	0	0.3
Sc	4	16	17	3	15.4	2.4	2.5	9.7
Y	11.2	17.7	17.1	3.2	15.4	3.9	3.5	18.7

(Sick & tired)
But I don't wanna mess up
*Cause **life goes on***

-병 [Dis-ease]
BTS